



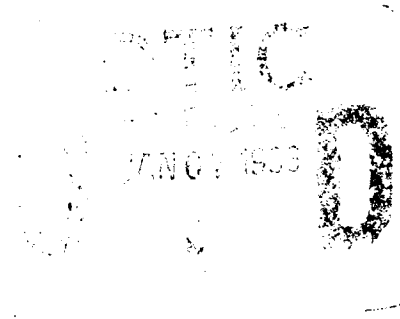
AFIT/GAE/ENY/92D-16

**OPTIMAL CONTROL OF THE
STARFIRE BEAM DIRECTOR**

THESIS

TROY V. LANIER

AFIT/GAE/ENY/92D-16




93-00045

Approved for public release; distribution unlimited.

OPTIMAL CONTROL OF THE STARFIRE BEAM DIRECTOR

THESIS

Presented to the Faculty of the School of Engineering
of the Air Force Institute of Technology

Air University

In Partial Fulfillment of the
Requirements for the Degree of
Master of Science in Aeronautical Engineering

Troy V. Lanier, B.S.

December 1992

Approved for public release; distribution unlimited.

Accession For	
NTIS CRA&I	<input checked="checked" type="checkbox"/>
DTIC TAB	<input type="checkbox"/>
Unannounced	<input type="checkbox"/>
Justification	
By	
Distribution /	
Availability Codes	
Dist	Avail and/or Special
A-1	

Acknowledgments

I wish to acknowledge the support of those people who helped me complete this thesis. First, I thank Dr. Brett Ridgely, my thesis advisor, for his guidance, patience and for allowing me to pick a thesis that was not directly up his alley, but one that I felt passionate about. I thank him for the long hours of optimal control discussion - I envy his enthusiasm.

I thank Dr. Sal Cusamano at the Phillips Lab for sponsoring this effort, allowing me to keep my fingers in the type of work I enjoy, before I move on to see what else the Air Force has to offer.

Mostly, I thank my wife, Francesca, for enduring these eighteen months, while giving me the support I needed and raising our one year old boy. With the completion of this thesis I now look forward to a normal job and devoting more time to my family.

Troy V. Lanier

Table of Contents

	Page
Acknowledgments	ii
List of Figures	vii
List of Tables	x
List of Symbols	xi
List of Acronyms	xiv
Abstract	xv
I. Introduction	1-1
1.1 Background	1-1
1.2 Problem Statement	1-3
1.3 Objectives	1-3
1.4 Scope	1-3
1.5 Assumptions	1-4
1.6 Tools	1-5
1.7 Thesis Organization	1-5
II. Starfire Beam Director Modeling	2-1
2.1 Introduction	2-1
2.2 Starfire Beam Director Description	2-1
2.3 System Configuration	2-2
2.4 Azimuth Axis Linear Plant Model	2-4
2.4.1 Current Loop	2-7
2.4.2 Gimbal Dynamics	2-11
2.4.3 Nominal Plant Model	2-12
2.5 Plant Disturbances and Sensor Noise	2-13
2.5.1 Plant Disturbances	2-14

	Page
2.5.1.1 Bearing Friction	2-14
2.5.1.2 Wind Buffeting	2-16
2.5.1.3 Motor Ripple and Cogging	2-17
2.5.2 Sensor Noise	2-19
2.6 Digital Control Effects	2-19
2.7 SBD Model Summary	2-20
III. Optimal Control Design Techniques	3-1
3.1 Background	3-1
3.2 Design Techniques	3-4
3.2.1 Unity Feedback Setup	3-5
3.2.1.1 Control Weighting Rationale	3-8
3.2.1.2 Building the P Matrix	3-10
3.2.1.3 H_2 and H_∞ Algorithms	3-10
3.2.2 Two-Degree of Freedom Controller Setup	3-10
IV. SBD Azimuth Axis Controller Design	4-1
4.1 Introduction	4-1
4.2 Scaling Problem	4-1
4.3 Position Command Inputs	4-2
4.4 Unity Feedback Design	4-3
4.4.1 Control Weightings	4-4
4.4.2 H_2 Controller Synthesis	4-8
4.4.3 Controller Fine Tuning	4-8
4.4.3.1 Control Use Weighting	4-9
4.4.3.2 "Manual" Pole Placement	4-10
4.5 Two-Degree of Freedom Controller Design	4-11

	Page
V. Azimuth Axis Simulations and Results.....	5-1
5.1 Introduction.....	5-1
5.2 Controller Comparison.....	5-1
5.2.1 Current SBD Controller	5-3
5.2.2 H ₂ Optimization Controller	5-3
5.3 Simulations and Results	5-4
5.3.1 Torque Disturbance and Sensor Noise	5-4
5.3.2 Step Response	5-6
5.3.3 Ramp Response	5-8
5.3.4 Ephemeris Response	5-10
5.3.5 Full-Up Simulation	5-12
5.3.6 Summary of Results	5-13
VI. Elevation Axis.....	6-1
6.1 Introduction	6-1
6.2 Elevation Axis Linear Plant Model.....	6-1
6.3 Torque Disturbance and Sensor Noise	6-2
6.4 Nominal and Truth Models	6-4
6.5 Elevation Axis Controller Design	6-5
6.6 Simulation and Results.....	6-6
VII. Conclusions/Recommendations	7-1
7.1 Conclusions.....	7-1
7.1.1 Azimuth Axis Performance.....	7-1
7.1.2 The Price to Pay	7-2
7.2 Future Research.....	7-3
7.3 Closing Comments	7-5

	Page
Appendix A: Final Compensator Design	A-1
A.1 Azimuth Axis Compensator	A-1
A.2 Elevation Axis Compensator	A-1
Appendix B: Matlab M-Files	B-1
B.1 Introduction	B-1
B.2 List of M-files	B-1
B.3 Azimuth Axis Plant "azplant"	B-2
B.4 Elevation Axis Plant "elplant"	B-4
B.5 Weighting, Disturbance, and Noise Parameters "param"	B-5
B.6 Building the P matrix "pbazsw15"	B-6
B.7 H_2 Optimization "H2"	B-7
B.8 H_2 Optimization "h2opt"	B-7
B.9 Frequency Responses "sentoteval"	B-8
Appendix C: Simulink Block Diagrams	C-1
Appendix D: SBD Controller Design and Simulation Tutorial	D-1
Appendix E: Full-Up Simulation Plots	E-1
References	R-1
Vita	V-1

List of Figures

Figure	Page
2-1 Starfire Beam Director.....	2-2
2-2 Beam Director Configuration	2-3
2-3 Top Level System Block Diagram	2-3
2-4 Fine Position Servo Loop	2-4
2-5 Coelostat Plant	2-5
2-6 Position Servo Loop Signal Measurement Setup	2-7
2-7 Current Loop.....	2-8
2-8 Current Loop Frequency Response	2-9
2-9 Second-Order Model of Current Loop Frequency Response	2-10
2-10 Nominal Plant Model.....	2-13
2-11 SBD Plant Model with Disturbances and Sensor Noise	2-14
2-12 Dahl Friction Model	2-15
2-13 Simulink Bearing Friction Model	2-16
2-14 Wind Buffeting Coloring Filter	2-17
2-15 Torque Disturbance Coloring Filter.....	2-18
2-16 Zero-Order Hold	2-20
3-1 Optimal Control Setup.....	3-1
3-2 State-Space Block Diagram Form	3-5
3-3 Unity Feedback Setup.....	3-7
3-4 General Shape of Sensitivity	3-8
3-5 Two Degree of Freedom Controller Setup	3-12
3-6 Track Weighting	3-12
4-1 Position Command Input	4-3
4-2 Velocity Derived From Position Command	4-3

Figure	Page
4-3 Unity Feedback Setup	4-4
4-4 Output Multiplicative Uncertainty Block Diagram	4-6
4-5 Closed-Loop State Weighting Block Diagram	4-6
4-6 Sensitivity Weighting	4-7
4-7 Controller Magnitude Frequency Response	4-9
4-8 Control Usage Weighting	4-10
4-9 Two Degree of Freedom Controller Setup	4-12
4-10 2 nd Order Track Weighting	4-12
4-11 Step Response	4-14
4-12 Tracking Error to Ramp Command	4-14
4-13 Truncated Tracking Error to Ramp Command	4-15
4-14 Tracking Error to Ephemeris Command	4-15
4-15 Truncated Tracking Error to Ephemeris Command	4-16
5-1 Bode Magnitude Frequency Response	5-2
5-2 Bode Phase Frequency Response	5-2
5-3 Torque Disturbance	5-5
5-4 Position Error to Torque Disturbance	5-5
5-5 Torque Disturbance Rejection Transfer Function	5-6
5-6 Step Response	5-7
5-7 Closed-Loop Transfer Function	5-7
5-8 Ramp Command Tracking Error	5-8
5-9 Truncated Ramp Command Tracking Error	5-9
5-10 Bearing Friction Effect With Current Controller	5-10
5-11 Bearing Friction Effect With H ₂ Controller	5-10
5-12 Ephemeris Command Tracking Error	5-12

Figure	Page
5-13 Full-Up Simulation Tracking Error	5-13
6-1 Elevation Axis Current Loop Frequency Response.....	6-2
6-2 Torque Disturbance Coloring Filter.....	6-3
6-3 Sensitivity Weighting	6-6
6-4 Torque Disturbance Rejection Transfer Function	6-7
6-5 Ephemeris Command Tracking Error.....	6-8
7-1 Closed-Loop Transfer Function.....	7-3
C-1 Current Controller Simulation Model "SimCCEvalMod"	C-1
C-2 Current Controller Linmod Model "SimCCTotEvalMod"	C-2
C-3 Unity Feedback Simulation Model "SimSenEvalMod"	C-3
C-4 Unity Feedback Linmod Model "SimSenTotEvalMod1"	C-4
C-5 2 Degree of Freedom Controller Simulation Model "SimTrckEvalMod"	C-5
C-6 2-Degree of Freedom Controller Linmod Model "SimTrckTotEvalMod"	C-6
E-1 Current Controller Tracking Error PSD	E-1
E-2 H ₂ Controller Tracking Error PSD.....	E-1
E-3 Current Controller Voltage.....	E-2
E-4 H ₂ Controller Voltage	E-2
E-5 Current Controller Voltage PSD	E-3
E-6 H ₂ Controller Voltage PSD.....	E-3
E-7 Current Controller Amps.....	E-4
E-8 H ₂ Controller Amps	E-4
E-9 Current Controller Motor Torque.....	E-5
E-10 H ₂ Controller Motor Torque	E-5
E-11 Current Controller Motor Torque PSD	E-6
E-12 H ₂ Controller Motor Torque PSD	E-6

List of Tables

Table	Page
2-1 Documentation Parameters	2-5
2-2 Azimuth Axis Parameters	2-21
4-1 Unity Feedback Controller Comparison	4-9
4-2 Two Degree of Freedom Controller Comparison	4-13
5-1 Simulation Results	5-14
5-2 Full-Up Simulation Results	5-14
6-1 Elevation Axis Parameters	6-5

List of Symbols

$G_a(s)$	Amplifier transfer function
$G_{cl}(s)$	Current loop transfer function
A_a, B_a, C_a, D_a	Current loop state-space realization matrices
$G_m(s)$	Motor transfer function
$G_g(s)$	Gimbal dynamics transfer function
A_g, B_g, C_g, D_g	Gimbal dynamics state-space realization matrices
$G_p(s)$	Plant dynamics transfer function
A_p, B_p, C_p, D_p	Plant dynamics state-space realization matrices
$G_c(s)$	Compensator transfer function
K_{FB}	Current loop feedback constant
K_v	Coefficient of viscous friction
K_T	Motor torque constant
J	Moment of inertia
ω_{mb}	Motor break frequency
ω_b	Elevation axis current loop break frequency
ω_{an}	Azimuth axis current loop natural frequency
K_a	Current loop gain constant
ζ_a	Azimuth axis current loop damping ratio
$x(t)$	HP signal generator output
$v(t)$	Compensator voltage output
$y(t)$	Difference between $x(t)$ and $v(t)$
$a(t)$	Current loop ampere output
$\theta(t)$	Gimbal position
$\dot{\theta}(t)$	Gimbal rate

$\dot{\theta}_m(t)$	Digitally measured gimbal position
$\theta_c(t)$	Position command input
$T_m(t)$	Motor torque
$T_d(t)$	Torque disturbance
F_c	Running friction constant
T_c	Running friction torque disturbance constant
τ_D	CPU computational time delay
T	Sample period
ω_s	Sample frequency
ω_c	Bandwidth or zero dB crossover frequency
$G_{pa}(s)$	Pade' approximation transfer function
$G_{sd}(s)$	Approximated sampling effects transfer function
$\Sigma_d(s)$	Wind buffeting PSD
W_d	Torque disturbance coloring filter
A_d, B_d, C_d, D_d	Torque disturbance coloring filter state-space realization matrices
w	Exogenous inputs
z	Controlled outputs
u	Control input
y	Measured output
w_1	Zero-mean, unit intensity, white Gaussian noise disturbance input
w_2	Zero-mean, unit intensity, white Gaussian sensor noise input
K	Controller
P	Optimal control setup plant matrix
$A, B_w, B_u, C_z, D_{zw}, D_{zu}, C_y, D_{yw}, D_{yu}$	The 9 matrices that make up the P matrix
T_{zw}	Closed-loop transfer function of w to z

R_z	Control usage weighting
H	State weighting
W_s	Sensitivity weighting
A_s, B_s, C_s, D_s	Sensitivity weighting state-space realization matrices
Γ	Disturbance distribution matrix
J	LQG performance index
Q	LQG state weighting matrix
S	Sensitivity
T	Complimentary sensitivity
W_t	Tracking error minimization weighting
W_{Rz}	Dynamic control usage weighting
err_{ss}	Steady state position error.

List of Acronyms

ATP	Acquisition, Tracking, and Pointing
CPU	Central processing unit
DSP	Digital Signal Processor
EI	Experimenter's interface
EMF	Electro-magnetic field
FSM	Fast steering mirror
GBL	Ground based laser
LC	Local controller
LOS	Line-of-sight
LQG	Linear quadratic Gaussian
MIMO	Multi-input multi-output
PI	Proportional integral control
PSD	Power spectral density
RAM	Random access memory
RMS	Root mean squared
S/N	Signal to noise ratio
SBD	Starfire Beam Director
SISO	Single-input single-output

Abstract

The Starfire Beam Director (SBD) is located at the Starfire Optical Range at Kirtland Air Force Base in Albuquerque, New Mexico. The SBD capabilities include tracking celestial objects and active or passive tracking of artificial satellites to support the Phillips Laboratory Ground Based Laser Acquisition, Tracking, and Pointing (GBL ATP) program. The pointing and tracking accuracy needed to support such experiments is microradian to sub-microradian level. To accomplish this goal requires precise pointing of the massive 6 ton 1-meter clear aperture coelostat¹.

The purpose of this thesis is to use optimal control design techniques to develop a controller to meet the stringent pointing requirements. A nominal linear state-space model was built which included gimbal dynamics, plant disturbances, and sensor noise. Then optimal design techniques were used to develop unity feedback and two degree of freedom controllers. The various controllers were simulated with the coelostat "truth" model, which incorporated the higher frequency current loop and motor dynamics, nonlinearities, plant disturbances, sensor noise, and discrete control effects. The best of the designs, the H_2 unity feedback controller, was compared and contrasted with the performance of the controller currently being used, which was obtained by classical control design. The H_2 controller exceeded tracking requirements and in most areas performed better than the current controller.

¹Coelostat refers to a two-mirror beam director gimbal.

OPTIMAL CONTROL OF THE STARFIRE BEAM DIRECTOR

I. Introduction

1.1 Background

The background discussion is intended to be a generic description of the acquisition, pointing, and tracking (ATP) functions of a beam director. Most beam directors have ATP systems and procedures that are slightly different from this description, but the general process and terminology is the same.

The term "beam director" is generally intended to describe a device which takes the output of a stationary laser device and transmits it in an arbitrary direction. To accurately illuminate an object with a laser beam the object must be tracked with minimal line-of-site (LOS) error. Typically, beam directors incorporate both passive and active tracking to minimize LOS error. Active tracking is used once an object is in the field of view and there is enough return image intensity for a coarse or fine acquisition sensor, such as a 30 Hz frame rate camera and/or a focal plane array, to close a beam steering mirror loop. The beam steering mirror is commonly called a fast steering mirror (FSM). Passive tracking, also known as predictive control, uses ephemeris computation as a command input to a beam director's gimbal position servo loop. A tracking error signal is then derived from an encoder measuring beam director gimbal position. The passive LOS stabilization is thus considered "open-loop" pointing in the sense that no precise

measurement of tracking error using a target image is fed back to close the gimbal position servo loop.

The two types of tracking can be simultaneously used to effectively reduce LOS error. The acquisition and tracking of an object starts with open-loop pointing, where assuming the ephemeris data is accurate enough to bring the object into view of a coarse acquisition camera, an update is made to the ephemeris making it more accurate. Once the return image yields enough intensity on a fine acquisition sensor, a focal plane array, the FSM loop can be closed to further reduce the LOS error effects of residual gimbal motion², atmospheric turbulence, and ephemeris inaccuracy.

Tracking low-earth orbit satellites presents a very difficult challenge for a beam director, because the gimbal must reach velocities of 5° to 10° per second, demanding extremely large step sizes in the ephemeris position command and causing many plant disturbances that must be rejected. Assuming that the ephemeris is accurate, good open-loop pointing will have LOS error of less than 5 μ rad RMS [5:60]. Of course, the measure of "good" tracking will vary with the requirements of the particular task. Typically, once the FSM loop is closed LOS error can be reduced to sub- μ rad.

Although it is true that a FSM loop with high bandwidth and adequate dynamic range can effectively reduce LOS error, it is necessary to have accurate open-loop pointing for several reasons: return image intensity must initially be present on the coarse and/or fine acquisition sensor; image intensity must remain uninterrupted; if the FSM should break track and open-loop pointing is accurate, intensity will not be lost and FSM tracking can be immediately resumed; and if open-loop pointing is accurate, the more likely the FSM will not break track. For large propagating laser beam divergence, full angle 50 to 70 μ rad, open-loop pointing accuracy is not as critical as it is for smaller beam divergence. As long as there is enough intensity on the acquisition sensors the

²Residual gimbal motion refers to the LOS error not rejected or possibly even created by the closed position servo loop, or open-loop pointing.

FSM loop can be closed to reduce LOS error. However, for example, if the beam divergence is $30\text{ }\mu\text{rad}$ full angle and open-loop pointing is $5\text{ }\mu\text{rad}$ RMS the LOS error will have peaks of $15\text{ }\mu\text{rad}$ and appropriate intensity can not be maintained to close the FSM loop. Add an ephemeris bias error of 5 to $10\text{ }\mu\text{rad}$ and the problem is worse. Also, there are times when closing the FSM loop will not be possible, such as tracking dim sunlit satellites where the image does not have the required intensity, or daylight tracking of objects where the sensitive coarse acquisition camera cannot be used and signal-to-noise (S/N) ratio of the fine acquisition sensor is too low due to sunlight.

1.2 Problem Statement

The SBD linear dynamics, non-linearities, plant disturbances, and sensor noise need to be modeled, and design of a controller for the position servo loop is needed, which will effectively reject modeled plant disturbances and track actual ephemeris data for a low-earth orbiting satellite to less than $5\text{ }\mu\text{rad}$ RMS.

1.3 Objectives

The SBD currently has a controller in operation that meets the specifications described in the background section. That controller was developed by classical control design. The object of this thesis is two-fold; first, design a controller that has better performance than the current controller, and second, use optimal control design techniques to develop the controller.

1.4 Scope

While in the background section many parts of the ATP system were described, this thesis only addresses the position servo loop or open-loop pointing. From here on, closed-loop tracking will be in reference to the position servo loop as opposed to the closed FSM loop. The position servo loop is made up of two loops; the coarse position loop and the fine position loop. The coarse position loop uses "bang-bang" control to

provide a time optimal response to large position commands. A maximum voltage in the feedforward path creates a constant acceleration or deceleration. Once the position error falls below a predefined level, the control switches from the coarse to the fine position loop. The controller design in this thesis is only for the fine position loop.

The plant model, for which the controller is designed, does not account for the effects of high frequency resonant dynamics. Notch filters will have to be designed as they have been for the current controller.

Coupling between the azimuth and elevation axes is not considered in this thesis. Separate controllers are designed for each axis, which simplifies the design to two single-input single-output (SISO) systems. Simplifying the design is not the motivation behind not including coupling, but rather that the coupling is not understood well enough to model.

1.5 Assumptions

Saturation occurs when the compensator output is greater than ± 10 volts. Non-linear saturation analysis is not performed with the fine position loop. It is assumed that by the time hand-off from the coarse to the fine position loop occurs the system will be approaching steady state conditions and the transients due to the hand-off will not be too severe. Even if this is not a completely valid assumption, the results of the comparison of the currently used controller versus the H_2 controller, in Chapter 5, show that the output voltage transients due to various commanded input types are very similar. Therefore, the H_2 controller should not perform any worse than the current controller in regard to saturation.

A major source of disturbance in the system is back electro-magnetic field (EMF) of the motor. The amplifier has built-in proportional plus integral (PI) control circuitry for the purpose of rejecting the back EMF. Since measured closed-loop amplifier dynamics are used in the plant model, back EMF is not simulated as a disturbance. It is

assumed that the built-in amplifier circuitry yields zero steady state error due to the EMF. The EMF can be simulated as a step input because it is a linear function of velocity and velocity is nearly constant throughout a satellite pass. PI control yields zero steady state error to a step input. At worst case the commanded position input has a small acceleration component, in which case the EMF is a ramp disturbance and with a near integrator in the H_2 controller the result should be near zero steady state error. A full description of the amplifier dynamics is presented in section 2.4.1.

1.6 Tools

All computer modeling, analysis, and word processing was done on a Macintosh IIsx with a 32K cache card, 20MHz math coprocessor, 5MB of RAM, and a 40MB hard drive. Microsoft Word 5.0 was used for word processing. Matlab/Simulink™ was used for modeling, controller design, and analysis. Linear modeling and controller design utilized the Control System, Robust-Control, Matlab, and Signal Processing Toolboxes, and the H_2 and H_∞ algorithms written as Matlab script M-files by Dr. Brett Ridgely. Simulations with the controller, full linear plant, non-linearities, plant disturbances, and sensor noise were performed in Simulink.

1.7 Thesis Organization

This thesis concentrates on the controller design for the coelostat's azimuth axis for several reasons. First, it is only necessary to show the detailed design of the controller for one axis to demonstrate the optimal control design techniques. Second, the azimuth axis is chosen because more accurate data is available for the azimuth plant dynamics than for the elevation axis dynamics. Third, the comparison of the optimal design to the current azimuth axis controller is straightforward compared to the current elevation axis controller, where direct feedforward control had to be implemented for reasons not even the SBD engineers clearly understand.

Chapter 2 details the nominal and truth plant model, non-linear effects, plant disturbances, and sensor noise for the azimuth axis.

Chapter 3 gives an overview of optimal control design techniques.

Chapter 4 details the azimuth axis optimal controller design with some results of the less successful controllers.

Chapter 5 starts with a description of the controller currently used on the azimuth axis and then compares and contrasts the simulation results of the best H_2 controller versus the current controller.

Chapter 6 builds the model and designs the controller for the elevation axis and provides results.

Chapter 7 presents conclusions and recommendations for future research.

II. Starfire Beam Director Modeling

2.1 Introduction

The first few sections of this chapter describe the overall function and operation of the SBD. The emphasis of this chapter is contained in the last sections where the linear nominal model, plant disturbances, sensor noise, and the truth model, which incorporates the high frequency amplifier dynamics, discrete control effects, and non-linearities are developed. It is important to distinguish between the nominal and truth models because the optimal controller is designed for the nominal model, plant disturbances, and sensor noise, while simulations are performed with the truth model.

2.2 Starfire Beam Director Description

The SBD is an elevation over azimuth coelostat that maintains a 1-meter clear aperture over a full hemisphere. The coelostat weighs approximately 6 tons and has hydrostatic oil bearings in both axes to reduce bearing friction and noise. The azimuth motor can generate a maximum torque of 3000 ft-lbs and the elevation motor 300 ft-lbs. The maximum rates for the azimuth and elevation axes are set at 10° and 5° per second, respectively. It currently has the capability to track celestial objects and artificial satellites with less than 2 μ rad RMS of LOS error. Figure 2-1 is a picture of the SBD.

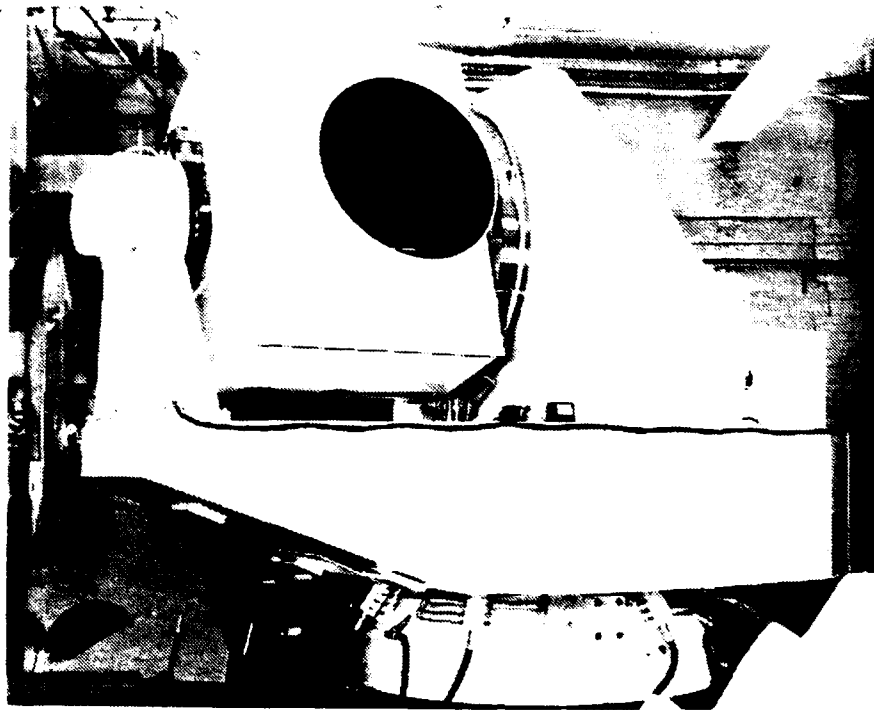


Figure 2-1 Starfire Beam Director

2.3 System Configuration

Figure 2-2 represents a beam director configuration similar to the SBD. There is an optical bench on which the visiting experimenters can mount lasers and optical equipment. The Coude' path³ contains a large turning flat mirror, a mirror mounted to the gimbal's azimuth axis, and a mirror mounted to the elevation axis.

Figure 2-3 is the top level block diagram of the beam director system. The experimenter's interface (EI) allows the experimenters to select a mode to point at a selected star, planet, or satellite. The remote controller (RC) calculates the pointing vector (ephemeris) based on the mode selected. The output of the RC is the position command input to the position servo loop, or what the SBD engineers refer to as the inner loop. The local controller (LC) refers to both the coarse and fine position loops.

³The Coude' path is the optical path from the edge of the optical bench to the exiting side of the elevation mirror.

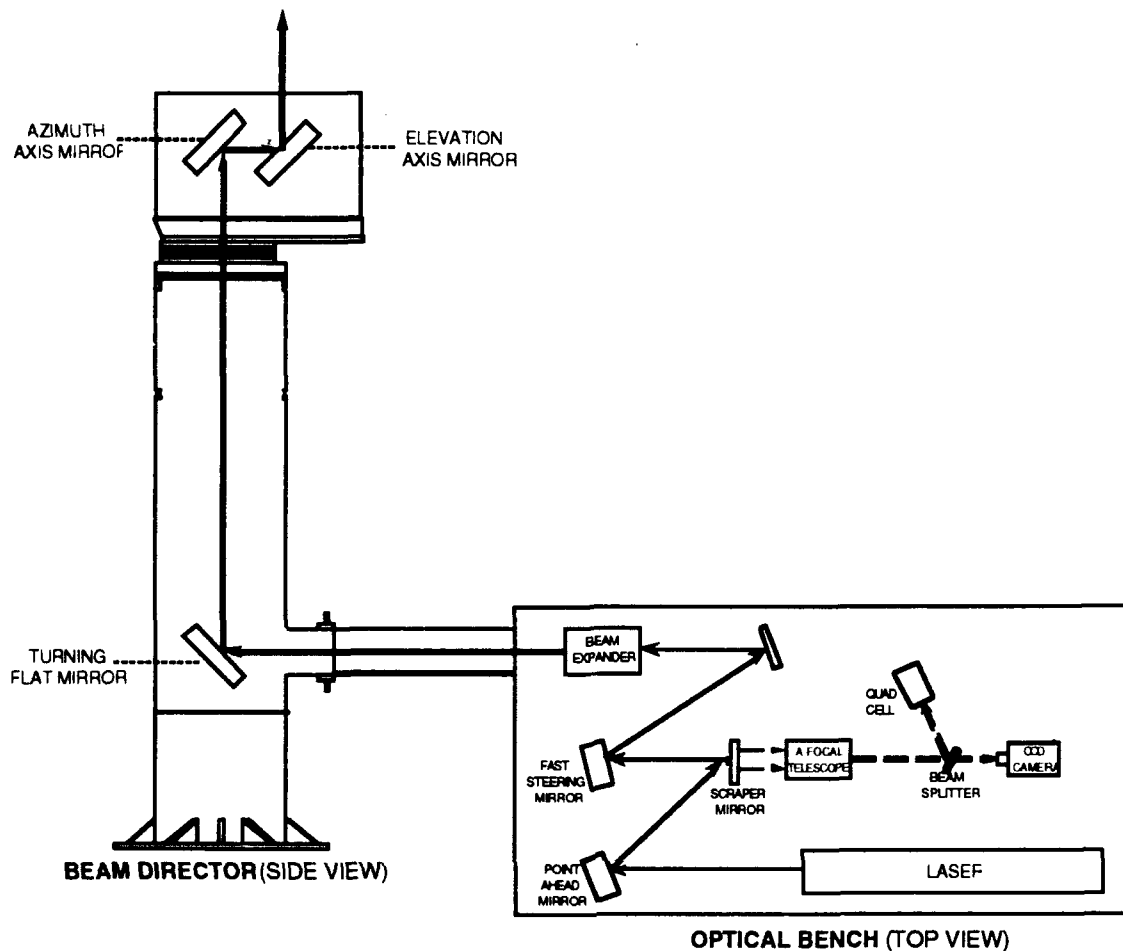


Figure 2-2 Beam Director Configuration

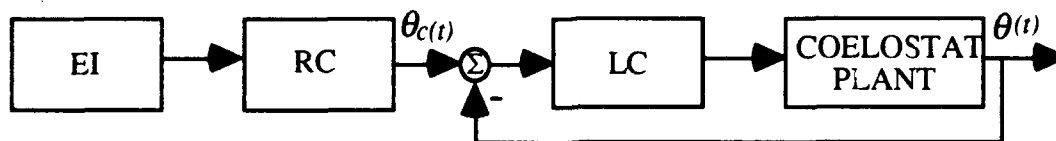


Figure 2-3 Top Level System Block Diagram

From here on, this thesis only addresses the fine position loop portion of the local controller shown in Figure 2-4. The SBD utilizes high speed digital signal processors (DSP) running at 200 Hz to execute digital control. The compensator output is then

converted to an analog voltage signal to drive the plant. Gimbal position is measured by highly accurate Inductosyn™ encoders, one for each axis, and the digitally measured position is fed back to form position error. Although the controller is discrete, it is designed and simulated in the continuous domain using a continuous approximation to a zero-order hold to account for the delay effects of discrete control. The approximation is developed in section 2.6.

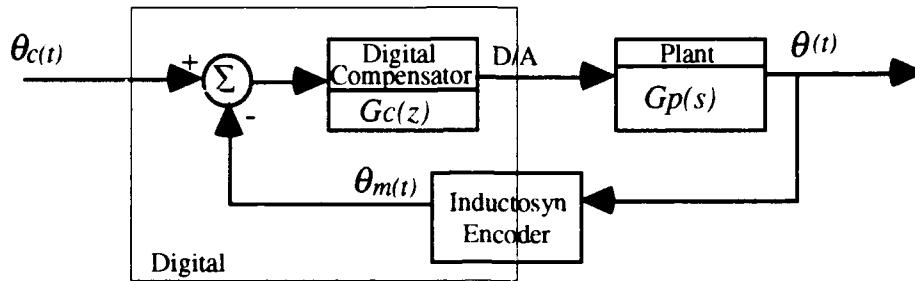


Figure 2-4 Fine Position Servo Loop

2.4 Azimuth Axis Linear Plant Model

The plant, consisting of an amplifier, motor, and gimbal is shown in Figure 2-5. The current feedback loop is necessary to reject back EMF disturbance, which is discussed in detail in section 2.4.1. The closed current loop G_{cl} can be modeled as

$$G_{cl}(s) = \frac{Gm(s)Ga(s)}{1 + Gm(s)Ga(s)K_{FB}} \quad (2.1)$$

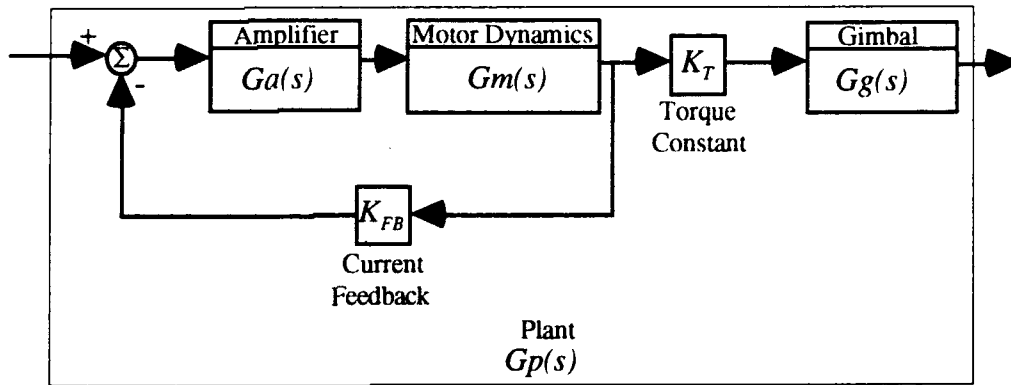


Figure 2-5 Coelostat Plant

The parameter values used to construct the plant dynamics are obtained from two sources. The first source is the original coelostat documentation, *Technical Description of a Coelostat System* [1]. The parameters and the values used in the model are shown in Table 2-1 [1:134]. The second and most accurate source is frequency response data taken from the actual SBD system in June 1991. The frequency responses are more accurate than the technical documentation because the documentation was written over twenty years ago and most of the parameters have changed due to system wear and small modifications. Unfortunately, complete frequency response data is not available for every component of the plant; therefore, documentation data is used for part of the model.

Table 2-1 Documentation Parameters

Parameter		Azimuth Axis
Moment of Inertia (ft-lbs-sec ²)	J	26000
Coefficient of Viscous Friction (ft-lbs/rad/sec)	K_v	350
Motor Torque Constant (ft-lbs/amp)	K_T	75.6
Motor Lag Frequency	ω_{mb}	60.0

Ideally, to accurately determine the frequency response of each component of the plant, the input and output of each component should be directly measurable. Figure 2-6 depicts the position servo loop and the signals that were measured to determine the system's frequency responses. The signal generator and the signal analyzer are shown as separate devices for clarity. Actually, they are both part of a Hewlett-Packard Dynamic Signal Analyzer. A sine signal $x(t)$ was input at the summing junction and the component transfer functions were calculated by measuring the signals $v(t)$, $y(t)$, $a(t)$, and $\theta_m(t)$ as the frequency of $x(t)$ was incremented through a range. $v(t)$ is the voltage output of the compensator, $y(t)$ is the difference between $v(t)$ and the signal generator output $x(t)$, $a(t)$ is the ampere output of the current loop, and $\theta_m(t)$ is the digitally measured gimbal position. Open and closed-loop transfer function data was acquired with this setup, where the open and closed loops were defined as

$$\frac{v(s)}{y(s)_{ol}} = G_c(s)G_g(s)K_T G_{cl}(s) \quad \frac{v(s)}{x(s)_{cl}} = \frac{G_c(s)G_g(s)K_T G_{cl}(s)}{1 + G_c(s)G_g(s)K_T G_{cl}(s)} \quad (2.2)$$

However, only the current loop data is useful for modeling and is described by the open loop transfer function

$$G_{cl}(s) = \frac{a(s)}{y(s)} \quad (2.3)$$

The torque constant K_T and the gimbal dynamics, theoretically, could have been backed out of the open loop transfer function of $\theta_m(t)$ to $y(t)$, but the data was not output at low enough frequency to determine the low frequency effect of the gimbal's viscous damping. Therefore, actual data is used to model the current loop and parameters from the original documentation are used for the torque constant and gimbal dynamics. The controller is designed with high gain and phase margins (stability robustness) to account for the uncertainty associated with using the parameters in place of actual data.

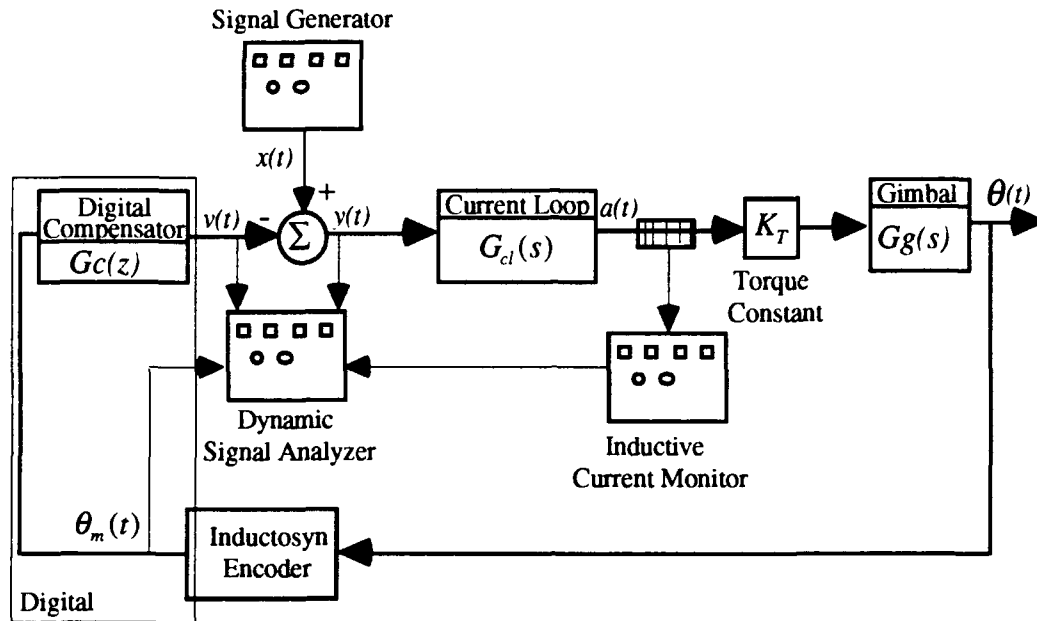


Figure 2-6 Position Servo Loop Signal Measurement Setup

2.4.1 Current Loop. As briefly discussed in section 1.5 the amplifier was designed with PI circuitry to reject back EMF of the motor. It was also designed to include a lead to cancel the 20 dB per decade roll off at 60 rad/sec due to the motor resistance and inductance (see Eqn 2.4). Figure 2-7 is a model of the current loop used in designing the presently used controller. The current loop parameters for this model were obtained from the original coelostat document.

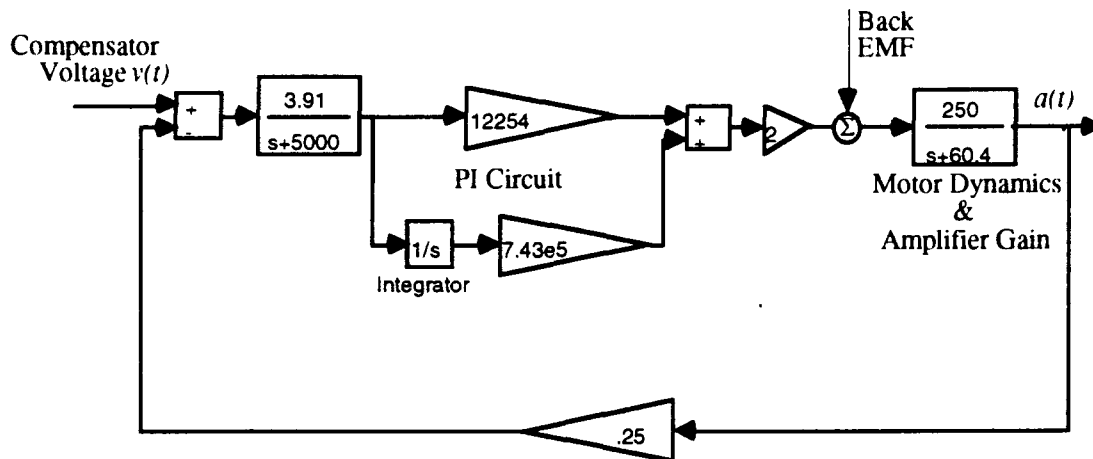


Figure 2-7 Current Loop

The transfer function equivalent of the closed current loop is

$$G_{cl}(s) = \frac{2.4 \times 10^7 (s + 60.6)}{(s + 3011)(s + 1988)(s + 60.6)} \text{ amps / volt} \quad (2.4)$$

The Bode plot in Figure 2-8 shows that the closed current loop has a roll off at approximately 2000 rad/sec, or 320 Hz, and a dc (low frequency) gain of 12 dB or 4 amps/volt . As stated in Section 1.5 it is assumed that the current loop effectively rejects the back EMF; therefore, back EMF is not simulated and the measured closed current loop transfer function is used in the model.

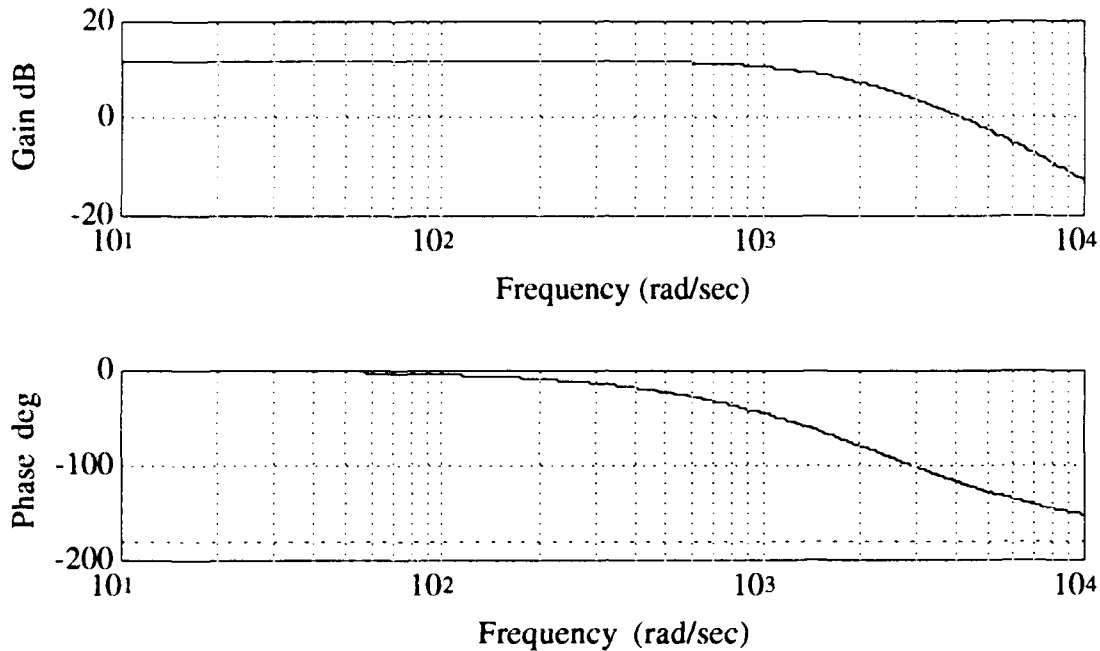


Figure 2-8 Current Loop Frequency Response

The measured current loop data came in the form of an HP signal analyzer Bode plot and can be closely modeled as a standard second-order transfer function

$$G_{cl}(s) = \frac{K_a \omega_{an}^2}{s^2 + 2\zeta_a \omega_{an} s + \omega_{an}^2} \quad (2.5)$$

This plot showed another 40 dB/decade attenuation at approximately 2000 rad/sec, but at such a high frequency its contribution to system dynamics would be negligible; therefore, it was neglected. The plot was reconstructed in Matlab by iteration until the shape of the simplified second order model matched the original⁴. The reconstructed simplified model Bode plot, Figure 2-9, shows the current loop having a natural frequency ω_{an} of approximately 560 rad/sec, or 90 Hz; a gain constant $K_a = 4.4$ amps/volt; and a damping ratio $\zeta_a = .25$. The damping ratio was determined from reference [2:253].

⁴The Matlab frequency response plot has 20 dB more gain than the original HP frequency spectral analyzer plot to account for a 10 amp/volt scale factor.

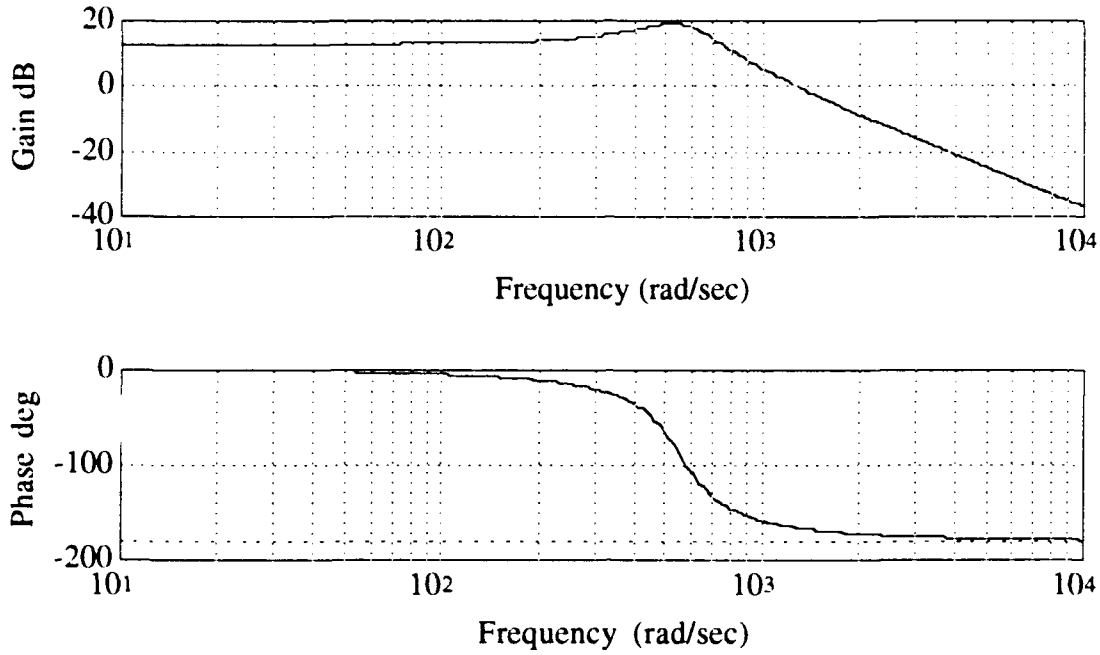


Figure 2-9 Second-Order Model of Current Loop Frequency Response

It is necessary to transform all dynamics to a state-space representation to be used in optimal control design. The state-space representation of $G_{cl}(s)$ is derived as follows:

$$G_{cl}(s) = \frac{a(s)}{v(s)} = \frac{K_a \omega_{an}^2}{s^2 + 2\zeta_a \omega_{an} s + \omega_{an}^2} \quad (2.6)$$

where $v(t)$ is the voltage input to the current loop and $a(t)$ is the current output. After cross multiplying and taking the inverse Laplace transform of both sides the corresponding output differential equation becomes

$$\ddot{a}(t) + 2\zeta_a \omega_{an} \dot{a}(t) + \omega_{an}^2 a(t) = K_a \omega_{an}^2 v(t) \quad (2.7)$$

The state variables are defined as

$$x_a(t) = \begin{bmatrix} a(t) \\ \dot{a}(t) \end{bmatrix} \quad (2.8)$$

The input and output are, respectively,

$$u_a(t) = v(t), \quad y_a(t) = a(t) \quad (2.9)$$

The phase-variable canonical form of the state-space model is

$$\begin{aligned} \dot{x}_a(t) &= A_a x_a(t) + B_a u_a(t) \\ y_a(t) &= C_a x_a(t) + D_a u_a(t) \end{aligned} \quad (2.10)$$

where A_a is the amplifier system matrix, B_a is the input matrix, C_a is the output matrix, and D_a is the direct feedthrough term having the values

$$\begin{aligned} A_a &= \begin{bmatrix} 0 & 1 \\ -\omega_{an}^2 & -2\zeta_a \omega_{an} \end{bmatrix} & B_a &= \begin{bmatrix} 0 \\ K_a \omega_{an}^2 \end{bmatrix} \\ C_a &= [1 \quad 0] & D_a &= 0 \end{aligned} \quad (2.11)$$

2.4.2 Gimbal Dynamics. The motion of the gimbal can be described by the differential equation

$$J\ddot{\theta}(t) + K_v \dot{\theta}(t) = T_m(t) \quad (2.12)$$

where J is the moment of inertia, K_v is the coefficient of viscous friction due to the viscosity of the fluid in the hydrostatic bearings, and $T_m(t)$ is the torque applied by the motor [3:133]. J and K_v are obtained from the coelostat's original documentation (see Table 2-1). The state variables are defined as

$$x_g(t) = \begin{bmatrix} \theta(t) \\ \dot{\theta}(t) \end{bmatrix} \quad (2.13)$$

The input and output are, respectively,

$$u_g(t) = T_m(t) \quad y_g(t) = \theta(t). \quad (2.14)$$

The corresponding state-space representation is

$$\begin{bmatrix} \dot{\theta}(t) \\ \ddot{\theta}(t) \end{bmatrix} = \begin{bmatrix} 0 & 1 \\ 0 & \frac{-K_v}{J} \end{bmatrix} \begin{bmatrix} \theta(t) \\ \dot{\theta}(t) \end{bmatrix} + \begin{bmatrix} 0 \\ \frac{1}{J} \end{bmatrix} T_m(t) \quad (2.15)$$

$$\theta(t) = \begin{bmatrix} 1 & 0 \end{bmatrix} \begin{bmatrix} \theta(t) \\ \dot{\theta}(t) \end{bmatrix} + \begin{bmatrix} 0 \end{bmatrix} T_m(t)$$

or

$$\begin{aligned} \dot{x}_g(t) &= A_g x_g(t) + B_g u_g(t) \\ y_g(t) &= C_g x_g(t) + D_g u_g(t) \end{aligned} \quad (2.16)$$

2.4.3 Nominal Plant Model. When designing a controller using optimal design techniques it is desirable to design the controller around a nominal model and then perform simulations with the truth model. Optimal control will yield controllers with at least as many states as the plant; therefore, it is desirable to keep the order of the plant small to keep the order of the controller small. The nominal plant model only includes the current loop gain constant K_a , the motor torque constant K_T , and the gimbal dynamics $Gg(s)$ as shown in Figure 2-10. The high frequency current loop dynamics are included in the truth model.

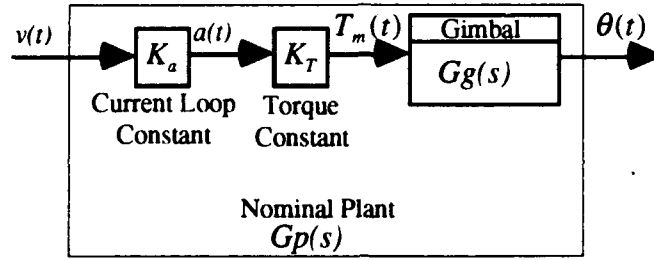


Figure 2-10 Nominal Plant Model

The state-space representation of the nominal plant is

$$\begin{bmatrix} \dot{\theta}(t) \\ \ddot{\theta}(t) \end{bmatrix} = \begin{bmatrix} 0 & 1 \\ 0 & -\frac{K_v}{J} \end{bmatrix} \begin{bmatrix} \theta(t) \\ \dot{\theta}(t) \end{bmatrix} + \begin{bmatrix} 0 \\ \frac{1}{J} K_T K_a \end{bmatrix} v(t) \quad (2.17)$$

$$\theta(t) = \begin{bmatrix} 1 & 0 \end{bmatrix} \begin{bmatrix} \theta(t) \\ \dot{\theta}(t) \end{bmatrix} + \begin{bmatrix} 0 \end{bmatrix} v(t)$$

or

$$\begin{aligned} \dot{x}_p(t) &= A_p x_p(t) + B_p u_p(t) \\ y_p(t) &= C_p x_p(t) + D_p u_p(t) \end{aligned} \quad (2.18)$$

2.5 Plant Disturbances and Sensor Noise

There are many sources of plant disturbances and sensor noise; some are used in the nominal model to design the optimal controller, some are only included in the truth model for simulation, and others are neglected. The position servo loop is shown in Figure 2-11 with all sources of plant disturbances and sensor noise.

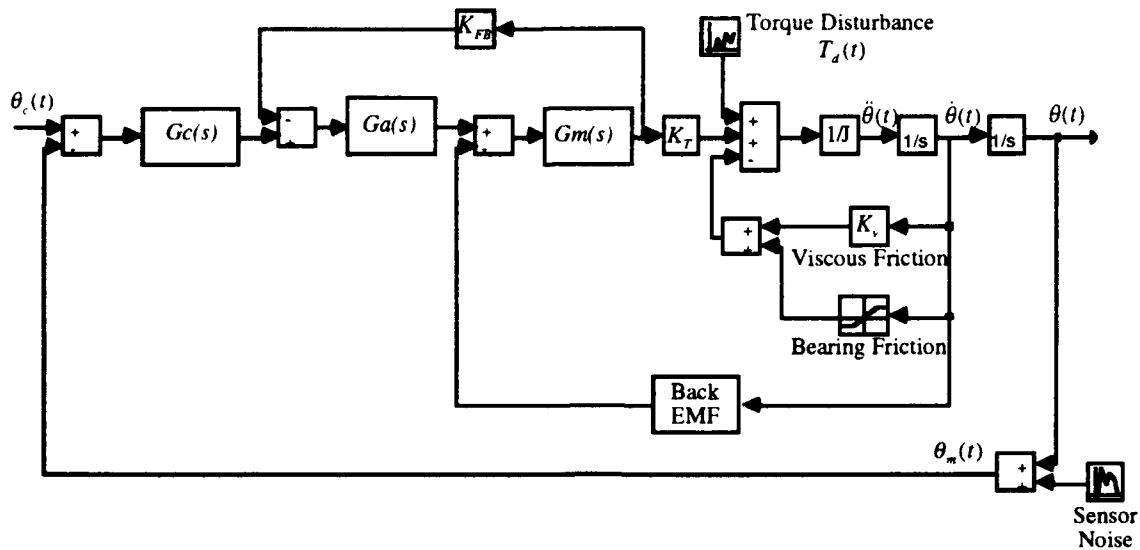


Figure 2-11 SBD Plant Model with Disturbances and Sensor Noise

2.5.1 Plant Disturbances. Most plant disturbances are in the form of torque disturbances. The torque disturbance $T_d(t)$ from Figure 2-11 is used to represent torque disturbance caused by wind buffeting, motor cogging, and motor ripple. Viscous friction is also a torque disturbance due to the viscosity of the fluid in the hydrostatic bearings and is already accounted for in the nominal plant model. Bearing noise is a bandlimited, white noise, torque disturbance that is neglected because of the smooth characteristics of hydrostatic bearings. Bearing friction is a non-linear torque disturbance that is used in the truth model and is discussed in detail in section 2.5.1.1. The last type of plant disturbance is back EMF of the motor that reduces power amp output proportional to the speed of the motor shaft and is not a simulated disturbance as discussed in section 1.5.

2.5.1.1 Bearing Friction. The Dahl friction model, shown in Figure 2-12, exhibits non-linear bearing stiffness and can be used to model bearing friction in a gimbal system, where the displacement x is equal to the change in θ from an initially stationary position. When the bearings are rolling the running friction F_c results in a constant torque disturbance T_c opposing the direction of motion. For the azimuth axis $T_c = 16$ ft-

lbs. The Dahl friction model behaves like a soft spring for small deflections, yet approaches the running friction for large deflections. When force is applied to the bearings they experience plastic deformation, known as the compliance zone. Outside the bearing compliance zone, i.e. bearings are rolling, the disturbance is equal to the running friction [6:2-4].

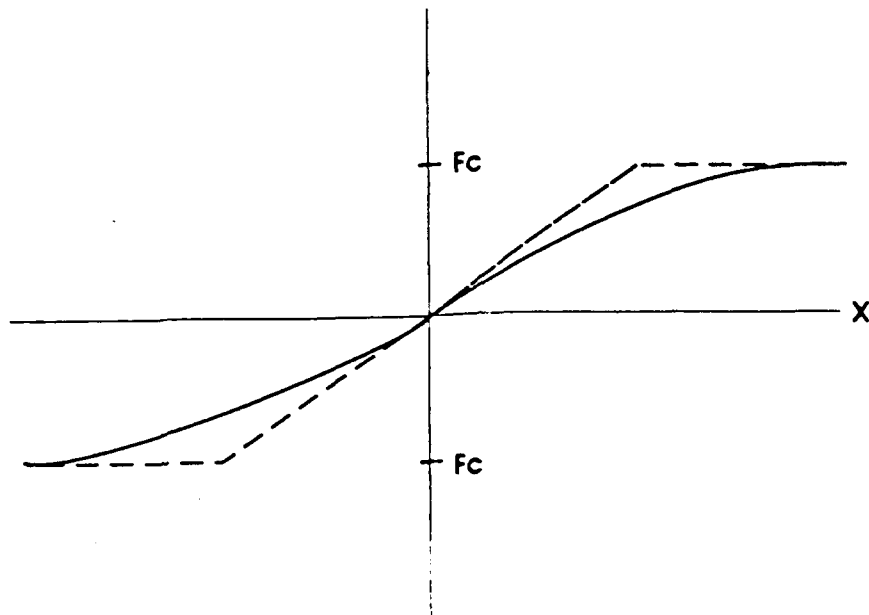


Figure 2-12 Dahl Friction Model

The characteristics of the Dahl friction model can be modeled such that the friction is not a function of θ but rather a function of $\dot{\theta}$. The bearing friction is modeled using the saturation block and a constant gain in Simulink. Figure 2-13 is the Simulink bearing friction model. For $\dot{\theta}(t) \geq 0.001$ rad/sec the saturation block's output value is constant at 0.001, thus the torque disturbance is equal to a constant 16 ft-lbs, i.e. the running friction torque constant. For $\dot{\theta}(t) < 0.001$ rad/sec the torque disturbance is a linear function of $\dot{\theta}(t)$.

$$\text{Torque} = \left(16000 \frac{\text{ft} - \text{lbs}}{\text{rad} / \text{sec}} \right) \dot{\theta}(t) \quad (2.19)$$

which captures the characteristic of the Dahl compliance zone, where small motions from an initially stationary position result in plastic deformation and bearing friction resistance.

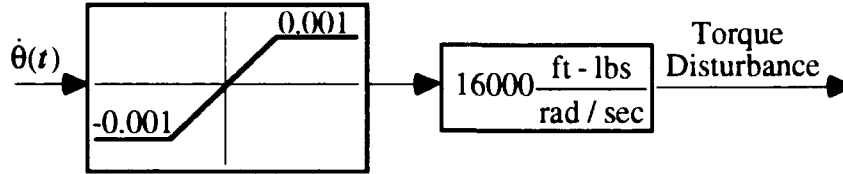


Figure 2-13 Simulink Bearing Friction Model

2.5.1.2 Wind Buffeting. Wind buffeting disturbance data is not available from the SBD, so data from another beam director is used as an estimate [5:54]. The data is in the form of a power spectral density (PSD) plot with units $(\text{ft-lbs})^2/\text{Hz}/\text{Hz}$. The wind disturbance PSD $\Sigma_d(\omega)$ is characterized as low frequency colored noise and can be modeled as a coloring filter $W_d(j\omega)$ driven by zero mean, unity intensity, white Gaussian noise $\Sigma_n(\omega)$, where

$$\Sigma_d(\omega) = |W_d(j\omega)|^2 \Sigma_n(\omega) \quad (2.20)$$

The resulting coloring filter $W_d(s)$ is shown in Figure 2-14.

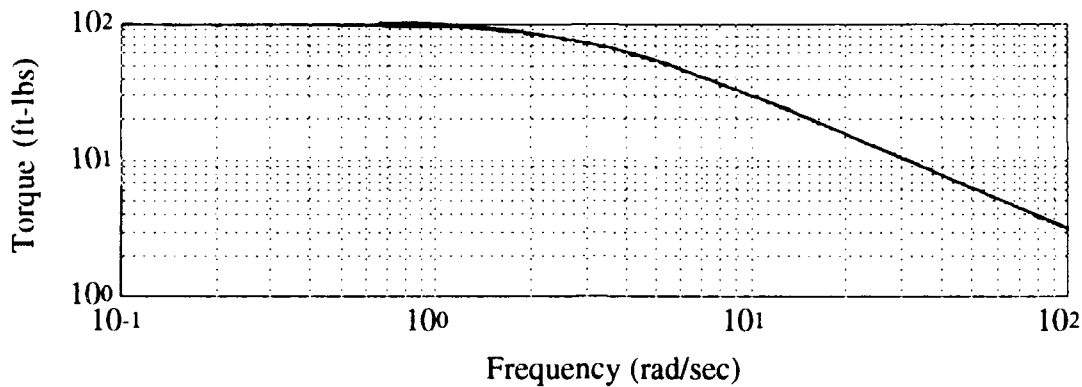


Figure 2-14 Wind Buffeting Coloring Filter

2.5.1.3 Motor Ripple and Cogging. Ripple torque disturbance is due to a small variation in average torque during rotation of the armature. This variation is due to the fact that commutation is done in discrete steps. The ripple torque is a deterministic low frequency sinusoidal effect that is a function of the motor shaft velocity [7:13].

Cogging torque disturbance is due to the non-uniform rotation of the motor armature caused by the tendency of the armature to prefer certain discrete positions. Cogging torque is also a deterministic low frequency effect that is a function of the motor shaft velocity [7:13].

Since both disturbances are low frequency they can be effectively rejected if the position servo loop has adequate bandwidth and low frequency gain. The two disturbances can be conservatively modeled as a coloring filter driven by white noise. The only data available on the actual effects of ripple and cogging disturbance is that it is a low frequency effect that contributes, when not rejected, approximately 60 μ rad of gimbal position error. The coloring filter designed for the wind buffeting disturbance creates 30 μ rad of error when the position servo is simulated open loop. The final torque disturbance coloring filter used for the controller design and simulation is designed to

incorporate wind buffeting, cogging, and ripple disturbance effects and is shown in Figure 2-15.

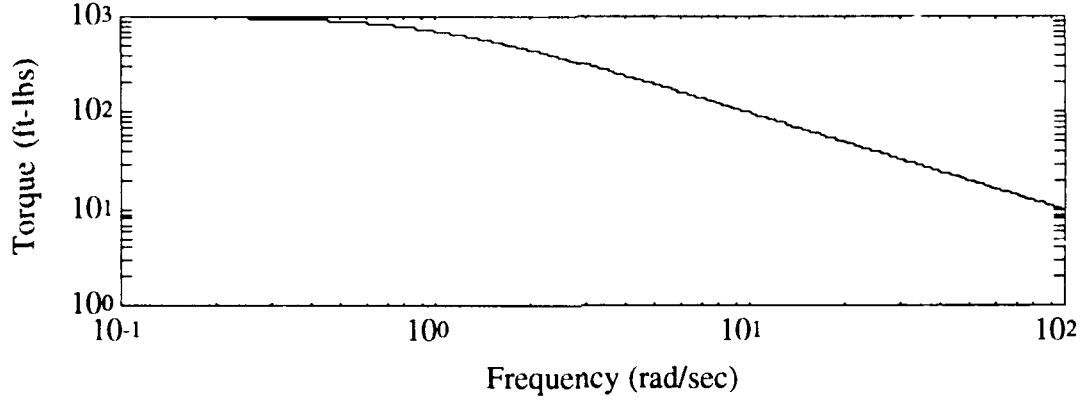


Figure 2-15 Torque Disturbance Coloring Filter

As stated earlier, this disturbance input is used in the optimal controller design, therefore, the coloring filter must be transformed to its state-space representation.

In transfer function form

$$W_d(s) = C_d(sI - A_d)^{-1}B_d + D_d \quad (2.21)$$

In state-variable form

$$\begin{aligned} \dot{x}_d(t) &= A_d x_d(t) + B_d w_1(t) \\ T_d(t) &= C_d x_d(t) + D_d w_1(t) \end{aligned} \quad (2.22)$$

where $T_d(t)$ is the torque disturbance, $x_d(t)$ is the disturbance state, and $w_1(t)$ is zero-mean, unit intensity, white Gaussian noise. The state-space values are

$$\begin{aligned} A_d &= -1 & B_d &= 1 \\ C_d &= 1000 & D_d &= 0 \end{aligned} \quad (2.23)$$

2.5.2 Sensor Noise. The absolute angular gimbal position is measured using an Inductosyn encoder. The measurement of true angular position is corrupted by noise with an RMS of .2 arc seconds or 1 μ rad and is modeled as zero-mean, white Gaussian noise for the controller design. For the simulation the sensor noise is rolled off at 40 dB per decade starting at 50 rad/sec to prevent the unrealistic driving of high frequency control power. A second source of encoder errors are cyclic, deterministic errors, which are a function of the rotation angle, generally comprised of modulated harmonics of the basic Inductosyn pole frequency [7:4]. Modeling of the cyclic errors is beyond the scope of this thesis.

2.6 Digital Control Effects

Digital control has several dynamic effects which can be adverse. Those effects are quantization, CPU computational time, and sample rate.

As shown in Figure 2-6 the input to the inductosyn encoder is continuous time gimbal position and the output is digital. Quantization of the gimbal position measurement is occurring due to the finite word length of the encoder. Without getting into the details of the encoder, the least significant bit is 0.75 μ rad. Quantization effects will be neglected, because the noise effects of the encoder are modeled such that the noise spectrum will account for quantization uncertainty.

The controller hardware consists of a Texas Instrument 320 C-30 Digital Signal Processor (DSP) programmed in C, housed in a VME chassis, with a Macintosh PC as the host. The system runs at 200 Hz, which corresponds to a sample time T of 0.005 seconds. The DSP computational time delay τ_d is assumed to be ≈ 0 , which is a valid assumption if τ_d is much less than T [4:7].

The dynamic effects of sampling and holding can be neglected when

$$\omega_s \geq 30\omega_c \quad (2.24)$$

where ω_s is the sample frequency and ω_c is the system cross-over or bandwidth frequency. Since ω_c is approximately 10 Hz and ω_s is 200 Hz, the ratio is 20, thus the dynamics cannot be neglected. Figure 2-16(a) shows the continuous model of the sampler and the zero-order hold (ZOH).

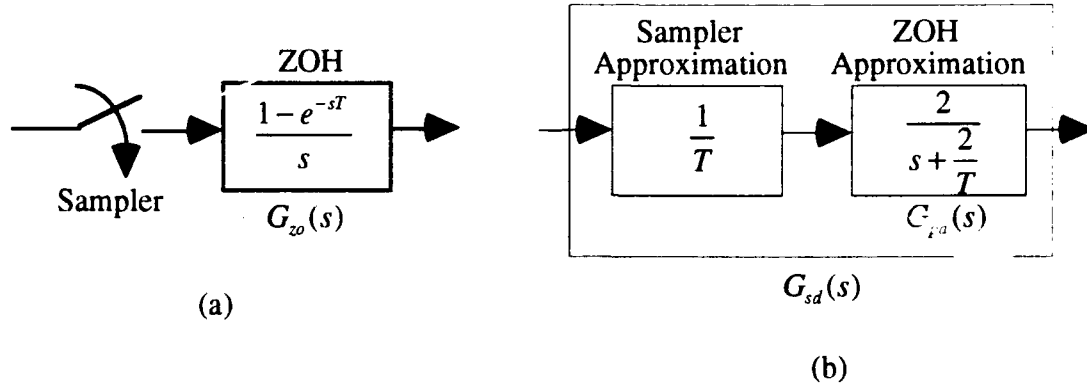


Figure 2-16
(a) Continuous Model (b) Continuous Approximation

The sampler can be approximated by $1/T$ and a first-order Pade' approximation $G_{pa}(s)$ can be used to linearize and approximate the ZOH. Thus,

$$G_{zo}(s) = \frac{1 - e^{-sT}}{s} \approx \frac{2}{s + \frac{2}{T}} = G_{pa}(s). \quad (2.25)$$

The first order Pade' approximation is valid for this system because $\omega_s \geq 10\omega_c$ [4:213]. The combination of the sampler and ZOH approximations are defined as $G_{sd}(s)$ which represent the reduced, approximated, and linearized effects of digital control (see Figure 2-16(b)).

2.7 SBD Model Summary

The optimal controller is designed around the nominal model, which includes: current loop gain constant K_a ; motor torque constant K_T ; gimbal dynamics $Gg(s)$; torque

disturbance input $T_d(t)$; and zero-mean, white Gaussian noise, of 1 μ rad intensity sensor noise. The truth or simulation model includes the nominal model plus: dynamics of the current loop $G_{cl}(s)$; non-linear bearing friction; first order Pade' approximation to a ZOH; and sensor noise rolled off at 40 dB per decade. The azimuth axis parameter values are summarized in Table 2-2.

Table 2-2 Azimuth Axis Parameters

Parameter		Value
Moment of Inertia (ft-lbs-sec ²)	J	26000
Coefficient of Viscous Friction (ft-lbs/rad/sec)	K_v	350
Motor Torque Constant (ft-lbs/amp)	K_T	75.6
Sample Period (sec)	T	0.005
Current Loop Gain Constant (amp/volt)	K_a	4.4
Current Loop Damping Ratio	ζ_a	.25
Current Loop Natural Frequency (rad/sec)	ω_{an}	560
Bearing Friction Torque Constant (ft-lbs)	T_c	16

III. Optimal Control Design Techniques

3.1 Background

H_2 or H_∞ control design begins with the standard positive feedback setup shown in Figure 3-1.

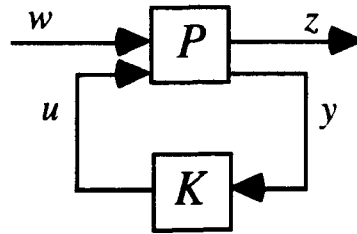


Figure 3-1 Optimal Control Setup

P is the plant, K is the compensator, w is the exogenous input, z is the controlled output, u is the control input, and y is the measured output. P includes system plant dynamics, exogenous input coloring filters, and any dynamic weights on the controlled outputs. P is partitioned as

$$P = \begin{bmatrix} P_{zw} & P_{zu} \\ P_{yw} & P_{yu} \end{bmatrix} \quad (3.1)$$

such that

$$\begin{bmatrix} z \\ y \end{bmatrix} = \begin{bmatrix} P_{zw} & P_{zu} \\ P_{yw} & P_{yu} \end{bmatrix} \begin{bmatrix} w \\ u \end{bmatrix} \quad (3.2)$$

The closed-loop transfer function T_{zw} , which is the transfer function from the external input w to the controlled output z , is given by

$$T_{zw} = P_{zw} + P_{zu}K(I - P_{yu}K)^{-1}P_{yw} \quad (3.3)$$

The objective is to design a stabilizing controller K such that the 2-norm or ∞ -norm of the closed-loop transfer function T_{zw} is minimized. Controller design by H_∞ optimization for the SBD model was less than completely successful (see section 4.2). Therefore, the H_∞ optimization theory and method is not presented.

The 2-norm is defined for a stable transfer function T_{zw} as

$$\|T_{zw}\|_2 = \left(\frac{1}{2\pi} \int_{-\infty}^{\infty} \text{tr}[T_{zw}^*(j\omega)T_{zw}(j\omega)] d\omega \right)^{\frac{1}{2}} \quad (3.4)$$

where tr is the trace and $*$ denotes the complex conjugate transpose. Thus, the 2-norm of the transfer function T_{zw} is minimizing the expected value of the energy of the output z assuming the input w is zero-mean, unit intensity, white Gaussian noise.

The plant P is described by the state-variable differential equations

$$\begin{aligned} \dot{x} &= Ax + B_w w + B_u u \\ z &= C_z x + D_{zw} w + D_{zu} u \\ y &= C_y x + D_{yw} w + D_{yu} u \end{aligned} \quad (3.5)$$

or

$$P = \left[\begin{array}{c|cc} A & B_w & B_u \\ \hline C_z & D_{zw} & D_{zu} \\ C_y & D_{yw} & D_{yu} \end{array} \right] \quad (3.6)$$

The following conditions on P must be true:

- i) $D_{zw} = 0$
- ii) $D_{yu} = 0$
- iii) (A, B_u) stabilizable & (C_y, A) detectable
- iv) $D_{zu}^T D_{zu}$ & $D_{yw} D_{yw}^T$ full rank
- v) $\begin{bmatrix} A - j\omega I & B_u \\ C_z & D_{zu} \end{bmatrix}$ has full column rank for all ω
- vi) $\begin{bmatrix} A - j\omega I & B_w \\ C_y & D_{yw} \end{bmatrix}$ has full row rank for all ω

Condition i) is required or the H_2 problem is not well defined, as the closed-loop transfer function will then have a nonzero D term for any choice of compensator, thus making the closed-loop two-norm infinite. Condition ii) makes the development easier, but can be completely removed. Condition iii) is necessary for the existence of stabilizing solutions. Condition iv) ensures that the penalty on control usage and the sensor noise intensity are nonsingular - relaxation leads to singular control problems. Conditions v) and vi) guarantee the existence of stabilizing solutions to the two Riccati equations which appear in the solution to the problem. [8:69-70]

The H_2 optimal controller is given by

$$K(s) = -\tilde{K}_c (A - K_f \tilde{C}_y - \tilde{B}_u K_c) \tilde{K}_f \quad (3.7)$$

where

$$K_c = \tilde{B}_u^T X + \tilde{D}_{zu}^T C_z \quad (3.8)$$

$$\tilde{K}_c = S_u^{-1} K_c \quad (3.9)$$

$$K_f = Y\tilde{C}_y^T + B_w\tilde{D}_{yw}^T \quad (3.10)$$

$$\tilde{K}_f = K_f S_y \quad (3.11)$$

X and Y are the solutions to the algebraic Riccati equations

$$\left(A - \tilde{B}_u\tilde{D}_{zu}^T\tilde{C}_z\right)^T X + X\left(A - \tilde{B}_u\tilde{D}_{zu}^T\tilde{C}_z\right) - X\tilde{B}_u\tilde{B}_u^T X + \hat{C}_z^T\hat{C}_z = 0 \quad (3.12)$$

and

$$\left(A - B_w\tilde{D}_{yw}^T\tilde{C}_y\right)Y + Y\left(A - B_w\tilde{D}_{yw}^T\tilde{C}_y\right)^T - Y\tilde{C}_y^T\tilde{C}_yX + \hat{B}_w\hat{B}_w^T = 0 \quad (3.13)$$

where

$$\hat{C}_z = \left(I - \tilde{D}_{zu}\tilde{D}_{zu}^T\right)\tilde{C}_z \quad (3.14)$$

$$\hat{B}_w = B_w\left(I - \tilde{D}_{yw}^T\tilde{D}_{yw}\right) \quad (3.15)$$

S_u and S_y are internal scalings such that

$$\begin{aligned} \tilde{B}_u &= B_u S_u^{-1} & \tilde{C}_y &= S_y C_y \\ \tilde{D}_{zu} &= D_{zu} S_u^{-1} & \tilde{D}_{yw} &= S_y D_{yw} \end{aligned} \quad (3.16)$$

For H_2 optimization the compensator K will be of the same order as the plant P .

For a more thorough description of H_2 and H_∞ optimization see reference [8].

3.2 Design Techniques

The first step in the optimal control design sequence is building the P matrix, followed by calculating the stabilizing and minimizing compensator K using H_2 or H_∞ optimization, then simulating the compensator with the truth model to determine if the desired performance is achieved. Overall, this is an iterative process in which the control

weightings in P are used like "dials" to "tune" system performance. It is important that the nominal plant model is used in building P to keep the order of the compensator to a minimum.

A key tool for building the P matrix is the use of a state-space block diagram shown in Figure 3-2 representing the transfer function

$$G(s) = C(sI - A)^{-1}B + D. \quad (3.17)$$

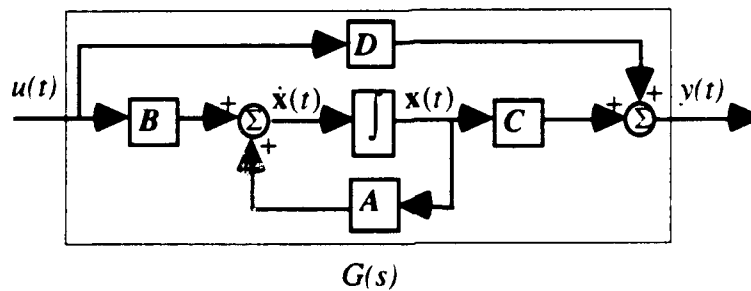


Figure 3-2 State-Space Block Diagram Form

Once an optimal control problem is set up with the system plant, coloring filters, and control weightings represented in state-space block diagram form, it is easy to augment all the states into one state-space representation of the entire system. That state-space representation is Eqns. 3.5, which as discussed earlier, define the P matrix.

A designer has many configurations to choose from when setting up the optimal control problem. There are two basic optimal control design setups which are presented in this section. Starting with a basic setup, control weightings are added depending on the performance requirements of the system, such as weightings on control usage, states, sensitivity, complementary sensitivity, and tracking. The two configurations presented represent configurations of two of the final controller designs for the SBD.

3.2.1 Unity Feedback Setup. The unity feedback setup shown in Figure 3-3 has a constant weighting R_c on control usage $u(t)$, a constant weighting H' on the states $x_p(t)$,

and a dynamic weighting W_s on sensitivity. The blocks A_p , B_p , and C_p are the state-space representation of the nominal plant $Gp(s)$. The controller K is replaced with G_c and is not represented in state-space form because it is not part of the P matrix. W_d is the plant disturbance coloring filter and Γ is a constant matrix used to distribute the disturbance to the proper state. The inputs w_1 and w_2 are zero-mean, white Gaussian noise of unit intensity, where w_1 is the disturbance input and w_2 represents sensor noise. The reference command $\theta_c(t)$ is not actually part of the setup for building the P matrix, but is shown to make the system complete. This means that command following is not directly optimized in the unity feedback setup. Robust state regulation is the real objective of this setup. In fact, if the dynamic sensitivity weighting W_s is not included, H_2 optimization on this setup is the same as the standard linear quadratic Gaussian (LQG) problem of minimizing the cost function

$$J = \int_0^{\infty} (x^T Q x + u^T R u) dt \quad (3.18)$$

where

$$Q = H^T H \quad \text{and} \quad R = R_z^T R_z \quad (3.19)$$

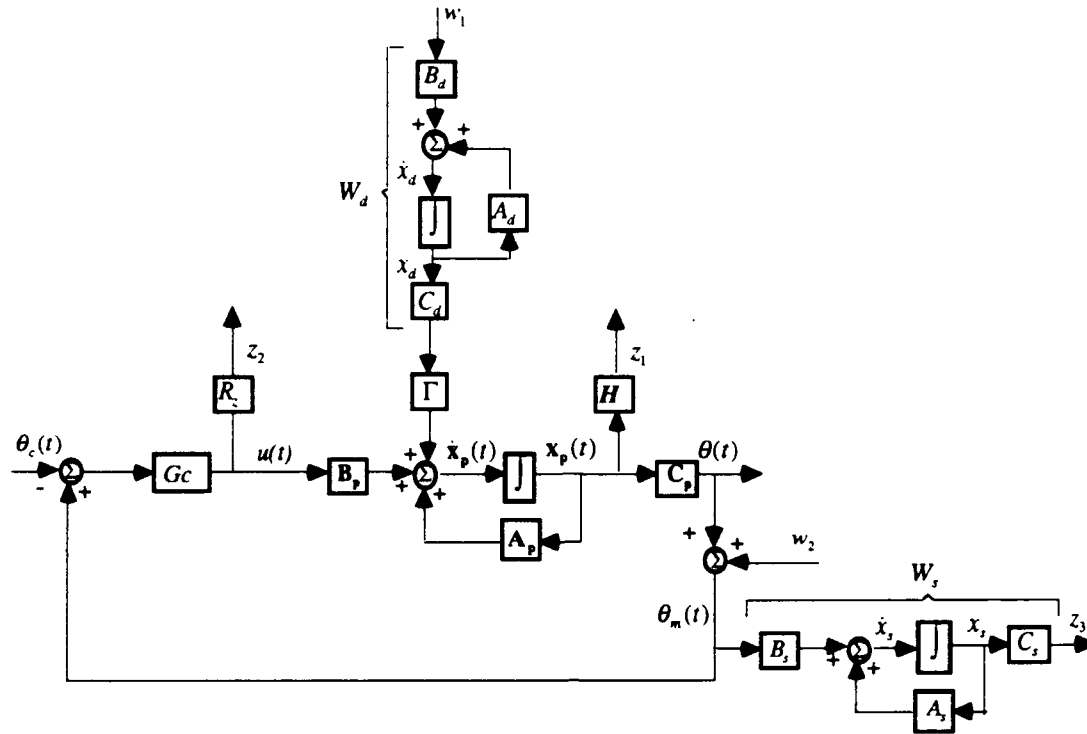


Figure 3-3 Unity Feedback Setup

Although good command input tracking is not a direct specification in this setup, it is indirectly achieved by use of the dynamic sensitivity weighting W_s . The term sensitivity refers to the output's sensitivity to plant uncertainties and/or disturbances and is defined in the SISO case as

$$S = \frac{1}{1 - G_p G_c} \quad (3.20)$$

It is desirable in the case of the SBD for the system to be insensitive to low frequency plant disturbances, thus S would have a general shape like that shown in Figure 3-4.

"General" is stressed because this discussion assumes that the plant disturbance is coming in at the plant output, where, in the case of the SBD the disturbance is actually a torque disturbance into the gimbal. The difference is elaborated when discussing the actual SBD

design in Chapter 4. S being "small" at low frequency is achieved by making G_c "large" or having high gain at low frequency. High gain at low frequency also yields good tracking as seen in the closed-loop tracking error response to the reference command and plant disturbance.

$$err = -\frac{1}{1 - G_p G_c} \theta_c + \frac{W_d}{1 - G_p G_c} w_1 \quad (3.21)$$

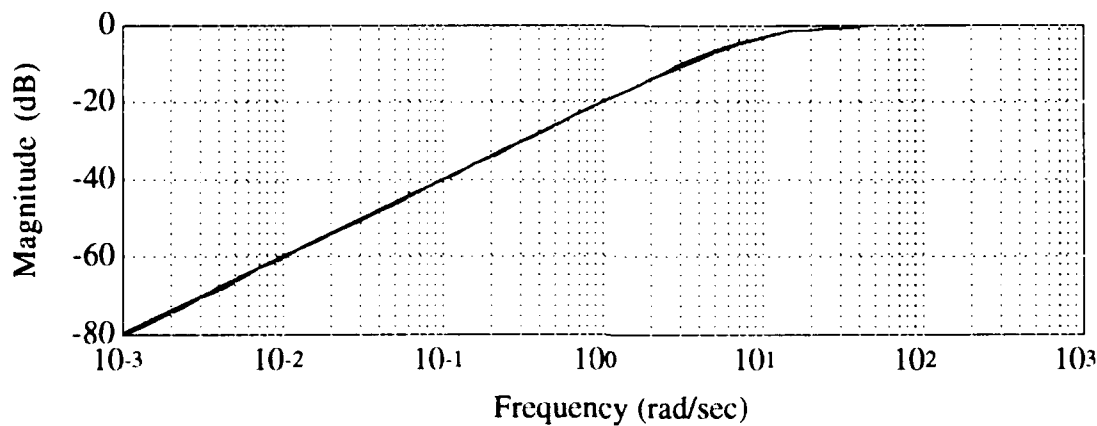


Figure 3-4 General Shape of Sensitivity

3.2.1.1 Control Weighting Rationale. Choosing control weighting values is not an exact science; rather it is an iterative process. However, it is important to understand the effects of the different weightings to provide a starting point.

The control usage weighting R_z must always be included and have a D term in the optimal control setup or condition iv) will be violated and the problem will be singular. Theoretically, if $R_z = 0$ there is no penalty on control usage allowing an infinite amount of control power to achieve the system requirements. R_z can be a dynamic weighting if, for example, it is desired to restrict high frequency control usage. The next chapter will

address that requirement. The effects of R_z can be seen by looking at the closed-loop transfer function of z_2 to w ,

$$z_2 = \frac{R_z G_c W_d}{1 - G_p G_c} w_1 + \frac{R_z G_c}{1 - G_p G_c} w_2 \quad (3.22)$$

As R_z is increased, the minimization of T_{zw} will yield a decreasing G_c , or in other words, less control usage.

The state weighting H can be used to minimize some states more than others. For example, in the case of the SBD system, if it were necessary to limit the velocity of the gimbal a large weighting would be put on the state $\dot{\theta}(t)$.

The sensitivity weighting W_s is chosen to achieve the desired S by picking it to generally look like $1/S$; therefore, W_s would have high gain at low frequency. W_s must roll off such that it does not contain a D term and violate condition i). The magnitude and bandwidth would depend on the severity of the disturbance input W_d and the command following requirements, i.e., step, ramp, speed of response, ect. The effects of sensitivity weighting can be seen by looking at the closed-loop transfer function of z_3 to w ,

$$z_3 = \frac{W_s W_d}{1 - G_p G_c} w_1 + \frac{W_s}{1 - G_p G_c} w_2 \quad (3.23)$$

As the low frequency magnitude of W_s is increased and/or the bandwidth is increased minimization of T_{zw} will yield an increasing G_c approximately over the same bandwidth. Note that if W_s is given a relatively small low frequency gain, minimization would still yield G_c with high gain at low frequency because the disturbance coloring filter W_d has high gain at low frequency. However, the controller would typically fall short of the desired performance, thus the "dial" W_s is needed to "tune" the performance.

3.2.1.2 Building the P Matrix. The augmented state-space representation of the optimal control setup in Figure 3-3 is described by Eqns. 3.5. P is then formed by Eqn 3.6 where,

$$\begin{aligned}
 A &= \begin{bmatrix} A_p & \Gamma C_d & 0 \\ 0 & A_d & 0 \\ B_s C_p & 0 & A_s \end{bmatrix} & B_w &= \begin{bmatrix} 0 & 0 \\ B_d & 0 \\ 0 & B_s \end{bmatrix} & B_u &= \begin{bmatrix} B_p \\ 0 \\ 0 \end{bmatrix} \\
 C_z &= \begin{bmatrix} H & 0 & 0 \\ 0 & 0 & 0 \\ 0 & 0 & C_s \end{bmatrix} & D_{zw} &= \begin{bmatrix} 0 & 0 \\ 0 & 0 \\ 0 & 0 \end{bmatrix} & D_{zu} &= \begin{bmatrix} 0 \\ R_z \\ 0 \end{bmatrix} \\
 C_y &= [C_p \quad 0 \quad 0] & D_{yw} &= [0 \quad 1] & D_{yu} &= [0]
 \end{aligned} \tag{3.24}$$

3.2.1.3 H_2 and H_∞ Algorithms. Once the P matrix has been built there are several H_2 and H_∞ algorithms that take the P matrix as an input and then output the stabilizing and minimizing controller in state-space form. All the algorithms listed are Matlab script M-files: h2lqg and hinf are found in the Robust-Control Toolbox; hinfsyn and hinfli are H_∞ routines found in the relatively new μ -Tools that calculate output feedback sub-optimal controllers and full state feedback sub-optimal controllers, respectfully; h2opt and hinf5 are user friendly algorithms used in this thesis and were written by Dr. Brett Ridgely.

3.2.2 Two-Degree of Freedom Controller Setup. The two degree of freedom controller setup shown in Figure 3-5 is a method which allows for the direct design of command following or tracking performance. This setup fits into the standard optimal control setup of Figure 3-1, where $u = Ky$, with K partitioned as

$$K = [Gc_1 \quad Gc_2] \quad (3.25)$$

and

$$y = \begin{bmatrix} \theta_m \\ \theta_c \end{bmatrix} \quad (3.26)$$

The control weightings R_z and H are used in the same manner as with the unity feedback setup. W_t is a dynamic track weighting that is used to directly minimize tracking error. The effect of W_t can be seen in the transfer function of z_3 to w ,

$$z_3 = \frac{W_t W_d}{1 - Gc_1 Gp} w_1 + \frac{W_t Gc_1}{1 - Gc_1 Gp} w_2 + \left(\frac{W_t Gc_2}{1 - Gc_1 Gp} - W_t \right) w_3 \quad (3.27)$$

Tracking performance is normally measured in terms of the ability of a system to track step or ramp inputs; therefore, emphasis of W_t should be high gain at low frequency. An example of what W_t would generally look like is shown in Figure 3-6. An indirect result of this setup, with the disturbance coloring filter W_d having high gain at low frequency, is good sensitivity or disturbance rejection in the feedback loop. It can be seen from Eqn. 3.27 that minimization of T_{zw} will tend to make Gc_1 large at low frequency.

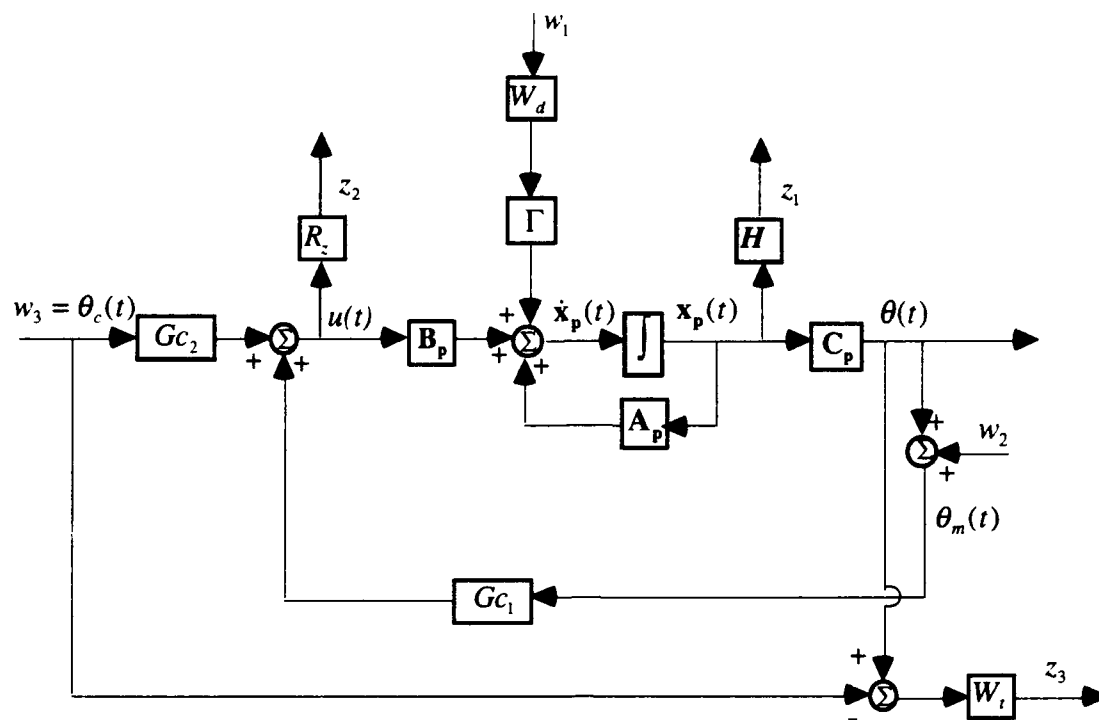


Figure 3-5 Two Degree of Freedom Controller Setup

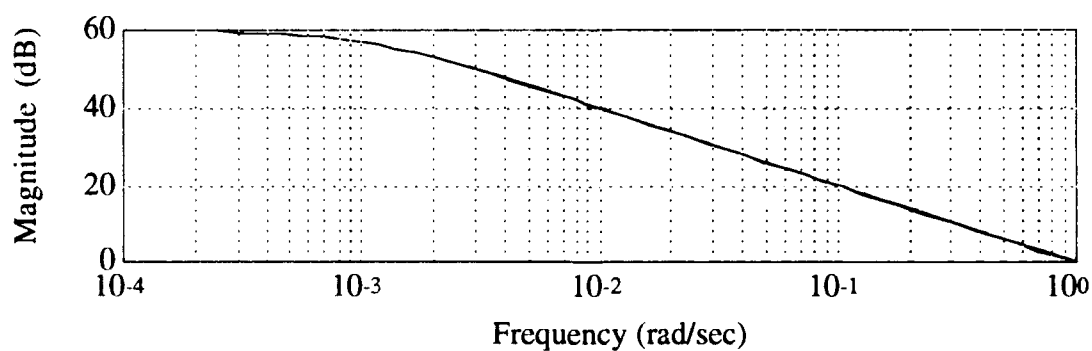


Figure 3-6 Track Weighting

IV. SBD Azimuth Axis Controller Design

4.1 Introduction

This chapter is devoted to a detailed description of the two basic design setups for the azimuth axis. The simulation results of the H_2 optimal two degree of freedom controller are also presented in this chapter, while the results of the H_2 optimal unity feedback controller are presented in Chapter 5. The Matlab M-files used for building the P matrix, for synthesizing the H_2 optimal controller, and for performance analysis are included in Appendix B. A tutorial of the H_2 optimization M-file `h2opt` and M-files specifically written for the SBD controller design is given in Appendix D.

4.2 Scaling Problem

Both the H_2 and H_∞ algorithms had numerical problems with the large controller gain required to achieve μrad tracking performance. The H_2 problem was solved by scaling the plant $Gp(s)$ to microradian output. Therefore, the resulting controller $Gc(s)$ had 10^6 less gain than it would have had with an unscaled plant. H_2 optimization was performed with the scaled plant and simply increasing the resulting controller by 10^6 rescaled the system. The scaling equations were

$$Gp(s)_{\text{scaled}} = Gp(s) \times 10^6 \quad \& \quad Gc(s) = Gc(s)_{\text{scaled}} \times 10^6 \quad (4.1)$$

where $Gc(s)_{\text{scaled}}$ was the controller yielded by the algorithm.

The H_∞ problem was not as straightforward, and all internal system scaling attempts yielded less than completely successful results. In-depth investigation of the scaling problem H_∞ had with the model was beyond the scope of this thesis; therefore, the H_∞ solution was not pursued any further.

4.3 Position Command Inputs

Although in-depth performance analysis is presented in Chapter 5, some analysis is done in this chapter. Therefore, it is appropriate at this time to describe the position command inputs used to determine performance.

Step response performance was baselined against a 100 μ rad step input; however, tracking commands for a beam director, whether tracking a star or a fast moving low-earth satellite, are more accurately described by a ramp input. For the SBD simulation the step sizes chosen for the ramp were 500 μ rad. With a servo loop sample rate of 200 Hz this was equivalent to 0.1 rad/sec or approximately 6° per second, which approaches the maximum azimuth axis velocity of 10° per second.

A true test of performance is to simulate a system with a command input that represents real ephemeris data of a low-earth orbit satellite near culmination, for this is when the azimuth axis is at maximum velocity. A five second sample of position and velocity data extracted from ephemeris data generated at the SBD is shown in Figures 4-1 and 4-2, respectively. Like the ramp command, the gimbal velocity due to the ephemeris command had an average value of approximately 6° per second. However, as seen in Figure 4-2 there was an acceleration component in the ephemeris data, which made the tracking problem more difficult. The position data was edited such that the initial position was 0.0 and that it represented an ascending portion of a satellite pass. The original data was from a descending portion of a pass. This five second sample of data was used for all ephemeris command tracking simulations.

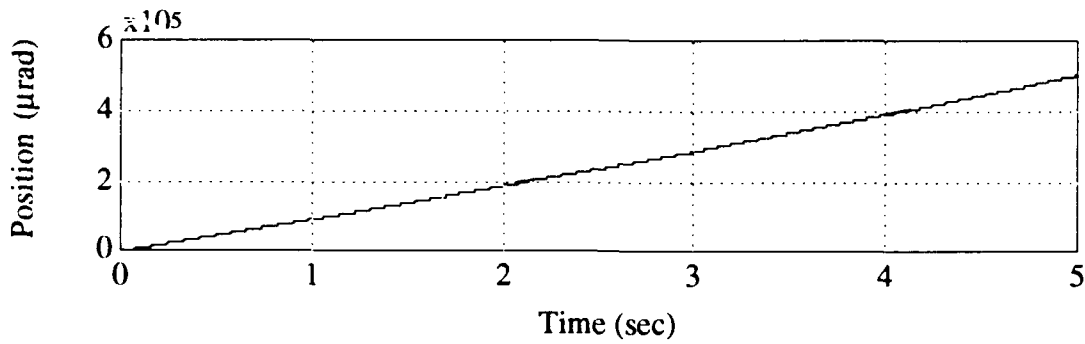


Figure 4-1 Position Command Input

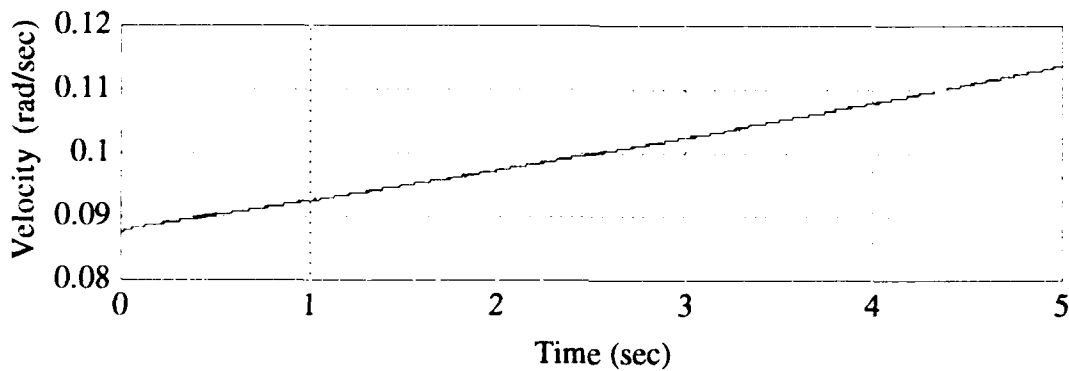


Figure 4-2 Velocity Derived From Position Command

4.4 Unity Feedback Design

Figure 4-3 shows the design setup, where the sensitivity weighting W_s was used for plant disturbance rejection and indirectly for good tracking performance. As stated in Section 3.2.1, sensitivity is defined for a disturbance added to the plant's output. The disturbance w_1 actually entered as a torque disturbance to the gimbal. However, setting up the optimal control problem with the disturbance modeled as torque yielded controllers of marginal performance for all weightings W_s that were tried. Therefore, the optimal control P matrix was built with w_1 entering as a position disturbance at the plant's

output and the simulation had the disturbance entering as torque. The same disturbance coloring filter W_d was used for both the controller design and the simulation (see Figure 2-15). It would seem that the disturbance entering as torque would not be the same as the disturbance entering as position in μrad , because the torque disturbance goes through the gimbal dynamics, which is practically a double integrator. However, in this case, the random white noise generated by Matlab contained the appropriate low frequency spectrum such that the open loop feed-through of the torque disturbance was almost the same as the disturbance spectrum in μrad .

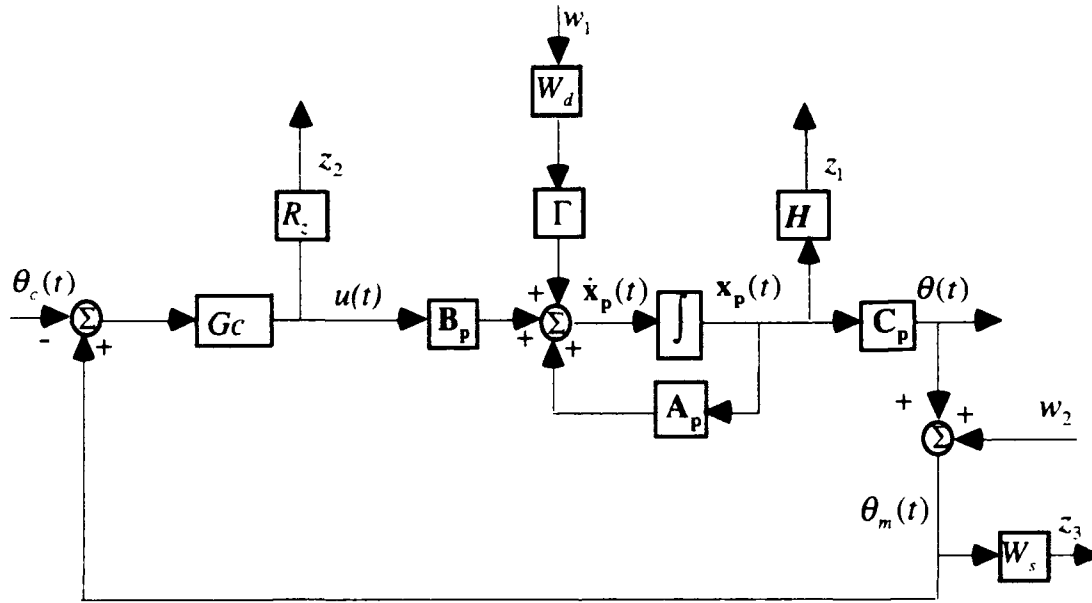


Figure 4-3 Unity Feedback Setup

4.4.1 Control Weightings. The control weightings used in the setup were the control usage weighting R_z , the state weighting H , and the sensitivity weighting W_s . Larger values of R_z yielded controllers of lower gain and vice versa. The final value chosen was $R_z = 1$. The nominal plant, where the only dynamics included were that of the gimbal, had two states, $\theta(t)$ and $\dot{\theta}(t)$. It was not necessary to weight the states for the

purpose of minimizing the amplitude of a particular state, which is normally the main objective of the state weighting H . However, including some weighting proved to yield a system with slightly better gain and phase margins than when a weighting was not included. The final value chosen was a weighting of 1 on both states such that

$$H = \begin{bmatrix} 1 & 0 \\ 0 & 1 \end{bmatrix} \quad (4.2)$$

The fact that including a weighting on the states resulted in better stability robustness warrants further explanation. Consider the perturbed plant $\tilde{G}p(s) = (1 + \Delta)Gp(s)$ modeled as output multiplicative uncertainty, where $Gp(s)$ is the nominal plant and Δ is the uncertainty. The closed-loop block diagram corresponding to the controller and this representation of the plant is shown in Figure 4-4. Now consider the case where $\Delta = 1$; the closed-loop transfer function of T_{zw} is equal to complimentary sensitivity T , where

$$T = \frac{C_p (sI - A_p)^{-1} B_p G_c}{1 - G_p G_c} \quad (4.3)$$

$Gp(s)$ in the numerator is represented in its state-space transfer function form for demonstration. Minimization of complimentary sensitivity provides increased stability robustness; therefore, minimization of the transfer function T_{zw} yields better gain and phase margins [9:53-54].

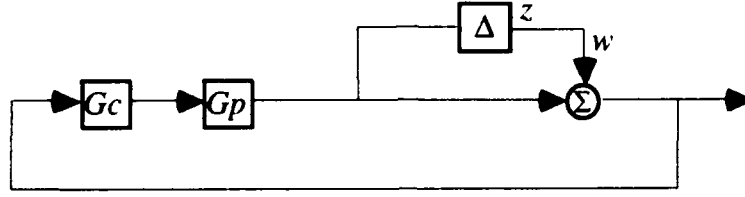


Figure 4-4 Output Multiplicative Uncertainty Block Diagram

Now consider the block diagram in Figure 4-5, which represents part of the closed-loop unity feedback setup for the SBD system. z_1 is the state control output and w_2 is the sensor noise input. Indirectly, the state weighting H provides for output multiplicative uncertainty such that the transfer function of $T_{z_1 w_2}$ is similar to the complimentary sensitivity, thus resulting in better stability robustness. It is clear that the complimentary sensitivity T in Eqn. 4.3 is similar to $T_{z_1 w_2}$, where

$$T_{z_1 w_2} = \frac{H(sI - A_p)^{-1} B_p G_c}{1 - G_p G_c} \quad (4.4)$$

and

$$C_p = \begin{bmatrix} 1 & 0 \end{bmatrix} \quad H = \begin{bmatrix} 1 & 0 \\ 0 & 1 \end{bmatrix} \quad (4.5)$$

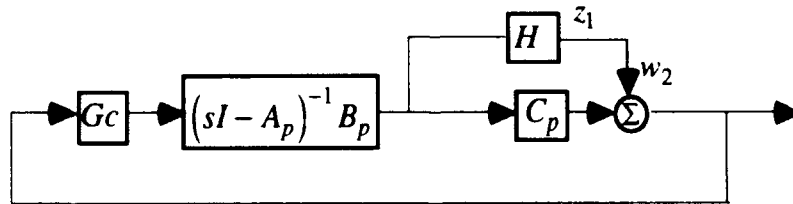


Figure 4-5 Closed-Loop State Weighting Block Diagram

The key to designing a good controller was in the sensitivity weighting. After many iterations of "dialing" W_s , the final had a low frequency gain of 2×10^4 and a pole at $s = -10^{-4}$ rad/sec (see Figure 4-6). The high gain of W_s was necessary to achieve the system bandwidth and high gain at low frequency needed to reject the plant disturbance. The low frequency pole gave the controller a near integrator necessary for command input tracking and rejection of the non-linear bearing friction disturbance, which is discussed further in Chapter 5. The state-space representation of W_s is

$$\begin{aligned}\dot{x}_s(t) &= A_s x_s(t) + B_s \theta_m(t) \\ z_3 &= C_s x_s(t) + D_s \theta_m(t)\end{aligned}\tag{4.6}$$

Where z_3 is the controlled output, $x_s(t)$ is the sensitivity weighting state, and $\theta_m(t)$ is the measured gimbal position. The state-space values are,

$$\begin{aligned}A_s &= -0.0001 & B_s &= 1 \\ C_s &= 2 & D_s &= 0\end{aligned}\tag{4.7}$$

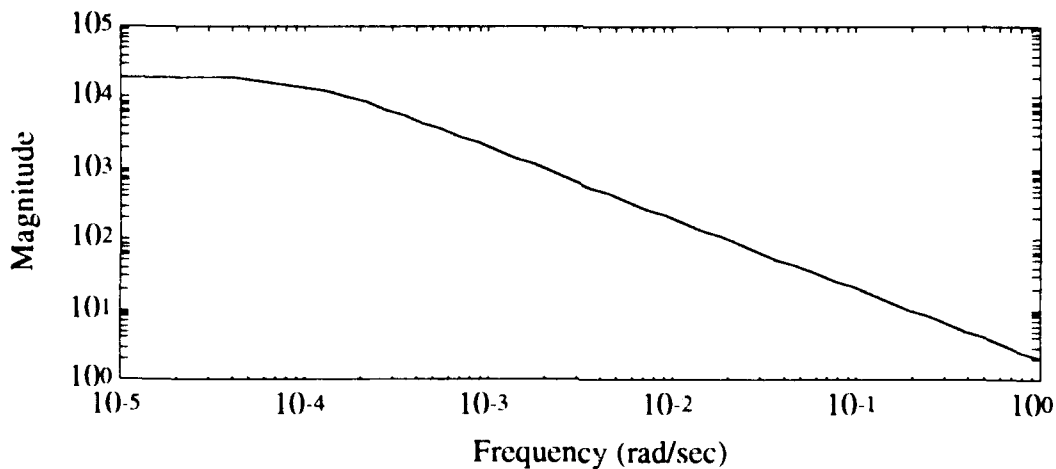


Figure 4-6 Sensitivity Weighting

4.4.2 H_2 Controller Synthesis. With the nominal plant, exogenous inputs, and control weightings defined in state-space form, the P matrix, described by Eqns. 3.24 was built. The Matlab M-file `h2opt` was used to synthesize the H_2 optimization controller. As stated earlier, optimal control produces controllers of the same order as the plant P ; thus, with a 2nd order nominal plant, one pole in W_d , and one pole in W_s , the resulting controller was 4th order.

4.4.3 Controller Fine Tuning. The controller produced by the weightings presented in Section 4.4.1 exceeded the tracking and disturbance rejection requirements. However, the controller contained relatively high gain at high frequency; in other words, it did not roll off rapidly after the bandwidth of the system. The scope of this thesis did not include the consideration of the gimbal's resonant frequencies, and as stated earlier notch filtering would have to be implemented. However, knowing that the resonant frequencies exist, it was important to roll off the controller as rapidly as possible without effecting the bandwidth or decreasing the gain and phase margins to unacceptable levels. There were two ways to correct this problem: one was to put a dynamic weighting W_{Rz} on control usage to minimize high gain at high frequency, and the other was to "manually" grab the high frequency poles in the controller and place them at lower frequency, thus rolling off the controller immediately after the bandwidth. Figure 4-7 compares the magnitude frequency responses of the original controller, the controller yielded from the dynamic weighting W_{Rz} design, and the controller resulting from placing the poles manually.⁵ Table 4-1 shows the gain margin, phase margin, and the bandwidth. For positive feedback, the gain and phase margins are taken from the open loop system $-GpGc$, while the bandwidth is defined as the 0 dB cross-over frequency ω_c of $|-GpGc|$. Reducing high frequency control power has a negative effect of reducing robustness, but the gain and phase margins are adequate for all the controllers. The pole placement

⁵The controllers have been rescaled to include the 10^6 gain.

controller had the best simulated performance of all three, and thus was chosen as the final design for the azimuth axis controller.

The next two sections elaborate on the methods used to reduce the high frequency gain of the original H_2 controller.

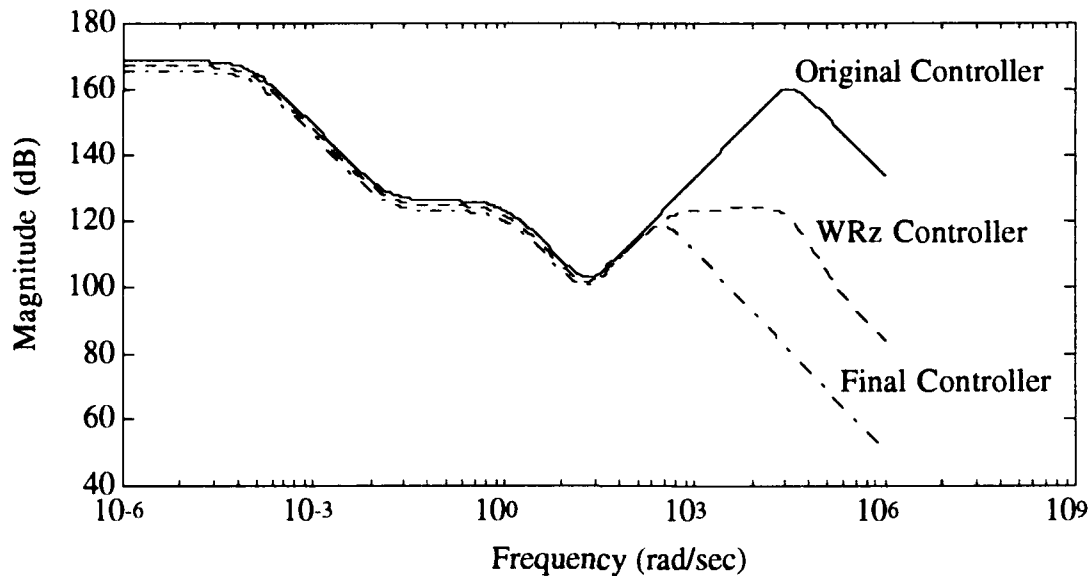


Figure 4-7 Controller Magnitude Frequency Response

Table 4-1 Unity Feedback Controller Comparison

Controller Design	Gain Margin (dB)	Phase Margin (Degree)	ω_c (rad/sec)
Original H_2	(-11.7, 16)	± 50	52
Control Usage Weighting W_{Rz}	(-10.8, 15)	± 42	48
Final	(-10.5, 11)	± 36	52

4.4.3.1 Control Use Weighting. The weightings used for the original H_2 design did not put any restriction on high frequency control use. As such, they met all the objectives stressed by the weightings, but the controller contained high gain at high

frequency. By using a dynamic weighting on control usage W_{R2} , shown in Figure 4-8, the minimization of high frequency control usage was achieved. A second order weighting would have rolled the controller off quicker without effecting bandwidth; however, the compensator would have been 6th order. Being that it was desirable to keep the order to a minimum and that this was a relatively simple SISO system, there was a more effective way of rolling off the controller.

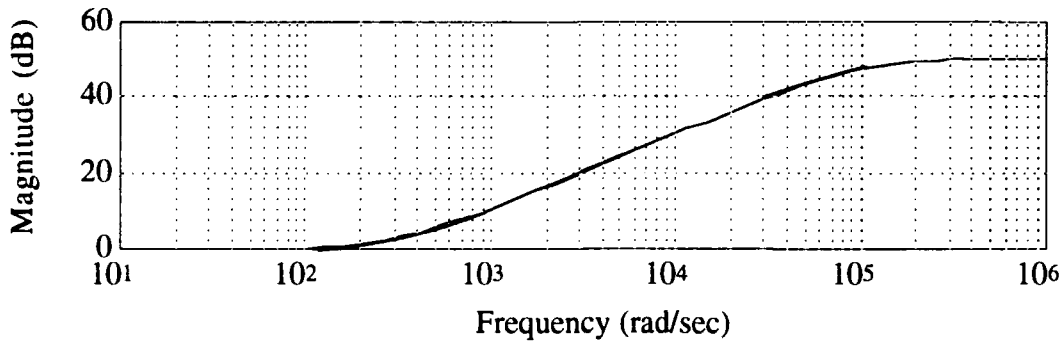


Figure 4-8 Control Usage Weighting

4.4.3.2 "Manual" Pole Placement. A closer look at the compensator yielded by H₂ optimization, after rescaling, revealed that a complex pair of poles were placed at high frequency.

$$G_c(s) = \frac{-4.5342 \times 10^{12} (s + 0.013462)(s^2 + 29.4s + 441.1073)}{(s + 0.0001)(s + 0.99996)(s^2 + 44329s + 1.002624 \times 10^9)} \quad (4.8)$$

After carefully decreasing the frequency of the complex pair, keeping the damping ratio of the complex pair and system bandwidth the same, and keeping the gain and phase margins acceptable, the resulting controller was

$$G_c(s) = \frac{-360 \times 10^6 (s + 0.013462)(s^2 + 29.4s + 441.1073)}{(s + 0.0001)(s + 0.99996)(s^2 + 424s + 90000)} \quad (4.9)$$

The compensator in Eqn. 4.9 was the final design used in the comparison with the current controller and its performance analysis is presented in Chapter 5. The rescaled negative feedback state-space representation of this controller is found in Appendix A. Although the gain and phase margins differed between this compensator and the original of Eqn. 4.8, they had the same performance, i.e. disturbance rejection, speed of response, and tracking error, but the original design had substantially more control power at frequencies past the system bandwidth. For example, comparison of the two controllers tracking five seconds of real ephemeris data revealed the motor torque of the original controller system was 644 ft-lbs RMS, and the final design had 244 ft-lbs RMS.

Again, since this was a SISO system, the task of grabbing the poles and dragging them to lower frequency was relatively straightforward. However, had this been a complex MIMO system, manually moving the poles could have been difficult and dangerous, because stability is not guaranteed as it is when using a control usage weighting and H_2 optimization.

4.5 Two-Degree of Freedom Controller Design

Figure 4-9 shows the two-degree of freedom controller design setup, where the track weighting W_t was used to minimize tracking error and indirectly to yield good disturbance rejection. The disturbance coloring filter W_d and the control weightings R_z and H had the same values as those used in the unity feedback design. W_t was designed with high gain at low frequency to emphasize step and ramp tracking. Two of the more successful W_t designs are presented: the first had a low frequency gain of 60 dB and a stable pole at 10^{-3} rad/sec; the second had a low frequency gain of 180 dB, one stable pole at 10^{-5} rad/sec, and another stable pole at 10^{-3} rad/sec. The latter is shown in Figure 4-10. The double pole W_t yielded a system with higher gain at low frequency while maintaining the same bandwidth.

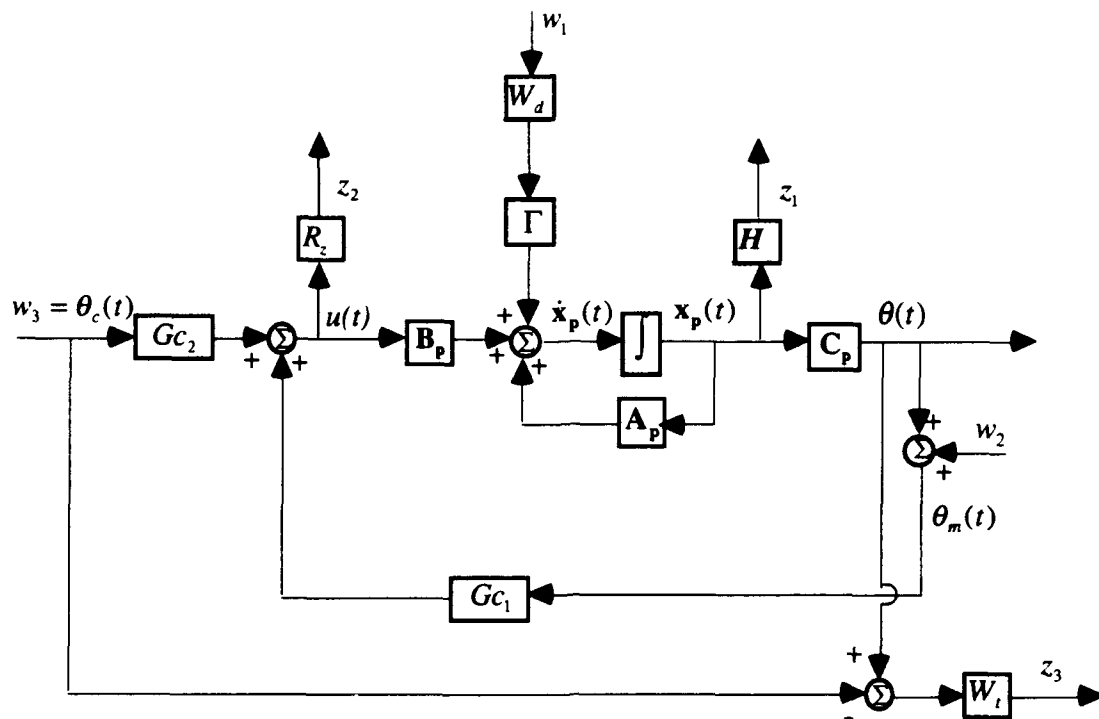


Figure 4-9 Two Degree of Freedom Controller Setup

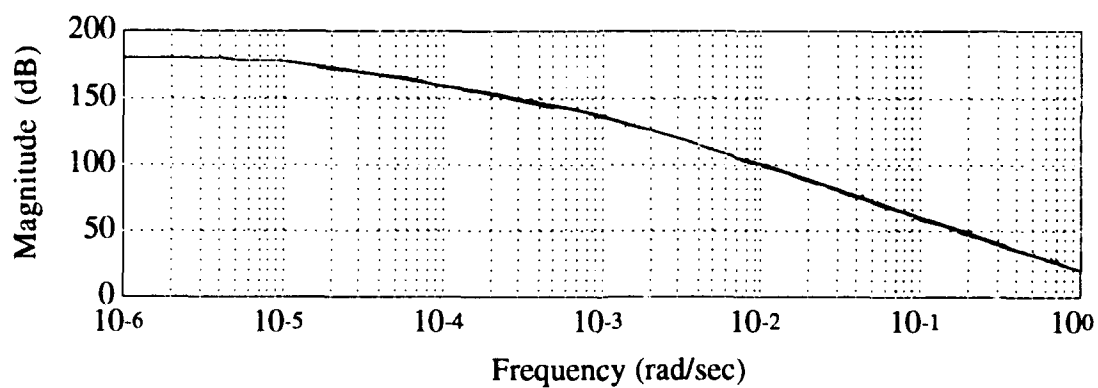


Figure 4-10 2nd Order Track Weighting

Gain and phase margins and bandwidth, listed in Table 4-2, for the two degree of freedom controller are dependent on the feedback loop of $-G_p G_c_1$; the preprocessor G_c_2

does not effect system stability. The margins were adequate and the bandwidth was sufficient for speed of response and disturbance rejection.

Table 4-2 Two Degree of Freedom Controller Comparison

Controller Design	Gain Margin (dB)	Phase Margin (Degree)	ω_c (rad/sec)
1 st Order W_t	(-11.8, 20)	± 51	46
2 nd Order W_t	(-7.5, 20)	± 50	47

Figures 4-11 and 4-12 show the step and ramp responses of both controller designs, respectfully. The 1st order weighting yielded a system with a fast, well damped step response; however, the ramp tracking response had an extremely large steady state error. The 2nd order weighting yielded a system with a fast, poorly damped step response and a ramp response with acceptable steady state error of approximately 1 μ rad. The steady state error is clearly seen in Figure 4-13, where the ramp response had been truncated to remove the initial transient response. Figure 4-14 shows the tracking error to ephemeris command input. The truncated data from the ephemeris command tracking error response shown in Figure 4-15 revealed that even the 2nd order track weighting system had poor steady state error. A third order track weighting design was attempted to cope with ephemeris tracking, but was unsuccessful. A gimbal velocity initial condition was given in the simulation of the ramp and ephemeris command input to prevent the initial transient from being too severe. As seen in the figures, the initial transients were still extremely large. Therefore, even if the steady state error was adequate, none of the two degree of freedom designs were acceptable for ramp or ephemeris command tracking.

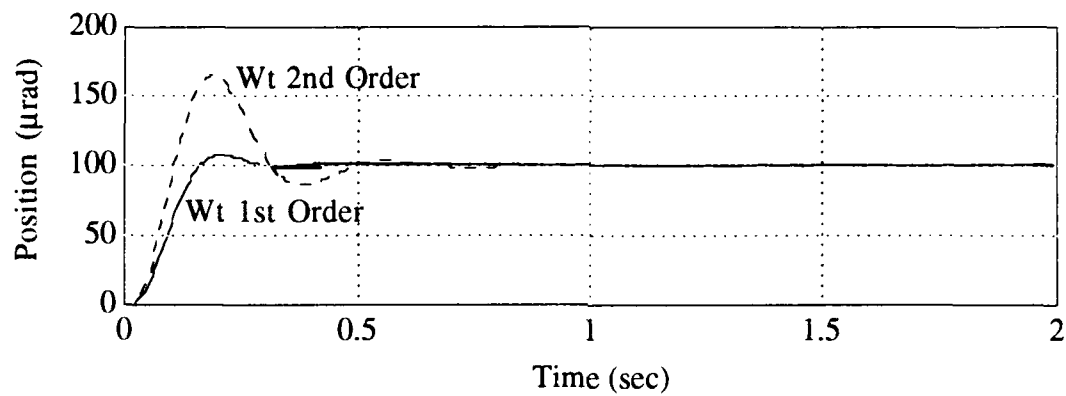


Figure 4-11 Step Response

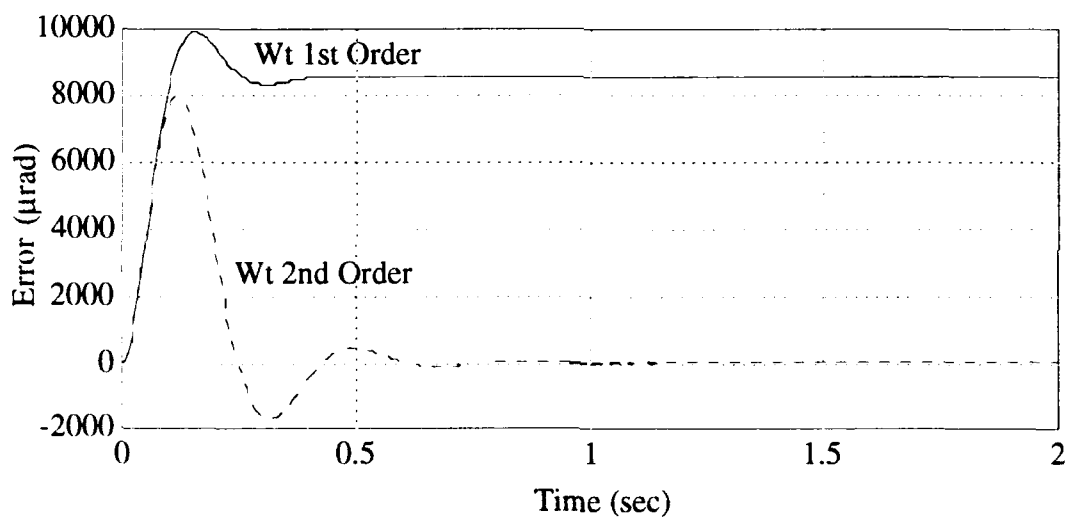


Figure 4-12 Tracking Error to Ramp Command

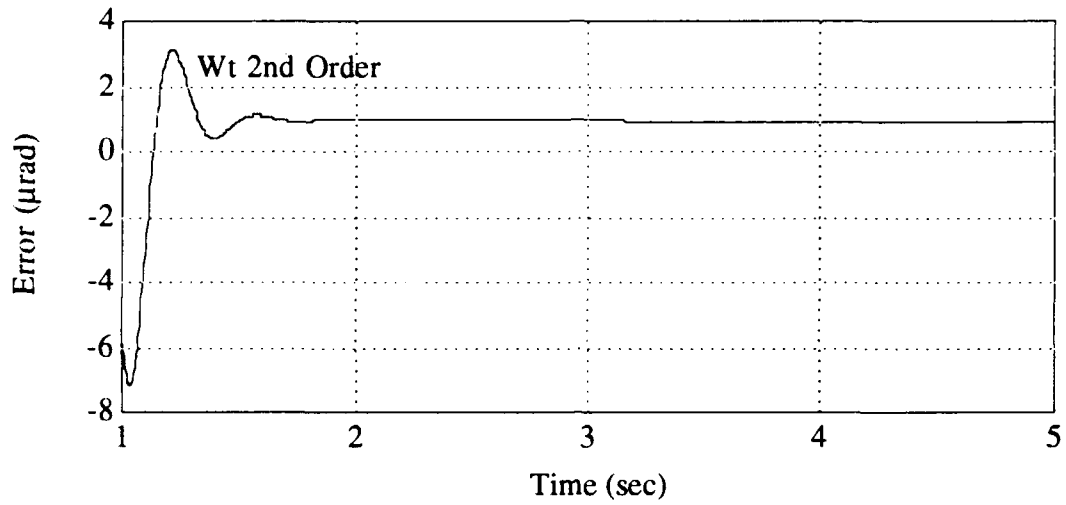


Figure 4-13 Truncated Tracking Error to Ramp Command

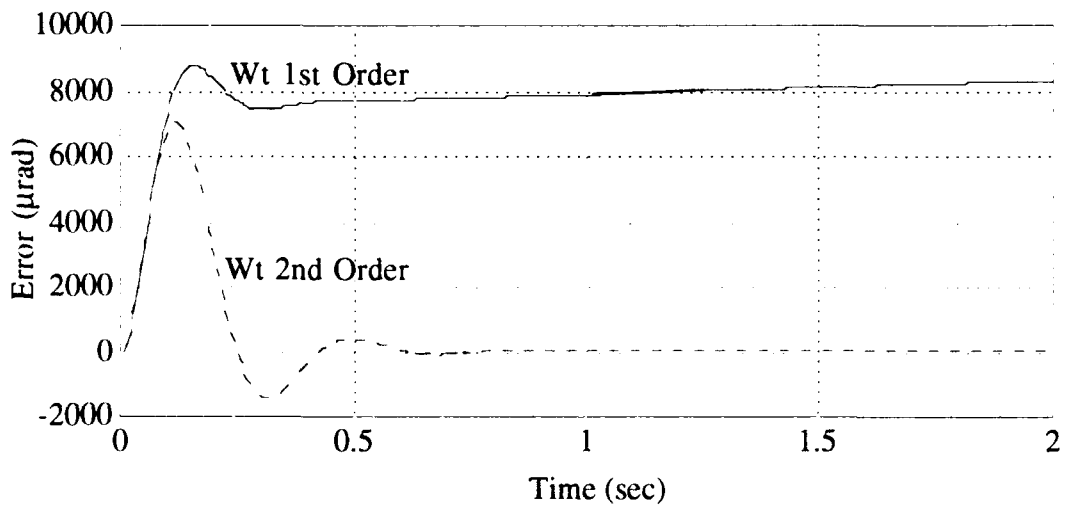


Figure 4-14 Tracking Error to Ephemeris Command

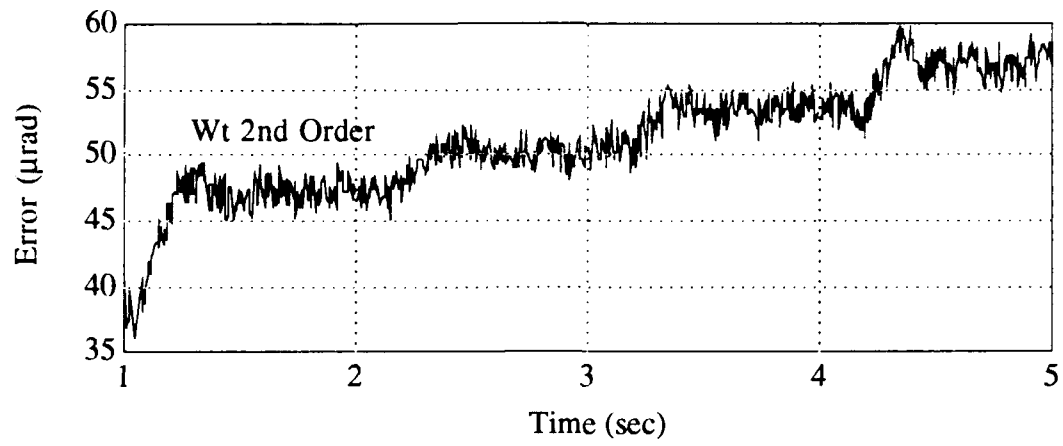


Figure 4-15 Truncated Tracking Error to Ephemeris Command

V. Azimuth Axis Simulations and Results

5.1 Introduction

This chapter provides detailed comparison of the final azimuth axis H_2 optimization unity feedback controller and the azimuth axis controller currently being used at the SBD. Comparison is based on simulations performed with the controllers and the SBD truth model developed in Chapter 2. The Simulink models used for simulations are shown in Appendix C, and a tutorial on the execution of the models is included in Appendix D.

5.2 Controller Comparison

The open-loop Bode frequency responses of $Gp(s)Gc(s)$ for the current SBD system and $-Gp(s)Gc(s)$ for the H_2 system are shown in Figures 5-1 and 5-2, where $Gp(s)$ is the truth model. Recalling that the H_2 controller is based on positive feedback, the open-loop Bode frequency response is defined as $-Gp(s)Gc(s)$. The current SBD system is very robust with gain margins of (-35 dB, 16 dB) and phase margin $\pm 60^\circ$. The system with the H_2 controller is not as robust, but has adequate gain margins of (-10.5 dB, 11 dB) and phase margin $\pm 36^\circ$. The bandwidths for the current and H_2 systems are 49.7 rad/sec or 7.9 Hz and 51.6 rad/sec or 8.2 Hz, respectively.

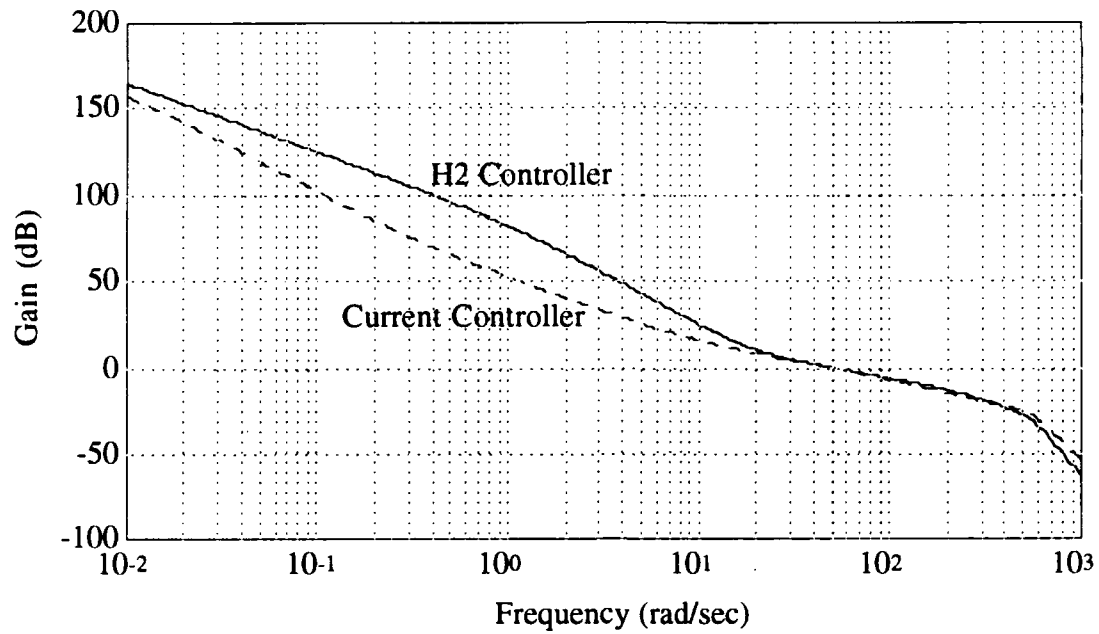


Figure 5-1 Bode Magnitude Frequency Response

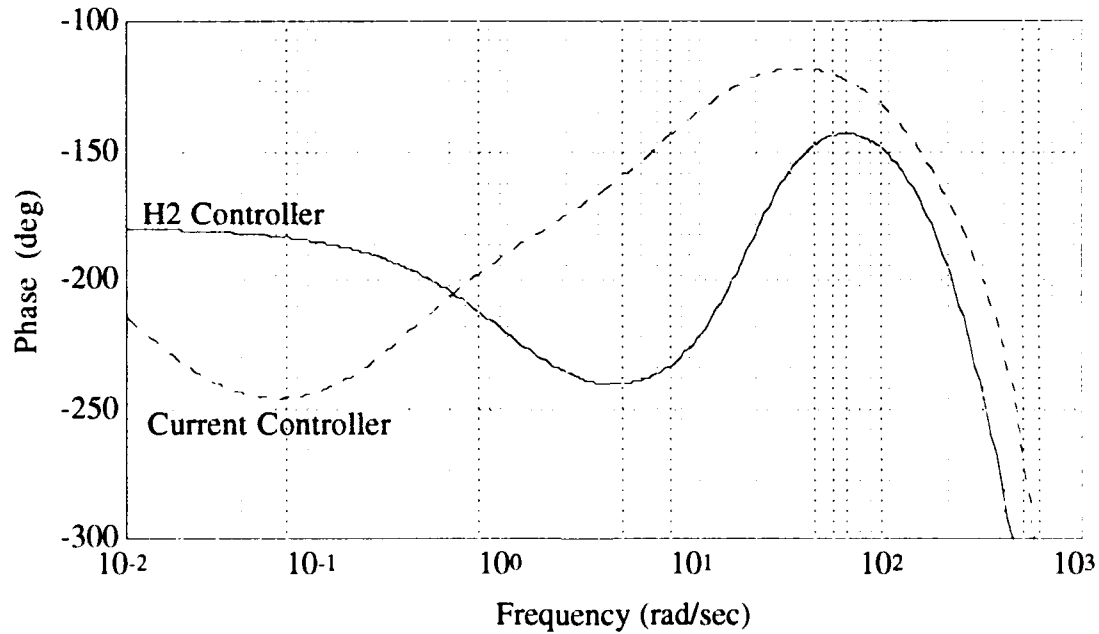


Figure 5-2 Bode Phase Frequency Response

5.2.1 Current SBD Controller. The current SBD azimuth axis controller is described by the transfer function

$$G_c(s) = \frac{10^6(s+0.3)(s+8.1)}{s(s+256)} \quad (5.1)$$

The controller is designed in a classical sense in that it consists of PI control and a lead, where high gain and the lead are required to achieve the necessary bandwidth for speed of response and plant disturbance rejection, and the integrator is necessary to provide a near type 3 system to track the parabolic ephemeris command with zero steady state error. "Near" type 3 is used to describe the system because the gimbal dynamics have one pure integrator and one "near" integrator, a low frequency pole due to the damping effect of viscous friction as described in Chapter 2.

An integrator in the compensator is also needed to reject the non-linear bearing friction. When the bearings are rolling the constant running friction torque T_c of 16 ft-lbs is like a step torque disturbance input. The definition of system type for unity feedback is based on the reference command input to the controller, not as an input disturbance to the plant; therefore, even though the gimbal is practically a double integrator it does not necessarily yield zero steady state error to a step torque disturbance. It can be seen from Eqn. 5.2 that $G_c(s)$ must contain an integrator to achieve zero steady state error to a step torque disturbance input.

$$err_{ss} = \lim_{s \rightarrow 0} s \left(\frac{Gg(s)}{1 - Gg(s)K_T G_{cl}(s)G_c(s)} \right) \frac{1}{s} \quad (5.2)$$

5.2.2 H_2 Optimization Controller. Again, it is pointed out that the final controller used for comparison and contrast with the current controller was obtained by placing the high frequency poles of the original H_2 design at lower frequency, as described in Section

4.4.3.2. The controller, repeated as Eqn. 5.3, is similar to the current controller in that it has high gain and leads to achieve the bandwidth necessary for speed of response and disturbance rejection. Although it does not contain a free integrator, it does have a "near" integrator that proved to yield more than adequate steady state error to a pure ramp and constant torque disturbance T_c input. Simulation indicated that the steady state error due to a pure ramp input was less than .05 μrad and was also less than .05 μrad due to T_c .

$$G_c(s) = \frac{-360 \times 10^6 (s + .013462)(s^2 + 29.4s + 441.1073)}{(s + .0001)(s + .99996)(s^2 + 424s + 90000)} \quad (5.3)$$

5.3 Simulations and Results

Simulations were performed with the torque disturbance input w_1 , the sensor noise input w_2 , step, ramp, and ephemeris command inputs as described in Section 4.3, and the non-linear bearing friction torque disturbance T_c . The inputs were simulated separately to determine the individual effects, and combinations of the inputs were simulated to determine the total system performance.

5.3.1 Torque Disturbance and Sensor Noise. The simulated torque disturbance driven by zero mean, unit intensity, white Gaussian noise, and shaped by W_d , had the time response shown in Figure 5-3. The position error due to the torque disturbance is shown in Figure 5-4. The current and H_2 systems had 2.12 and 0.47 μrad RMS of position error, respectively. The disturbance rejection transfer function with units of μrad per ft-lb is shown in Figure 5-5. It is clear that the H_2 controller had better disturbance rejection. However, as stated earlier the torque disturbance was modeled conservatively; therefore, the error due to torque disturbance may not be as severe in the actual SBD system.

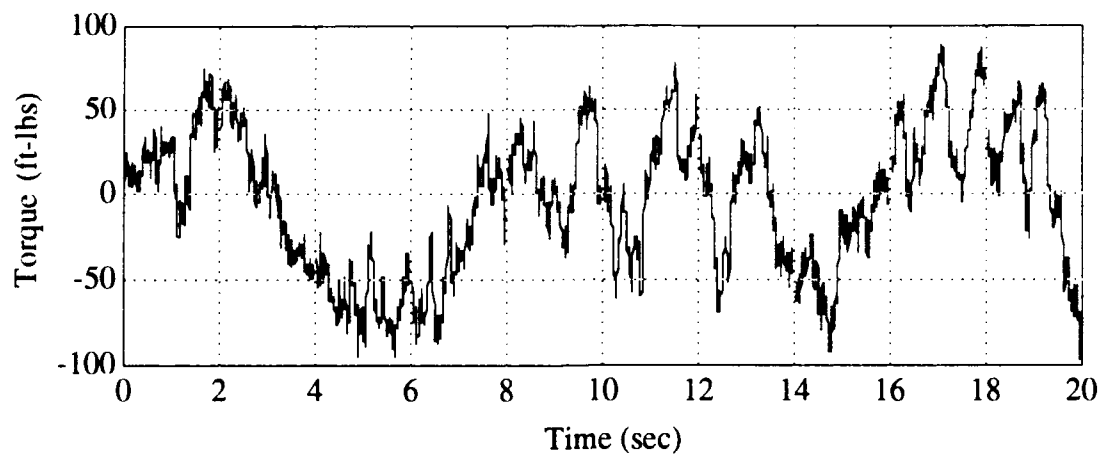


Figure 5-3 Torque Disturbance

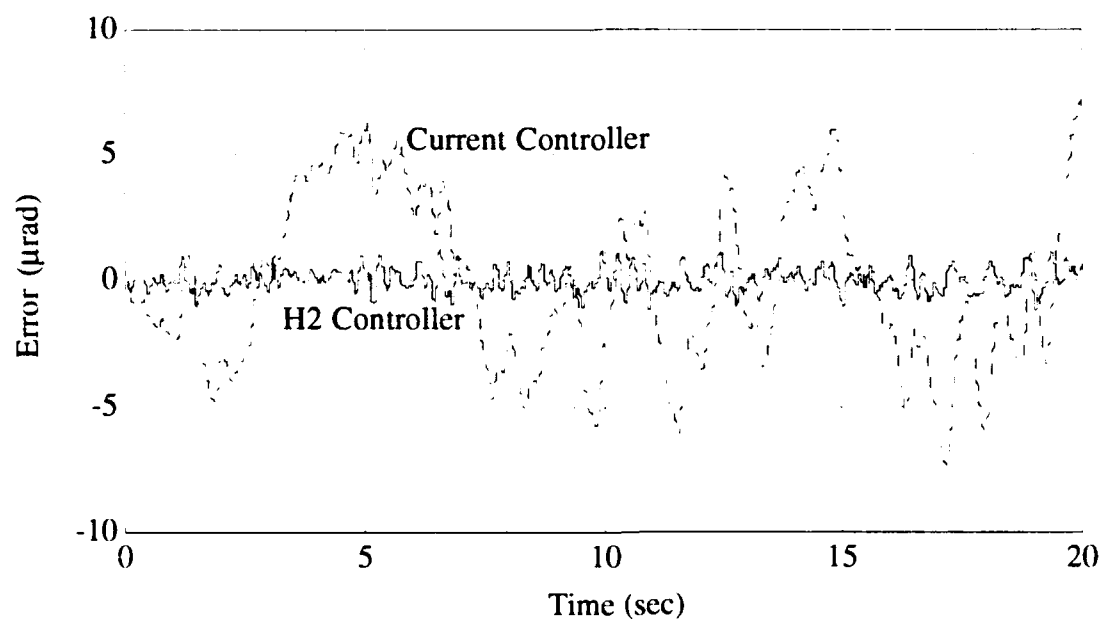


Figure 5-4 Position Error to Torque Disturbance

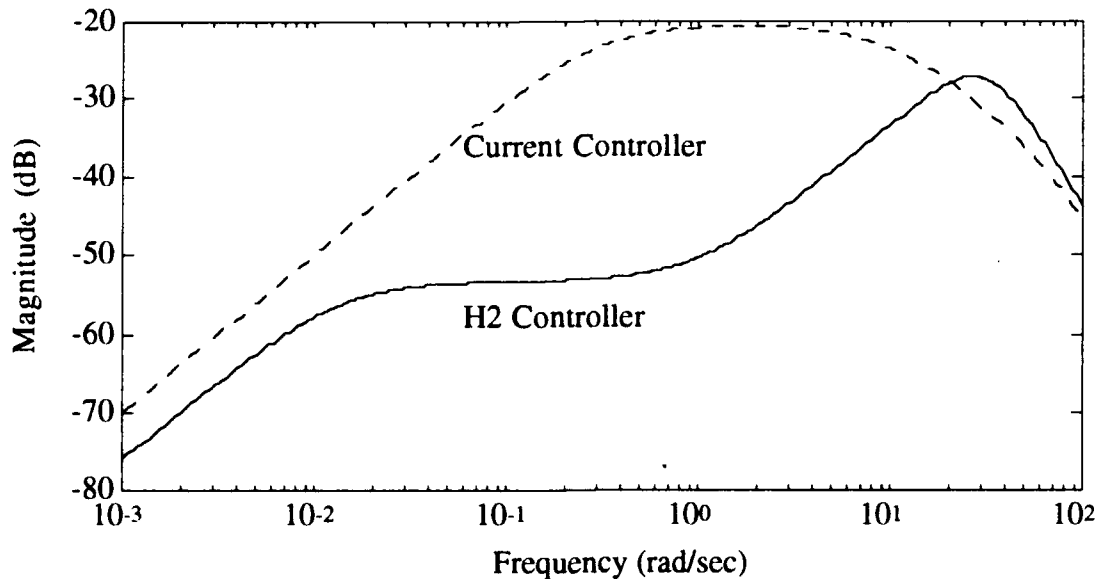


Figure 5-5 Torque Disturbance Rejection Transfer Function

Sensor noise was simulated with zero mean, unit intensity, white Gaussian noise, and filtered to prevent the unrealistic driving of high frequency control power. The position error due to sensor noise was approximately 0.3 μ rad RMS for both systems.

5.3.2 Step Response. Figure 5-6 shows the responses to a 100 μ rad step input, and Figure 5-7 is the closed-loop transfer function $\theta(s)/\theta_c(s)$ of the two systems. The H₂ system had a 2% settling time of approximately 300 msec. The current controller had a 2% settling time of 250 msec and was better damped with a damping ratio of 0.6 compared with 0.3 for the H₂ system. Although analysis of voltage saturation (± 10 volts) was not performed, both systems would have saturated with a 100 μ rad step. The current system required approximately 50% more control power than the H₂ system to achieve the well damped performance; therefore, had saturation been modeled, saturation for the current system would have been more severe. Greater saturation results in more overshoot and longer settling time [2:217-218]. Therefore, the well damped response does not necessarily mean that the current controller is a better design for step inputs.

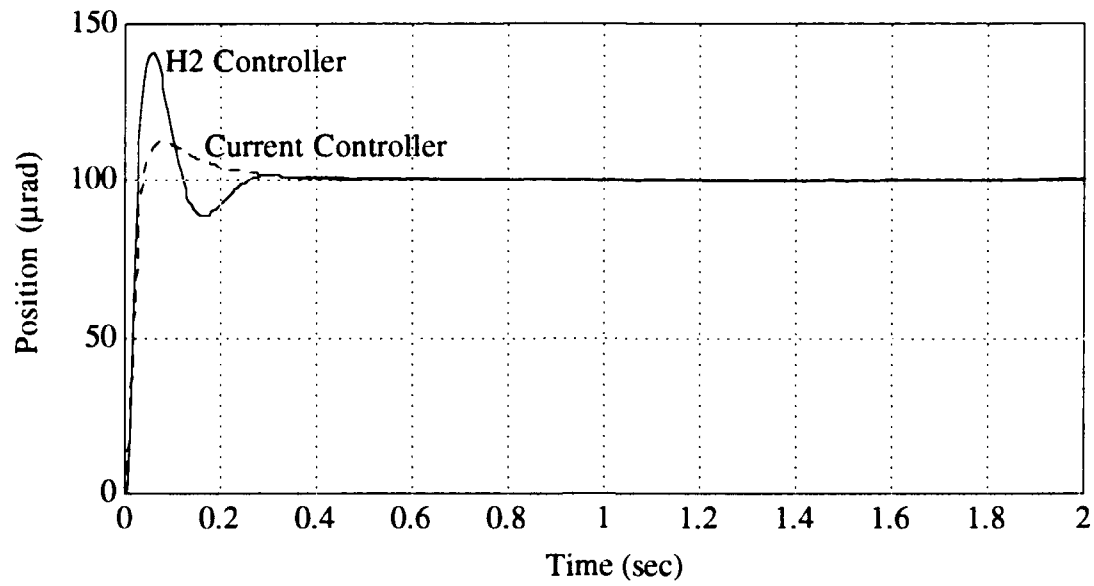


Figure 5-6 Step Response

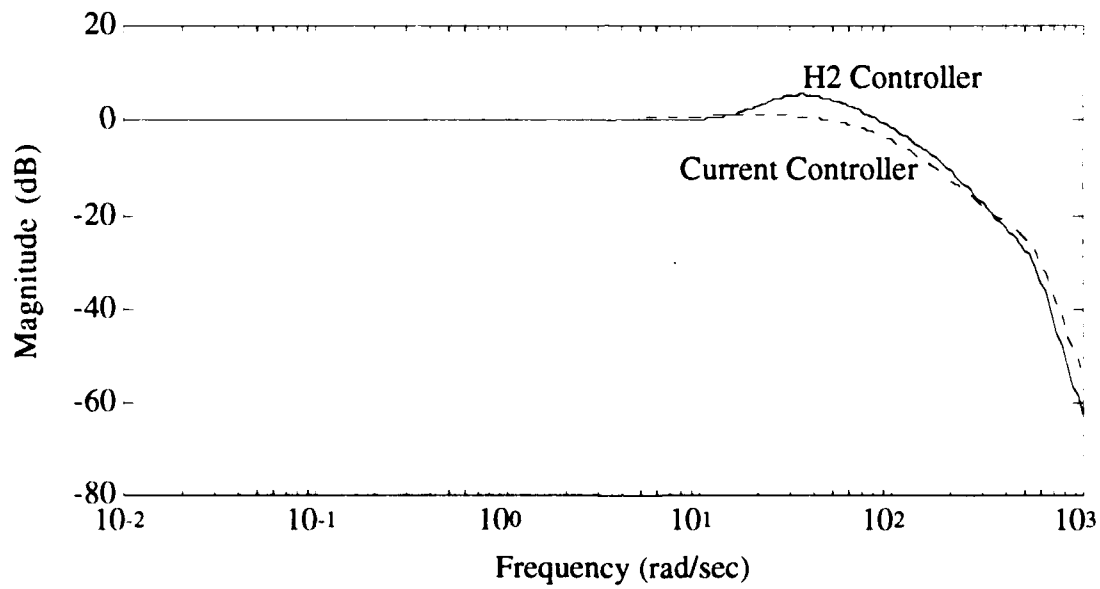


Figure 5-7 Closed-Loop Transfer Function

5.3.3 Ramp Response. As described in Section 1.4, bang-bang control is used to move the gimbal large distances. Thus, by the time control is switched to the fine position loop, the gimbal will have some initial velocity. To make the simulation more realistic an initial velocity condition is given. Actually, all the states, including the controller state, will have initial conditions, but experimenting with the initial conditions indicated that only the velocity initial condition was important. The first simulation presented was done without an initial condition for the purpose of contrasting a key difference between the two controllers. Figure 5-8 revealed that the amplitudes of the initial transients were about the same for both systems. In Figure 5-9 the initial transient response was removed by truncating the data to get a closer look at the steady state error. The H_2 controller produced near zero steady state error within 300 msec, while the current system had a settling time of greater than 10 seconds. This was the most significant difference between the two controllers.

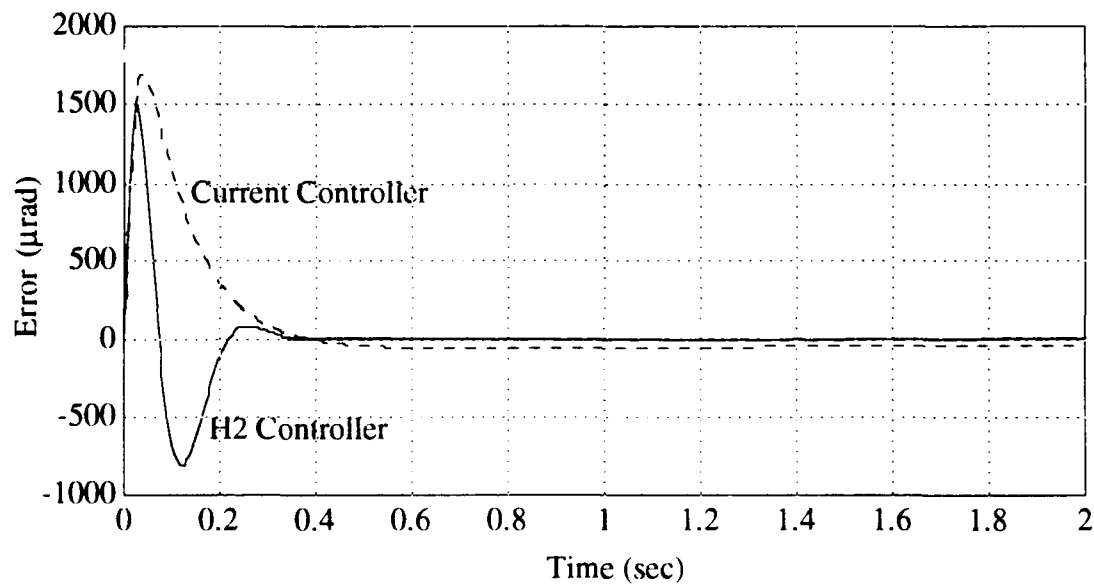


Figure 5-8 Ramp Command Tracking Error

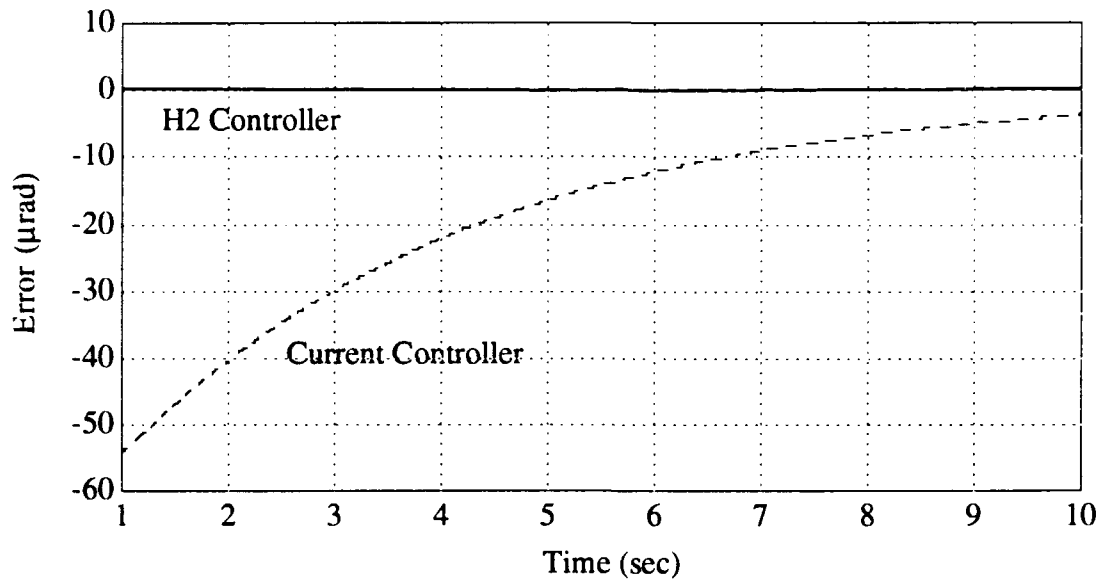


Figure 5-9 Truncated Ramp Command Tracking Error

The ramp command input has a slope of 0.1 rad/sec; therefore, the next simulation included an initial velocity of 0.1 rad/sec. The simulation also included the effects of the constant torque disturbance T_c . It would have been more realistic to pick an initial velocity less than 0.1 rad/sec, but to clearly illustrate the effects of bearing friction it was necessary to keep the initial transient to a minimum. Figure 5-10 and Figure 5-11 compare the effects of bearing friction of the current and H₂ controllers, respectively. Again, the large settling time with the current controller is seen. Both controllers did an adequate job rejecting the bearing friction torque disturbance. The small steady state error due to bearing friction with the H₂ controller can be seen in Figure 5-11 as the difference between the two curves.

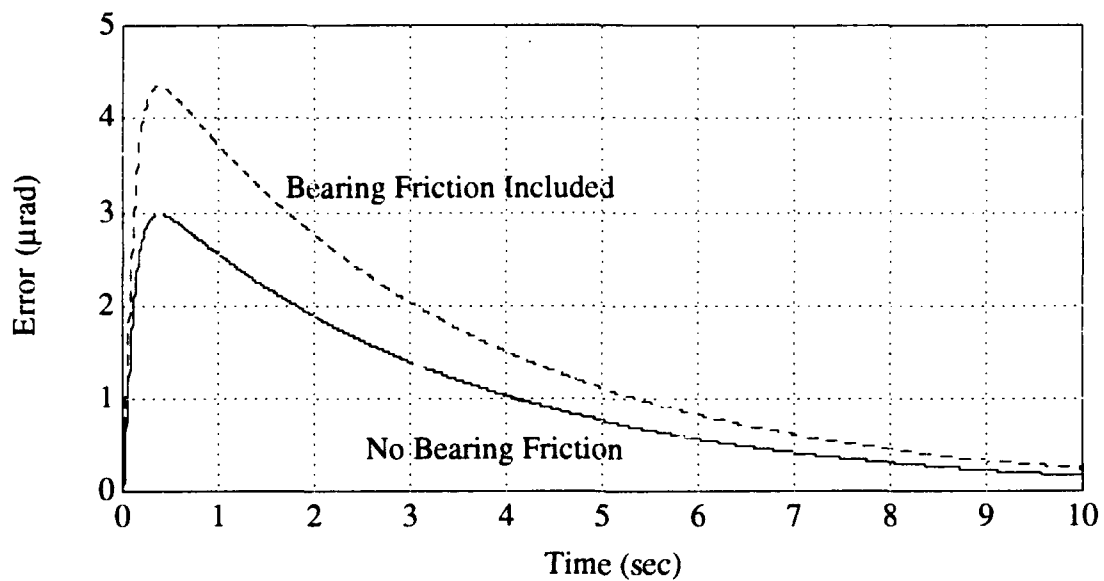


Figure 5-10 Bearing Friction Effect With Current Controller

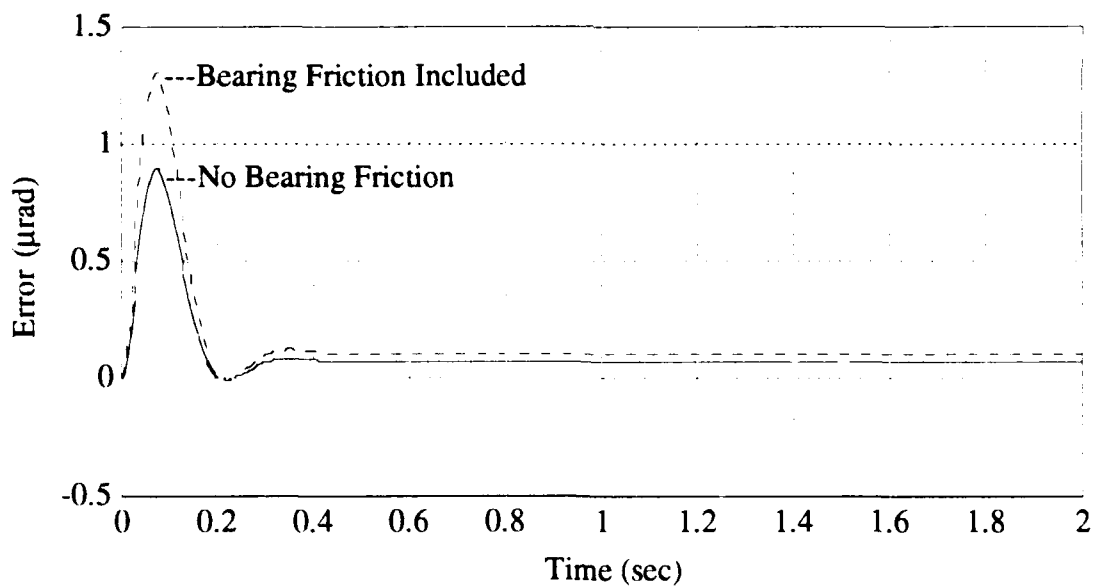


Figure 5-11 Bearing Friction Effect With H_2 Controller

5.3.4 Ephemeris Response. It is necessary at this time to make the distinction between RMS tracking error and steady state tracking error. Pointing and tracking requirements are usually split into two specifications: the first being pointing error defined as the bias or mean error, referred to in this thesis as the steady state error err_{ss} ; the second is the tracking jitter, which is the RMS error about the mean.

The simulation presented in this section only included the response to ephemeris command input. The velocity derived from the ephemeris command data had an initial value of 0.0875 rad/sec; therefore, an initial condition of .085 rad/sec was given to simulate the transient due to the hand-off from coarse to fine control. Figure 5-12 shows the resulting tracking error for both systems. The H_2 system had a settling time of 300 msec, err_{ss} of 0.36 μ rad, and an RMS tracking error of 1.0 μ rad. For the current system, it was not possible to determine the exact settling time or steady state error from the five second response, but as was seen with the ramp response in Section 5.3.3 the settling time was at least 10 seconds and the steady state error was asymptotically approaching zero. The RMS tracking error for the current system was 0.95 μ rad.

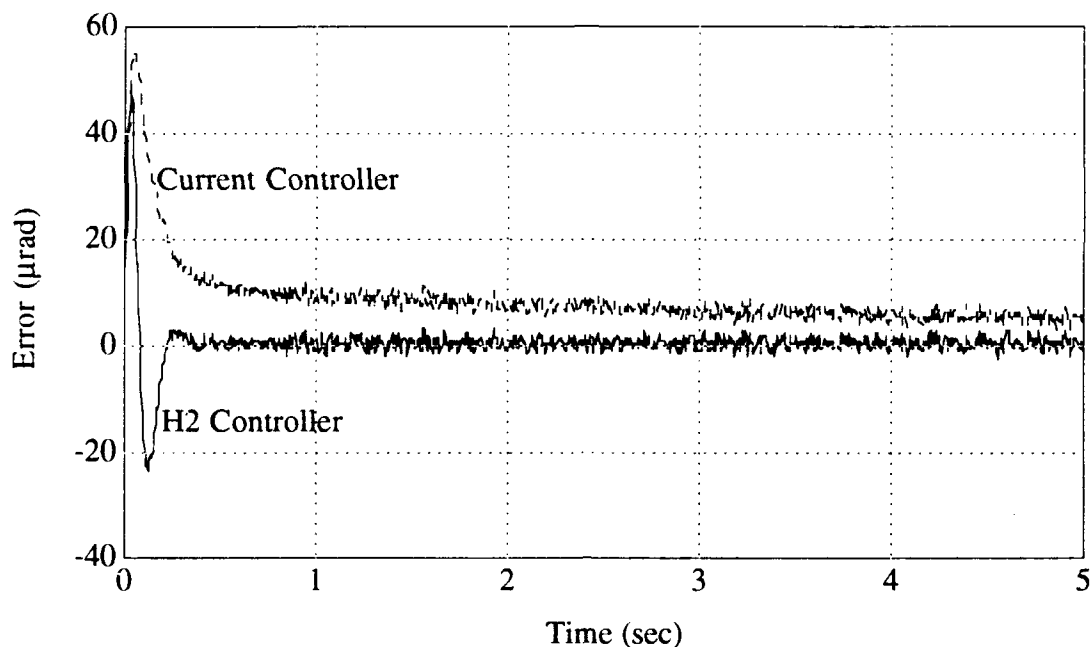


Figure 5-12 Ephemeris Command Tracking Error

5.3.5 Full-Up Simulation. Total system performance was analyzed in this section by simulating ephemeris command input with an initial velocity condition of 0.085 rad/sec, torque disturbance w_1 , sensor noise w_2 , and bearing friction torque disturbance T_c . Figure 5-13 shows the resulting tracking error for both systems. The conservatively modeled torque disturbance was apparent in the current system, whereas the torque disturbance was effectively rejected in the H_2 system. Time histories and PSD plots of all system signals for the full-up simulation are included in Appendix E.

The accuracy of the RMS tracking error values for the full-up simulation presented in the summary section in Table 5-2 is questionable. All of the RMS energy associated with the non-rejected low frequency torque disturbance was not captured in the 5 second sample of data. Therefore, the RMS values given were smaller than they would have been had the simulation been run longer. A five second sample of ephemeris data was the longest available. However, since the torque disturbance was modeled conservatively

this is not an important issue. Also, the point of the simulation was to compare the two controllers, and clearly the H_2 controller had the better disturbance rejection and ephemeris tracking performance.

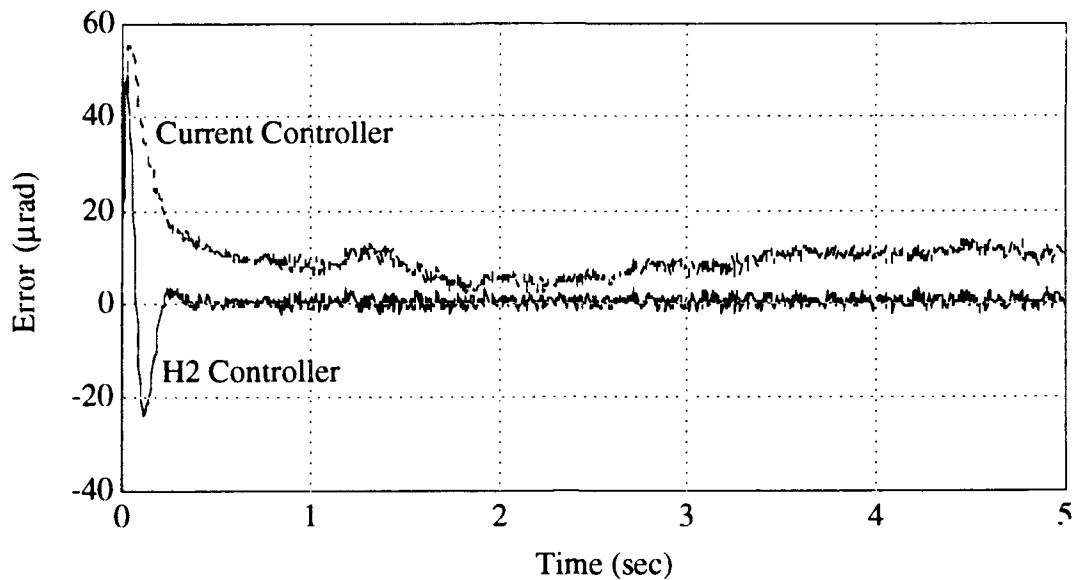


Figure 5-13 Full-Up Simulation Tracking Error

5.3.6 Summary of Results. Tables 5-1 and 5-2 are the compiled results from all simulations. Although the current system had a better step response, the H_2 controller proved to yield better overall performance, especially in the "true test of performance" of ephemeris tracking. One might think that the high price to pay for the better tracking performance would have been more control usage; however, as seen in the motor torque RMS values, the H_2 controller required only 10% more control power than the current controller.

Table 5-1 Simulation Results

Simulation	Settling Time	Over-shoot	RMS <i>err</i> (μ rad)	<i>err_{ss}</i> (μ rad)
Torque Disturbance				
Current Controller			2.12	
H ₂ Controller			0.47	
Sensor Noise				
Current Controller			0.30	
H ₂ Controller			0.30	
Bearing Friction				
Current Controller				≈ 0
H ₂ Controller				< 0.05
Step Response				
Current Controller	250 msec	10%		0.0
H ₂ Controller	300 msec	40%		0.0
Ramp Response				
Current Controller	≈ 10 sec			approaches 0
H ₂ Controller	300 msec			< 0.05
Ephemeris Response				
Current Controller	≈ 10 sec		0.95	approaches 0
H ₂ Controller	300 msec		1.0	0.36

Table 5-2 Full-Up Simulation Results

Full-Up Simulation	RMS <i>err</i>	<i>err_{ss}</i>	RMS	Mean Value
Current Controller	2.6 μ rad			
Voltage			0.66 volts	0.57 volts
Motor Torque			221 ft-lbs	195 ft-lbs
H ₂ Controller	1.14 μ rad	0.47 μ rad		
Voltage			0.60 volts	0.56 volts
Motor Torque			244 ft-lbs	190 ft-lbs

VI. Elevation Axis

6.1 Introduction

As stated earlier, the emphasis in this thesis is on controller design for the azimuth axis, and the elevation axis controller design is merely included for completeness. The data available for the elevation model is not complete; therefore, many assumptions are made in developing the model. Direct feedforward had to be implemented in the actual SBD elevation axis control to achieve adequate tracking for reasons not even the SBD engineers clearly understand. This indicates that there is something missing from the model developed in this thesis, because it is not necessary to implement feedforward to achieve the tracking requirements. Therefore, since the model does not accurately represent the actual system, a comparison between the currently used elevation axis controller and the controller developed in this chapter is not made. However, it is important to present the elevation axis model and controller design to provide a starting point for possible follow-on research.

6.2 Elevation Axis Linear Plant Model

Like the azimuth axis, the elevation axis consists of the current loop $G_{cl}(s)$, motor torque K_T , and the gimbal $Gg(s)$. Most of the model plant dynamics are obtained from the original coelostat documentation and from data taken from the actual SBD system. However, the data is not complete; therefore, some of the values for the model are estimated.

The motor torque constant and the gimbal's moment of inertia are given in the documentation as $K_T = 19.5$ ft-lbs/amp and $J = 1700$ ft-lbs-sec². No value for the

coefficient of viscous friction K_v is given, therefore, K_v is estimated such that the viscous damping is the same as it is in the azimuth axis. $K_v = 23$ ft-lbs/rad/sec.

The current loop dynamics are obtained from frequency response plots taken from the actual system. The plot was reconstructed in Matlab by iteration until the shape matched the original. Figure 6-1 shows that the current loop is a first order lag system with a break frequency ω_b of approximately 300 rad/sec and a gain constant K_a of 9 dB or 2.8 amps/volt.

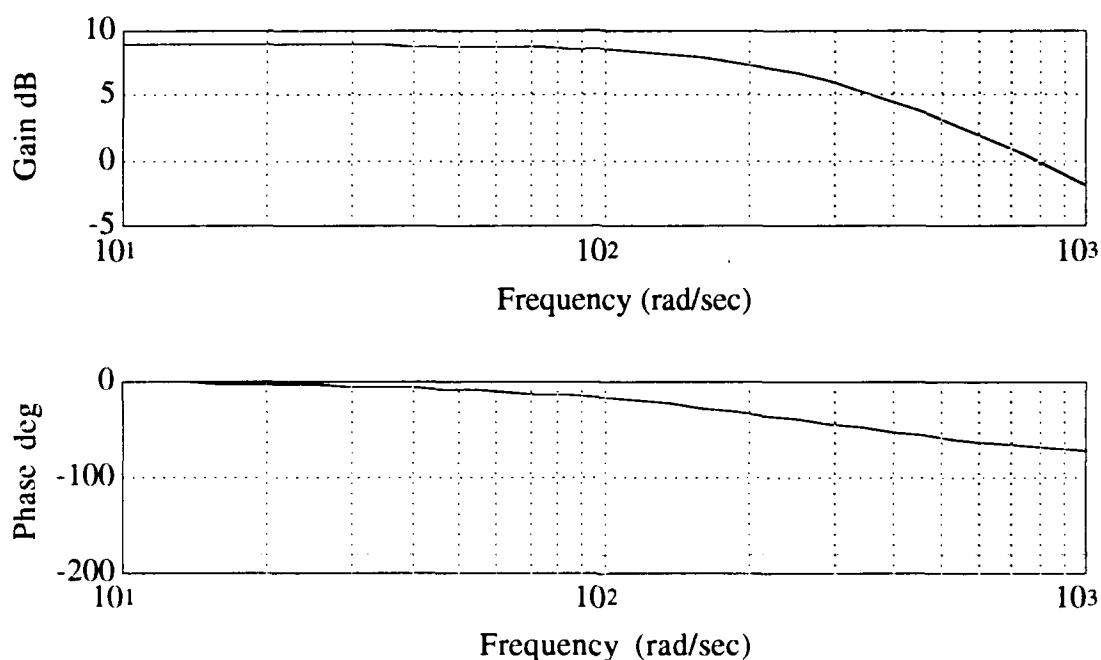


Figure 6-1 Elevation Axis Current Loop Frequency Response

6.3 Torque Disturbance and Sensor Noise

The motor cogging and ripple torque disturbances are estimated to be 10% of the magnitude of the disturbance used for the azimuth axis. Justification for the disturbance estimate came from data for a similar beam director that indicated that the magnitude of the elevation axis disturbance was 10% of that in the azimuth axis [7:14]. Wind buffeting

in the elevation axis will also not be as severe as in the azimuth axis. The torque disturbance is modeled as a coloring filter W_d , shown in Figure 6-2, driven by zero-mean, unit intensity, white Gaussian noise. W_d is described in state-space form as

$$\begin{aligned}\dot{x}_d(t) &= A_d x_d(t) + B_d w_1(t) \\ T_d(t) &= C_d x_d(t) + D_d w_1(t)\end{aligned}\tag{6.1}$$

where $T_d(t)$ is the torque disturbance, $x_d(t)$ is the disturbance state, and $w_1(t)$ is zero-mean, unit intensity, white Gaussian noise. The state-space values are

$$\begin{aligned}A_d &= -1 & B_d &= 1 \\ C_d &= 100 & D_d &= 0\end{aligned}\tag{6.2}$$

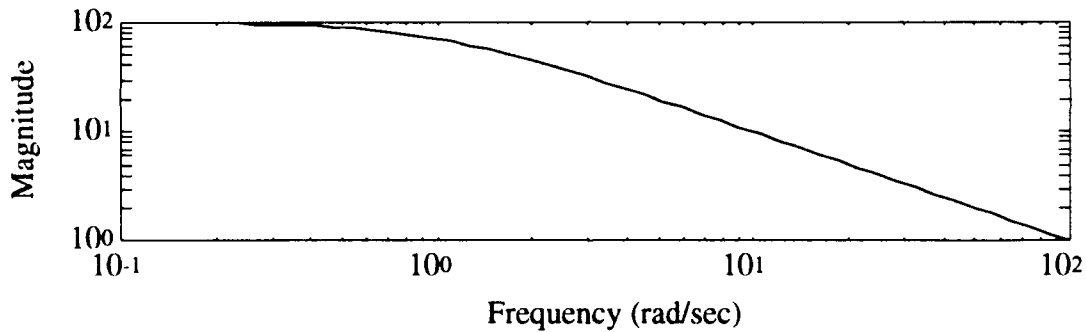


Figure 6-2 Torque Disturbance Coloring Filter

No data is available on the bearing friction; therefore, knowing that it will be less than the bearing friction in the azimuth axis, it is modeled as $T_c = 8$ ft-lbs.

The elevation gimbal position is measured using an Inductosyn encoder. The measurement of true angular position is corrupted by zero mean, white Gaussian noise with an RMS of .2 arc seconds or $1 \mu\text{rad}$ and is modeled as such for the controller design.

6.4 Nominal and Truth Models

The nominal model includes the current loop gain constant K_a , motor torque constant K_T , gimbal dynamics $Gg(s)$, torque disturbance input $T_d(t)$, and zero-mean, white Gaussian noise, of 1 μrad intensity sensor noise. The state-space representation of the nominal plant is

$$\begin{bmatrix} \dot{\theta}(t) \\ \ddot{\theta}(t) \end{bmatrix} = \begin{bmatrix} 0 & 1 \\ 0 & \frac{-K_v}{J} \end{bmatrix} \begin{bmatrix} \theta(t) \\ \dot{\theta}(t) \end{bmatrix} + \begin{bmatrix} 0 \\ \frac{1}{J} K_T K_a \end{bmatrix} v(t) \quad (6.3)$$

$$\theta(t) = [1 \quad 0] \begin{bmatrix} \theta(t) \\ \dot{\theta}(t) \end{bmatrix} + [0] v(t)$$

or

$$\begin{aligned} \dot{x}_p(t) &= A_p x_p(t) + B_p u_p(t) \\ y_p(t) &= C_p x_p(t) + D_p u_p(t) \end{aligned} \quad (6.4)$$

The truth or simulation model includes the nominal model plus the dynamics of the current loop $G_{cl}(t)$, non-linear bearing friction, first order Pade' approximation to a ZOH, and the sensor noise is rolled off at 40 dB per decade. The elevation axis parameter values are summarized in Table 6-1.

Table 6-1 Elevation Axis Parameters

Parameter		Value
Moment of Inertia (ft-lbs-sec ²)	J	17000
Coefficient of Viscous Friction (ft-lbs/rad/sec)	K_v	23
Motor Torque Constant (ft-lbs/amp)	K_T	19.5
Sample Period (sec)	T	0.005
Current Loop Gain Constant (amp/volt)	K_a	2.8
Current Break Frequency (rad/sec)	ω_b	300
Bearing Friction Torque Constant (ft-lbs)	T_c	8

6.5 Elevation Axis Controller Design

The same unity feedback setup used for the azimuth axis controller design is used for the elevation design. As in the azimuth axis design R_z is chosen to be 1 and H is a 2 by 2 identity matrix. The final sensitivity weighting W_s , chosen to achieve the performance requirements of disturbance rejection and command tracking, is shown in Figure 6-3 and its state-space representation is

$$\begin{aligned}\dot{x}_s(t) &= A_s x_s(t) + B_s \theta_m(t) \\ z_3 &= C_s x_s(t) + D_s \theta_m(t)\end{aligned}\tag{6.5}$$

where z_3 is the controller output, $x_s(t)$ is the sensitivity weighting state, and $\theta_m(t)$ is the measured gimbal position. The state-space values are

$$\begin{aligned}A_s &= -0.0001 & B_s &= 1 \\ C_s &= .5 & D_s &= 0\end{aligned}\tag{6.6}$$

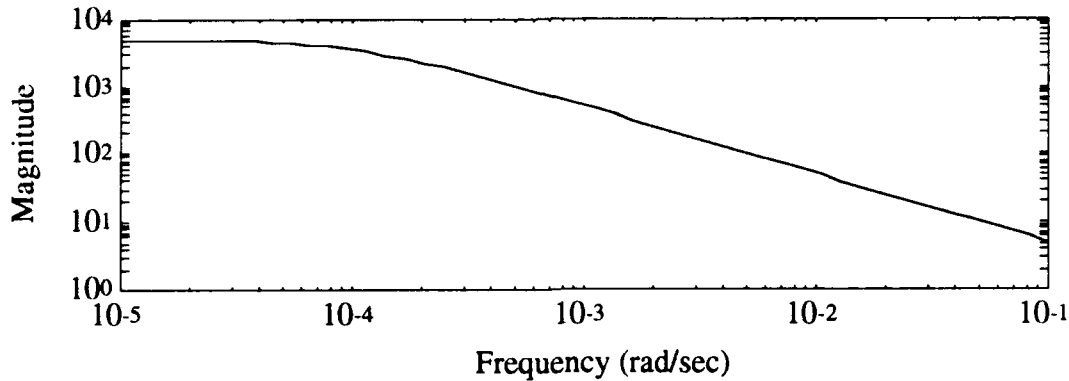


Figure 6-3 Sensitivity Weighting

The state-space description of the resulting controller is contained in Appendix A. The system had gain and phase margins of (-11.1 dB, 20 dB) and $\pm 43^\circ$, and a bandwidth of 49 rad/sec. Like the azimuth axis H_2 optimization put a pair of complex poles at high frequency resulting in more high frequency control power than was necessary for the required system performance. The high frequency poles could be moved to a lower frequency without decreasing system performance or decreasing the gain and phase margins below acceptable values.

6.6 Simulation and Results

Simulations were performed with the truth model. The disturbance rejection transfer function, shown in Figure 6-4, was not as good as it was in the azimuth axis. This is to be expected, because the moment of inertia of the azimuth axis is 15 times greater than that of the elevation axis, thus making it naturally more resistant to torque disturbances. Even though the input torque disturbance was modeled as 10% of that in the azimuth axis, the position error due to torque disturbance was greater in the elevation axis; $err = 0.78 \mu\text{rad RMS}$. However, the disturbance rejection was still more than adequate.

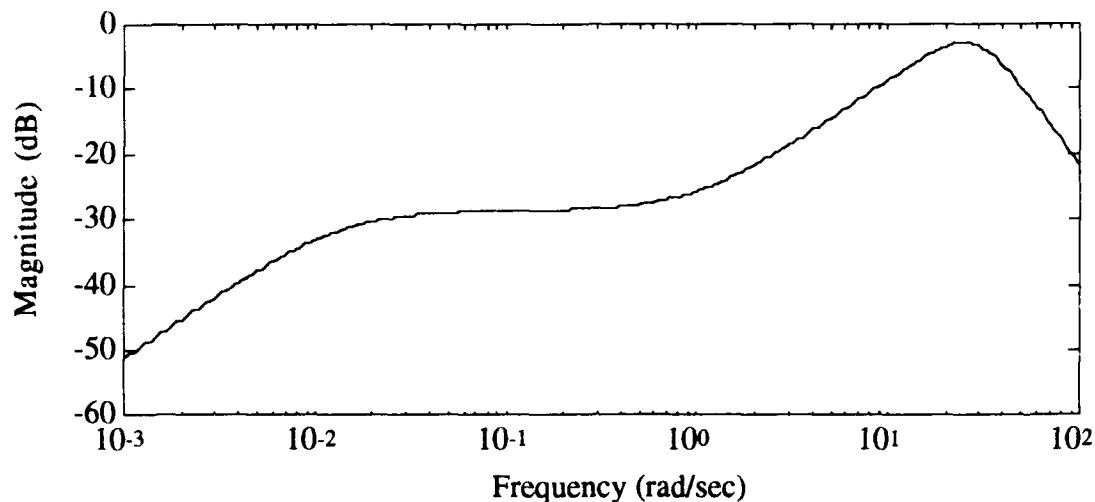


Figure 6-4 Torque Disturbance Rejection Transfer Function

In general, the elevation rate of a satellite ephemeris vector is considerably less than the azimuth rate for an elevation over azimuth beam director. The elevation position ephemeris had an average rate of 0.007 rad/sec compared to 0.1 rad/sec for the azimuth position ephemeris. Therefore, the tracking environment for the elevation axis is not as severe and is evident in the time response shown in Figure 6-5. Even with no initial velocity condition given, the initial transient was not too severe, the RMS jitter and err_{ss} were only 0.06 and 0.05 μ rad, respectively. The full-up simulation of ephemeris command input, torque disturbance, bearing friction disturbance, and sensor noise yielded RMS jitter and err_{ss} of 1.0 and 0.62 μ rad, respectively.

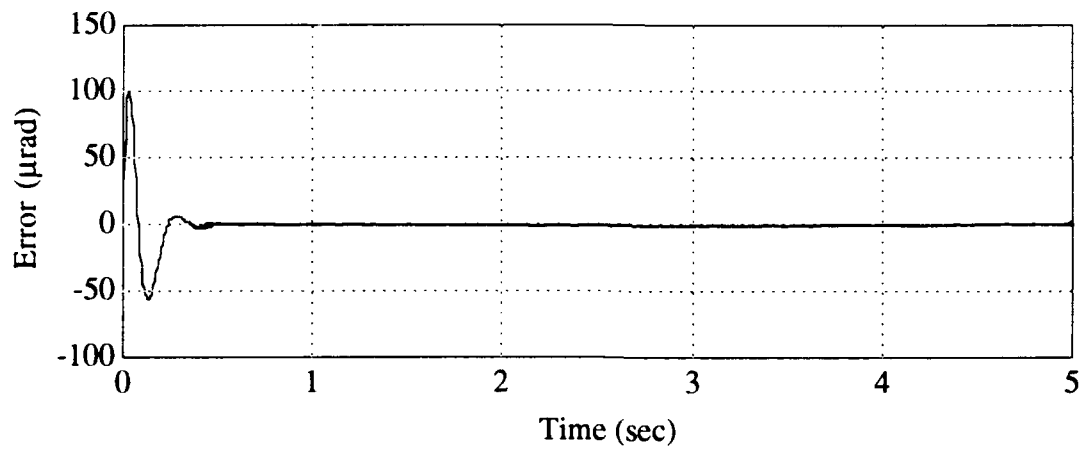


Figure 6-5 Ephemeris Command Tracking Error

VII. Conclusions/Recommendations

7.1 Conclusions

The two objectives of this thesis were met: a controller for the azimuth axis was designed that had better performance than the currently used controller, and optimal control was used to develop the controller.

The modeling (including the plant, disturbances, and sensor noise) and defining system requirements proved to be the most difficult tasks in designing the controller. Since the model was a SISO system, classical design techniques could have been used to design a controller with better ramp tracking performance than the currently used controller, because it appears that the original design was based on step response performance and not ramp tracking performance. The optimal control design techniques proved to be no more difficult than a classical approach, because once the optimal control problem was set up and it was understood how the control weightings affect system performance, it was relatively straightforward to "dial" the weightings to "tune" system performance.

7.1.1 Azimuth Axis Performance. The currently used controller yielded a system with better robustness than the H_2 controller. However, the gain and phase margins for the H_2 system were more than adequate.

The H_2 controller produced better disturbance rejection than the currently used controller. However, as stated in Section 5.3.1 the disturbance in the actual SBD system may not be as severe as the modeled disturbance; therefore, a controller with better disturbance rejection may not be necessary.

The currently used controller yielded a better damped, slightly faster, step response than the H_2 controller. However, this is not necessarily an advantage for three reasons: first, as described in section 5.3.2 the current controller requires more control power for step command following, and thus would have a larger saturation problem; second, the true test of performance is tracking ephemeris commands which are more akin to ramp commands than step commands; and third step commands are more realistically a job for the coarse position loop or "bang-bang" controller.

The most important difference between the two controllers was in their ability to track ramp or ephemeris commands. The settling time to achieve near zero steady state error for the H_2 system was 300 msec, while the settling time for the current system was greater than 10 seconds.

7.1.2 The Price to Pay. The most obvious difference between the two controllers is that the currently used controller is 2nd order and the H_2 controller is 4th order. Generally, optimal control produces high order controllers. However, if classical control design had been used to develop a controller with the same tracking performance as the H_2 controller, it is likely that it would have been higher than 2nd order.

The gimbal has resonant frequencies at 14, 30, and 45 Hz, or 88, 188, and 282 rad/sec, respectively. Notch filters were implemented on the current SBD system to account for the gimbal's natural modes. If the H_2 controller is implemented on the SBD, notch filters will also have to be used. As described in Section 4.4.2.2, the high frequency poles of the H_2 controller were moved to roll off the controller to minimize high frequency control use that would drive the resonant frequencies. As seen in the closed-loop transfer function $\theta(t)/\theta_d(t)$, Figure 7-1, the final H_2 controller still has more gain than the current controller out to 300 rad/sec. Placing the poles at an even lower frequency to roll off the compensator will have many adverse effects; lower bandwidth, lower gain and phase margins, and less damping. The notch filtering will be a more

difficult task with the H_2 controller for the resonant frequencies of 88 and 188 rad/sec, because the gain is higher than the current system at those frequencies.

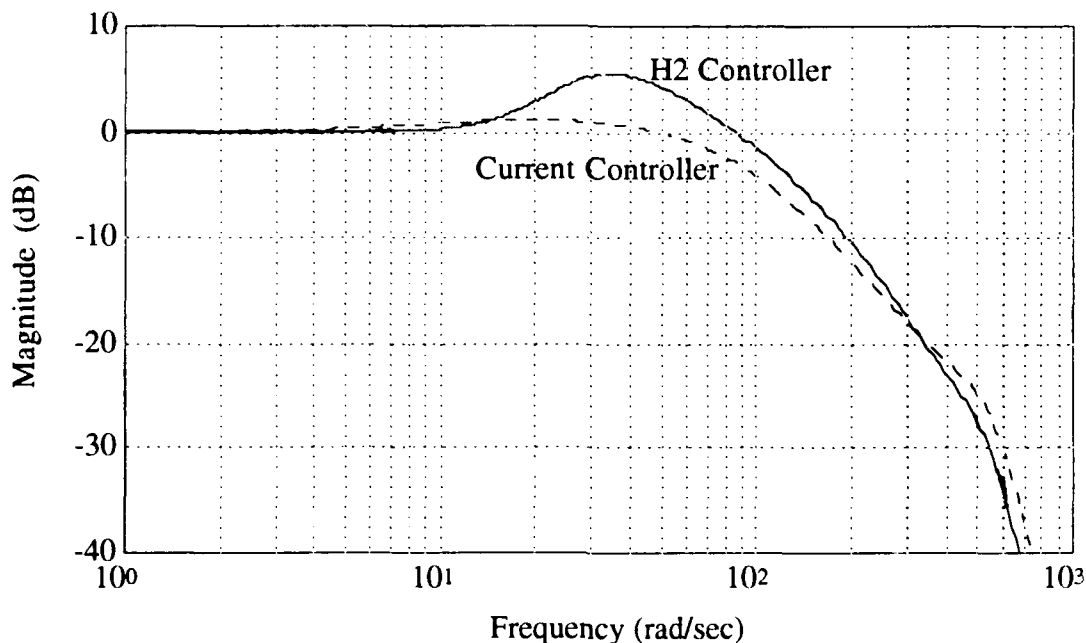


Figure 7-1 Closed-Loop Transfer Function

7.2 Future Research

Better understanding of the elevation axis dynamics and the coupling between the azimuth and elevation axes would enable one MIMO system model to be built. The two inputs would be azimuth and elevation position commands and the two outputs would be the measured azimuth and elevation positions. The resulting controller would be a coupled 2 by 2 matrix controller. The challenge would be to utilize the true advantage of optimal control design for a MIMO system and provide the SBL with a controller that addresses the coupling problem.

One of the original objectives of this thesis was to use both H_2 and H_∞ optimization for the controller design and compare and contrast the two. However, the scaling

problem described in Section 4.2 prevented completely successful H_∞ optimization results. An H_∞ synthesized controller was designed with marginal performance, and more effort would have eventually yielded an adequate controller. However, even if a successful H_∞ design was achieved, the comparison would have been difficult at best, because the scaled plant used for H_∞ optimization was drastically different than the scaled plant used for H_2 optimization. Further investigation is needed to determine the cause of the numerical problems H_∞ has with this model, and to determine the proper scaling necessary to develop a controller with good performance. It may have been possible to develop an adequate controller of the uncoupled SISO system, but a much better understanding of the H_∞ numerical problems will be necessary to develop a controller for a coupled MIMO system.

The most interesting suggested follow-on research is to design a two degree of freedom controller for the SBD model that has better performance than the unity feedback controller for ramp or ephemeris command tracking. A two degree of freedom controller has more flexibility than a unity feedback controller and theoretically, should provide at least as good if not better tracking performance. One of the two degree of freedom controllers designed in this thesis did yield a faster, better damped step response than the unity feedback controller. However, ramp tracking was non-existent and efforts to better the performance by changing the track weighting were less than completely successful. "Dialing" of the track weighting W_t was exhausted to achieve the desired performance of fast, well damped, zero steady state error ramp tracking, while maintaining the well damped step response. Other weightings in conjunction with the track weighting, such as a sensitivity weighting and a weighting on the command input, were also attempted to no avail. In order to get the two degree of freedom controller to yield adequate performance alternate approaches need to be investigated.

7.3 Closing Comments

This thesis demonstrates that optimal control design is a powerful tool that can be used not only to achieve robustness but also microradian tracking performance. The ultimate test of performance would be to integrate the discretized azimuth axis H_2 controller into the SBD. Obviously, that decision will be made by the SBD engineers who have to determine if the improved performance demonstrated in this thesis is worth the effort.

Appendix A: Final Compensator Design

A.1 Azimuth Axis Compensator

Transfer function form of negative feedback controller:

$$G_c(s) = \frac{360 \times 10^6 (s + 0.013462)(s^2 + 29.4s + 441.1073)}{(s + 0.0001)(s + 0.99996)(s^2 + 424s + 90000)}$$

State-space form:

$$G_c(s) = C_c(sI - A_c)^{-1}B_c + D_c$$

$$A_c = \begin{bmatrix} -425.0 & -90424.0 & -90006.0 & -8.9996 \\ 1.0 & 0 & 0 & 0 \\ 0 & 1.0 & 0 & 0 \\ 0 & 0 & 1.0 & 0 \end{bmatrix} \quad B_c = \begin{bmatrix} 1 \\ 0 \\ 0 \\ 0 \end{bmatrix}$$

$$C_c = [3.6 \times 10^8 \quad 9.6019 \times 10^9 \quad 1.2561 \times 10^{11} \quad 1.6892 \times 10^9] \quad D_c = 0$$

A.2 Elevation Axis Compensator

State-space form:

$$A_c = \begin{bmatrix} -14141.0 & 1.0 & 100.0 & 0 \\ -1273.0 & -50.458 & -4945.9 & -0.016059 \\ -999860.0 & 0 & -1.0 & 0 \\ 0 & 0 & 0 & -0.0001 \end{bmatrix} \quad B_c = \begin{bmatrix} 0.014141 \\ 0 \\ 0.99986 \\ 1.0 \end{bmatrix}$$

$$C_c = [39636.0 \quad 1570.6 \quad 153990.0 \quad 0.5] \quad D_c = 0$$

Appendix B: Matlab M-Files

B.1 Introduction

M-files were used extensively. Data, such as model parameter values were stored in M-files as opposed to data or MAT-files. It was easier to edit an M-file where a parameter and its value were clearly displayed. Simply typing the M-file name loaded its parameter contents into the Matlab work space. The comment sign "%" was also used extensively not only to add descriptive comments, but to comment out certain commands that were not wished to be executed for a particular analysis. Contained in this appendix is a list of all M-files and a short description used in the execution of this thesis, and a print out of some of the key M-files.

B.2 List of M-files

M-Files

- ave* - Calculates the average or mean value of a time history.
- azplant* - Contains all the azimuth axis plant parameter values, and builds state-space form of the nominal and truth models.
- cctoteval* - Creates linear state-space model of Simulink model "SimCCTotEvalMod" for the currently used controller to calculate the closed-loop transfer function and the disturbance rejection transfer function. Also calculates Bode frequency response and gain and phase margins of $G_p(s)G_c(s)$, where $G_p(s)$ is the truth model.
- cesca* - executes the sequence of M-files; *pbazsw15*, *H2*, *sentoteval*, which, builds the P matrix, calculates the H_2 optimal controller, and plots the Bode frequency plot of $-G_p(s)G_c(s)$.
- classcntr* - builds the currently used controller state-space, plots Bode frequency response, and calculates gain and phase margin from $G_p(s)G_c(s)$, where $G_p(s)$ is the truth model.
- comproll* - builds the final controller state-space.
- elplant* - Contains all the elevation axis plant parameter values, and builds the nominal and truth models.
- H2* - Calls the *h2opt* and *split* M-files to calculate the optimal controller and split it into its state-space form A_c , B_c , C_c , D_c .
- h2opt* - H_2 optimization algorithm
- Hin* - Calls the *hinf5* M-file to calculate the H_∞ optimized controller.

hinf5 - H_∞ optimization algorithm

param - Builds state-space of torque disturbance coloring filter, sensor noise shaping filter, and all weightings.

pbazsw1-14 - Builds azimuth axis P matrix for various unity feedback setups with 2nd and 3rd order sensitivity and complementary sensitivity weightings

pbazsw15 - Builds azimuth axis P matrix for the final unity feedback design with a 1st order W_s

pbaztw1-12 - Builds azimuth axis P matrix for various 2 degree of freedom controller setups with weightings W_t , W_s , and input weighting W_r .

pbaztw13 - Builds azimuth axis P matrix for 2 degree of freedom controller setup with 1st order W_t .

pbaztw14 - Builds azimuth axis P matrix for 2 degree of freedom controller setup with 2nd order W_t .

pbelsw2 - Builds elevation axis P matrix for the final elevation axis unity feedback design with a 1st order W_s

psd - Calculates RMS and Plots PSD of a vector.

scale3 - Performs internal scaling of the optimal control setup

sentoteval - Creates linear state-space model of Simulink model "SimSenTotEvalMod" for the unity feedback design to calculate the closed-loop transfer function and the disturbance rejection transfer function. Also calculates Bode frequency response and gain and phase margins of $-Gp(s)Gc(s)$. where $Gp(s)$ is the truth model.

split - Splits the H_2 optimal controller P_c into A_c , B_c , C_c , D_c .

trcktoteval - Creates linear state-space model of Simulink model "SimTrckTotEvalMod" for the 2 degree of freedom controller design to calculate the closed-loop transfer function and the disturbance rejection transfer function. Also calculates Bode frequency response and gain and phase margins of $-Gp(s)Gc(s)$. where $Gp(s)$ is the truth model.

truncate - truncates all of the time histories generated from a Simulink simulation to eliminate the initial transient response from a 5 second simulation.

truncate10sec - truncates all of the time histories generated from a Simulink simulation to eliminate the initial transient response from a 10 second simulation.

B.3 Azimuth Axis Plant "azplant"

This M-file contains all the azimuth axis parameter values, and builds the state-space nominal and truth models used in H_2 optimization and Simulink simulation.

M-File *azplant*:

```
% Azimuth axis symbol definitions and values

% Ka - current loop gain constant (AMP/VOLT)
% Wan - amplifier natural frequency (rad/sec)
% z - amplifier damping coefficient
% KT - motor Torque Constant (ft-lbs/AMP)
% J - gimbal moment of inertia (ft-lbs-sec^2)
% Kv - Coefficient of viscous friction (ft-lbs/rad/sec)
```

% T - Sample rate of digital controller

Ka=4.4;
Wan=560;
z=.25;
KT=75.6;
J=26000;
Kv=350;
T=.005;

%Aa - amplifier A matrix
%Ba - amplifier B matrix
%Ca - amplifier C matrix
%Da - amplifier D matrix
%

Aa=[0 1;-Wan^2 -2*z*Wan];
Ba=[0;Ka*Wan^2];
Ca=[1 0];
Da= [0];

%Ag - gimbal A matrix
%Bg - gimbal B matrix
%Cg - gimbal C matrix
%Dg - gimbal D matrix
%

Ag=[0 1;0 -Kv/J];
Bg=[0;1/J];
Cg=[1e6 0];
Dg=0;

%Asd - Sampling Delay A matrix
%Bsd - Sampling Delay B matrix
%Csd - Sampling Delay C matrix
%Dsd - Sampling Delay D matrix
%

Asd=-2/T;
Bsd=2/T;
Csd=1;
Dsd=0;

% The following augmented plant state-space is for the
% optimization routines and therefore does not include the current
% loop dynamics. The current loop is modeled by the gain constant Ka.

%Ap - plant A matrix
%Bp - plant B matrix
%Cp - plant C matrix
%Dp - plant D matrix
%

```

Ap=Ag;
Bp=KT*Ka*Bg;
Cp=Cg;
Dp=0;

% The following state-space is the full plant "truth model" including current loop
% and sampling delay dynamics
Afp=[Asd zeros(1,4);Ba*Csd Aa zeros(2,2);zeros(2,1) Bg*KT*Ca Ag];
Bfp=[Bsd;0;0;0;0];
Cfp=[0 0 0 Cg];
Dfp=0;

```

B.4 Elevation Axis Plant "elplant"

This M-file contains all the elevation axis parameter values, and builds the state-space nominal and truth models used in H₂ optimization and simulation.

M-File *elplant*:

```

% Elevation axis symbol definitions values and model
% Ka - amplifier gain constant (AMP/VOLT)
% Wab - amplifier break frequency (rad/sec)
% KT - motor Torque Constant (ft-lbs/AMP)
% J - gimbal moment of inertia (ft-lbs-sec^2)
% Kv - Coefficient of viscous friction (ft-lbs/rad/sec)
% T - Sample rate of digital controller
Ka=2.8;
Wab=300;
KT=19.5;
J=1700;
Kv=23;
T=.005;

% Aa - amplifier A matrix
% Ba - amplifier B matrix
% Ca - amplifier C matrix
% Da - amplifier D matrix
%
Aa=[-Wab];
Ba=[Ka*Wab];
Ca=[1];
Da= 0;

% Ag - gimbal A matrix
% Bg - gimbal B matrix
% Cg - gimbal C matrix
% Dg - gimbal D matrix
%

```

```

Ag=[0 1;0 -Kv/J];
Bg=[0;1/J];
Cg=[1e6 0];
Dg=0;

%Asd - Sampling Delay A matrix
%Bsd - Sampling Delay B matrix
%Csd - Sampling Delay C matrix
%Dsd - Sampling Delay D matrix
%
Asd=-2/T;
Bsd=2/T;
Csd=1;
Dsd=0;

% The following augmented plant state-space is for the
% optimization routines and therefore does not include the amplifier
% dynamics. The amplifier is modeled by the gain constant Ka.
%Ap - plant A matrix
%Bp - plant B matrix
%Cp - plant C matrix
%Dp - plant D matrix

Ap=Ag;
Bp=KT*Ka*Bg;
Cp=Cg;
Dp=0;

% The following state-space is the full plant including amplifier
% and sampling delay dynamics

Afp=[Asd zeros(1,3);Ba*Csd Aa zeros(1,2);zeros(2,1) Bg*KT*Ca Ag];
Bfp=[Bsd;0;0;0];
Cfp=[0 0 Cg];
Dfp=0;

```

B.5 Weighting, Disturbance, and Noise Parameters "param"

This M-file builds the state-space representation of the torque disturbance coloring filter, the sensor noise shaping filter, and the dynamic weightings used in the various optimal control designs. This print out has been edited to remove all but the 1st order weighting W_s used in the final azimuth axis unity feedback design.

M-File *param*:

% param - Parameters for disturbance, noise, and weightings.


```

% Torque Disturbance distribution vector
gam=[1;0];

% Disturbance state-space where:
%           -1
%  $Wd(s) = Cd(sI - Ad) Bd + Dd$ 
% Disturbance parameters used in optimal control for performance robustness
Gain=1000;
wb=1;
numd=Gain*wb;
dend=[1 wb];
[Ad,Bd,Cd,Dd]=tf2ss(numd,dend);
% Disturbance parameters used in simulation
Gain=1000;
wb=1;
numd=Gain*wb;
dend=[1 wb];
[Adsim,Bdsim,Cdsim,Ddsim]=tf2ss(numd,dend);

% Sensor Noise parameters used in simulation
Gain=1;
wb1=50;
wb2=50;
numn=Gain*wb1*wb2;
denn=conv([1 wb1],[1 wb2]);
[Ansim,Bnsim,Cnsim,Dnsim]=tf2ss(numn,denn);

% Sensitivity weighting state-space where  $W_s$  is First Order
Gain=5000;
wb1=.0001;
numws=Gain*wb1;
denws=[1 wb1];
[As,Bs,Cs,Ds]=tf2ss(numws,denws);

% LQG weightings
Rz=1;
H=[1 0 ; 0 1];

```

B.6 Building the P matrix "pbazsw15"

This M-file calls the M-files *azplant* and *param* to build the state-space form of the azimuth axis model, the torque disturbance and sensor noise coloring filters, and the

weightings. Then it builds the P matrix and defines the dimension of P necessary for the H_2 optimization algorithm.

M-File pbazsw15:

% pbazsw15- Azimuth Axis P Matrix Build

% Unity feedback setup

% Build state-space azimuth axis plant
azplant

% Disturbance, noise, and weighting parameters
param

% Nine matrices that make up the state-space of $P(s)$

$A=[A_p \text{ gam} * C_d \text{ zeros}(2,1); \text{zeros}(1,2) \text{ Ad } 0; B_s * C_p \text{ } 0 \text{ } A_s];$

$B_w=[\text{zeros}(2,2); B_d \text{ } 0 \text{ } 0 \text{ } B_s];$

$B_u=[B_p; 0 \text{ } 0];$

$C_z=[H \text{ zeros}(2,2) \text{ } \text{zeros}(1,4); \text{zeros}(1,3) \text{ } C_s];$

$D_{zw}=[\text{zeros}(4,2)];$

$D_{zu}=[\text{zeros}(2,1); R_z; 0];$

$C_y=[C_p \text{ } 0 \text{ } 0];$

$D_{yw}=[0 \text{ } 1 \text{ }];$

$D_{yu}=[0];$

%

$P=[A, B_w, B_u; C_z, D_{zw}, D_{zu}; C_y, D_{yw}, D_{yu}];$

%

% Define the dimensions of P where

% $\text{dims}=[n_s, n_w, n_u, n_z, n_y]$

% n_s - number of states

% n_w - number of inputs w

% n_u - number of inputs u

% n_z - number of outputs z

% n_y - number of outputs y

$[m, n]=\text{size}(A);$

$n_s=m;$

$[m, n]=\text{size}(B_w);$

$n_w=n;$

$[m, n]=\text{size}(B_u);$

$n_u=n;$

$[m, n]=\text{size}(C_z);$

$n_z=m;$

$[m, n]=\text{size}(C_y);$

$n_y=m;$

$\text{dims}=[n_s, n_w, n_u, n_z, n_y];$

B.7 H₂ Optimization''H2''

This M-file calls the M-files *h2opt* and *split* to calculate the H₂ optimal controller and split the controller into its state-space form.

M-File H2

```
% H2- H2 Optimization
[Pc,su,sy,Kc,Kf]=h2opt(P,dims);
ns=dims(:,1);
[Ac,Bc,Cc,Dc]=split(Pc,ns);
```

B.8 H₂ Optimization''h2opt''

This M-file calculates the H₂ optimal controller.

M-File h2opt

```
function [pk,su,sy,kc,kf] = h2opt(p,dims)
%[pk,su,sy,kc,kf]=h2opt(p,dims)
ns = dims(1);nw = dims(2);nu = dims(3);nz = dims(4);ny = dims(5);
[a,b,c,d] = split(p,ns);
[d11,d12,d21,d22] = split(d,nz,nw);
if any(any(d11 ~= 0)), error('d11 not a zero matrix');end;
if any(any(d22 ~= 0)), error('d22 not a zero matrix');end;
[pscl,su,sy] = scale3(p,dims);
[a,b,c,d] = split(pscl,ns);
[d11,d12,d21,d22] = split(d,nz,nw);
b1 = b(:,1:nw);
b2 = b(:,nw+1:nw+nu);
c1 = c(1:nz,:);
c2 = c(nz+1:nz+ny,:);
f = a - b2*d12'*c1;
g = b2*b2';
c1hat = (eye(nz) - d12*d12')*c1;
h = c1hat*c1hat';
x2 = are(f,g,h);
f = (a - b1*d21'*c2)';
g = c2'*c2;
b1hat = b1*(eye(nw) - d21'*d21);
h = b1hat*b1hat';
y2 = are(f,g,h);
kc = b2'*x2 + d12'*c1;
kf = y2*c2' + b1*d21';
ak = a - kf*c2 - b2*kc;
bk = kf*sy;
ck = -inv(su)*kc;
dk = 0*ones(nu,ny);
```

pk = [ak, bk;ck, dk];

B.9 Frequency Responses "sentoteval"

This M-file calculates the open loop Bode frequency response and gain and phase margins of $-G_p(s)G_c(s)$. It also calculates the closed-loop transfer function $\theta(s)/\theta_d(s)$ and the torque disturbance rejection transfer function by calculating the closed-loop linear model of the Simulink model "SimSenTotEvalMod".

M-File *sentoteval*

% sentotaleval - Total Evaluation Model

% Gain and Phase Margins

% Closed-Loop and Torque Disturbance Rejection Transfer Functions

% Frequency range for all analysis

w=logspace(-2,3,300);

% Calculate the SISO gain and phase margins

% where Aol, Bol, Col, & Dol is the open loop state-space of $-G_p(s)G_c(s)$

[Aol,Bol,Col,Dol]=series(Ac,Bc,Cc,Dc,Afp,Bfp,Cfp,Dfp);

% Since feedback is positive the margins are obtained from $-G_cG_p$

[magol,phaol]=bode(Aol,Bol,-Col,Dol,1,w);

[GM,PM,wg,wp]=margin(magol,phaol,w);

margin(magol,phaol,w)

% Set up for transfer function calculations, null out filters

% and calculate linear model

Ansim=[];

Bnsim=[];

Cnsim=[];

Dnsim=1;

Adsim=[];

Bdsim=[];

Cdsim=[];

Ddsim=1;

[Acl,Bcl,Ccl,Dcl]=linmod('SimSenTotEvalMod');

% Torque disturbance rejection transfer function

[magds,phads]=bode(Acl,Bcl,Ccl,Dcl,1,w);

magds=20*log10(magds);

% Closed-loop transfer function

% Complimentary Sensitivity

[magns,phans]=bode(Acl,Bcl,Ccl,Dcl,2,w);

magns=20*log10(magns);

Appendix C: Simulab Block Diagrams

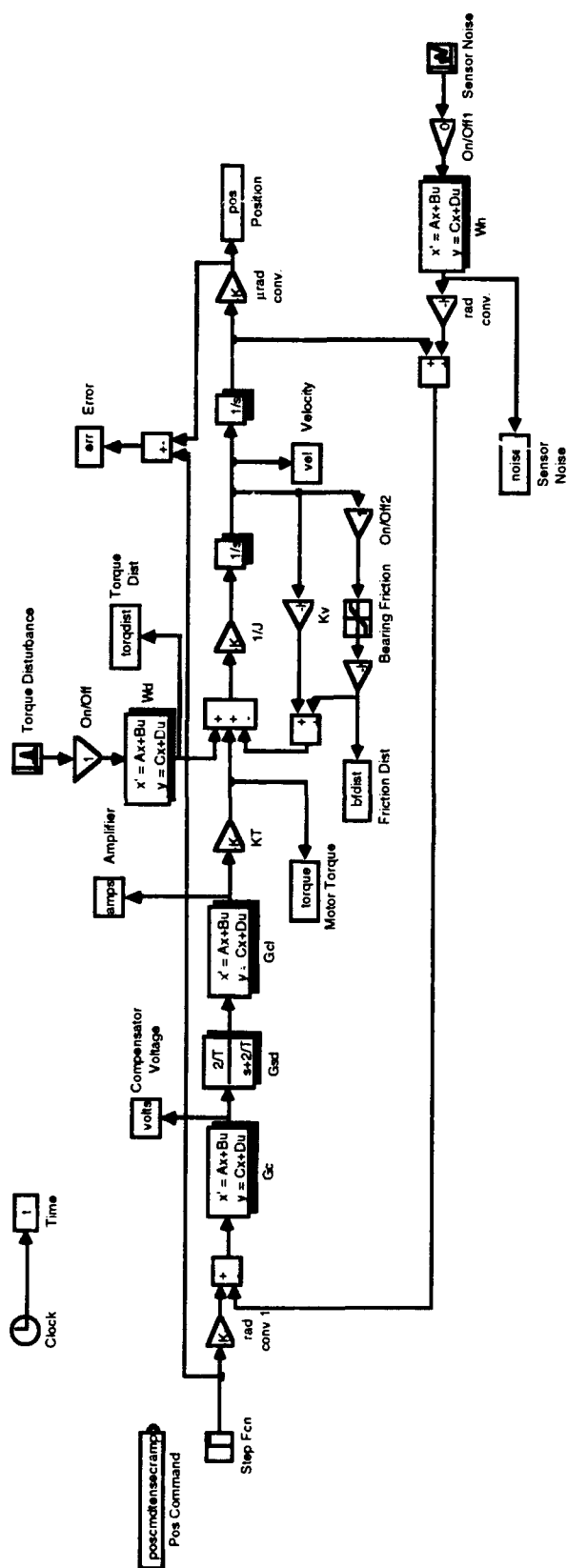


Figure C-1 Current Controller Simulation Model "SimCCEvalMod"

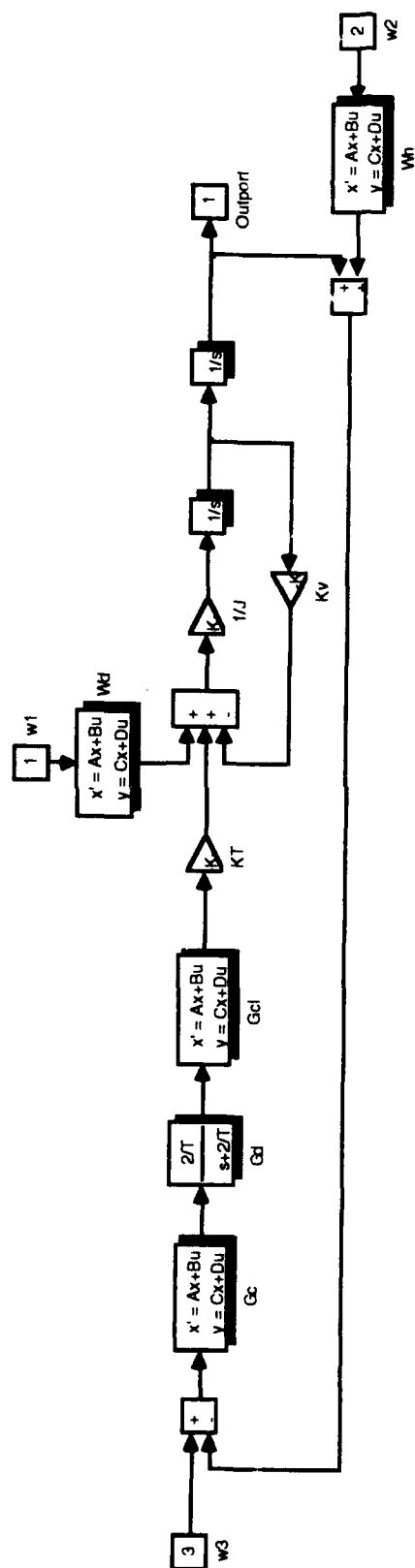


Figure C-2 Current Controller Linmod Model "SimCCTotEvalMod"

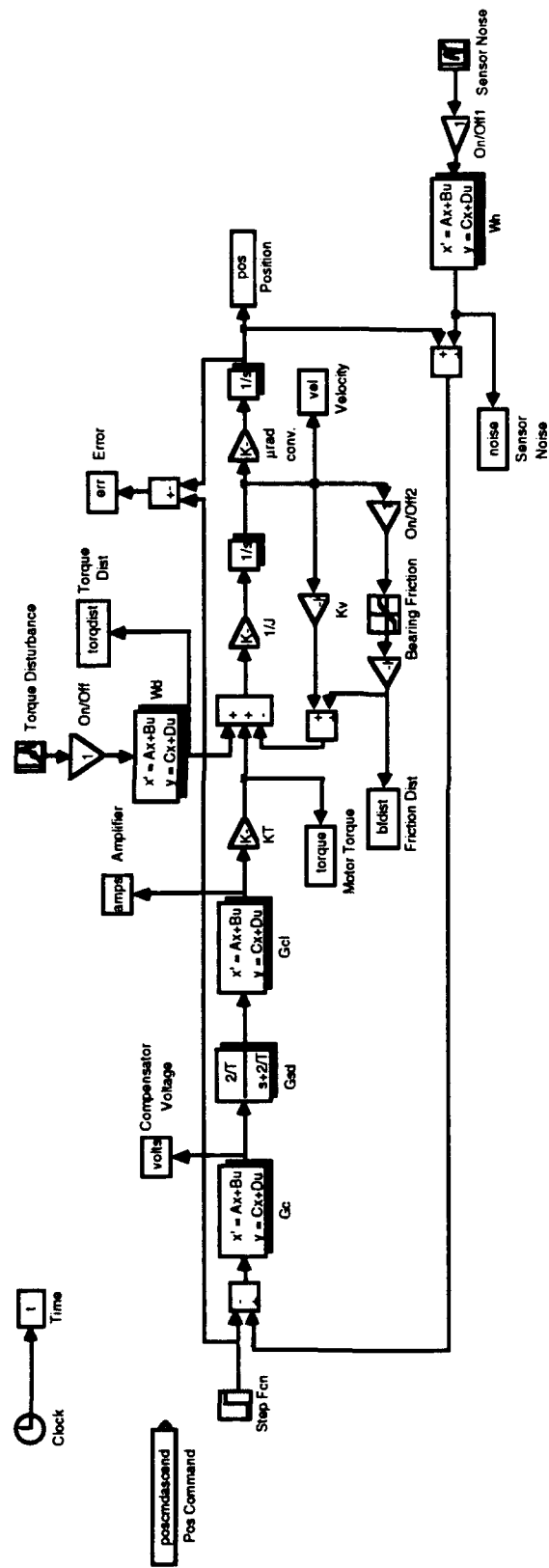


Figure C-3 Unity Feedback Simulation Model "SimSenEvalMod"

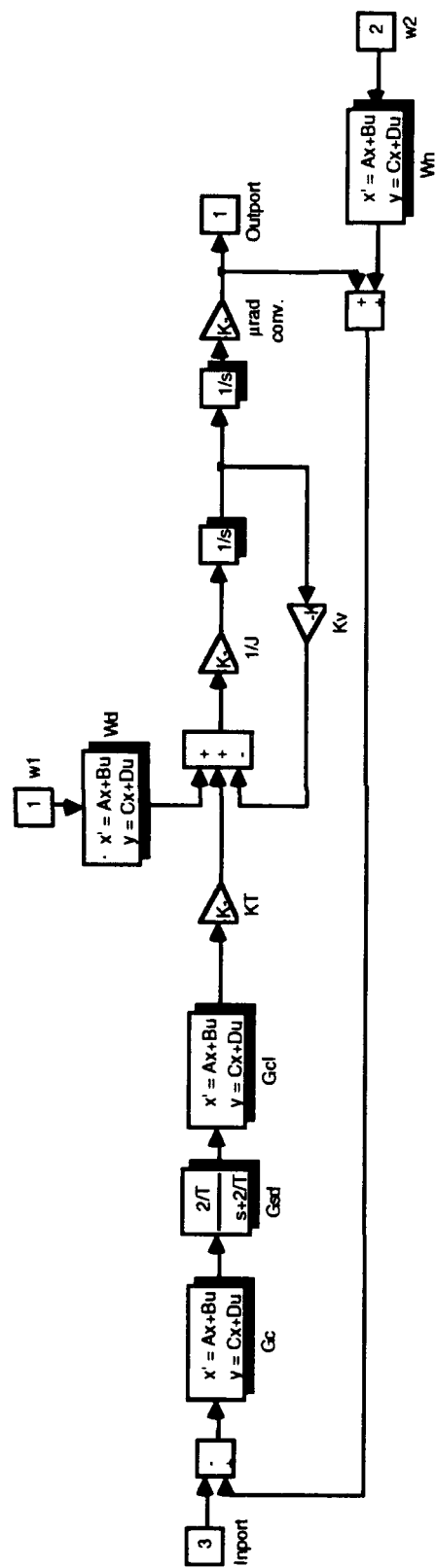


Figure C-4 Unity Feedback Linmod Model "SimSenTotEvalMod1"



Figure C-5 2 Degree of Freedom Controller Simulation Model "SimTrckEvalMod"

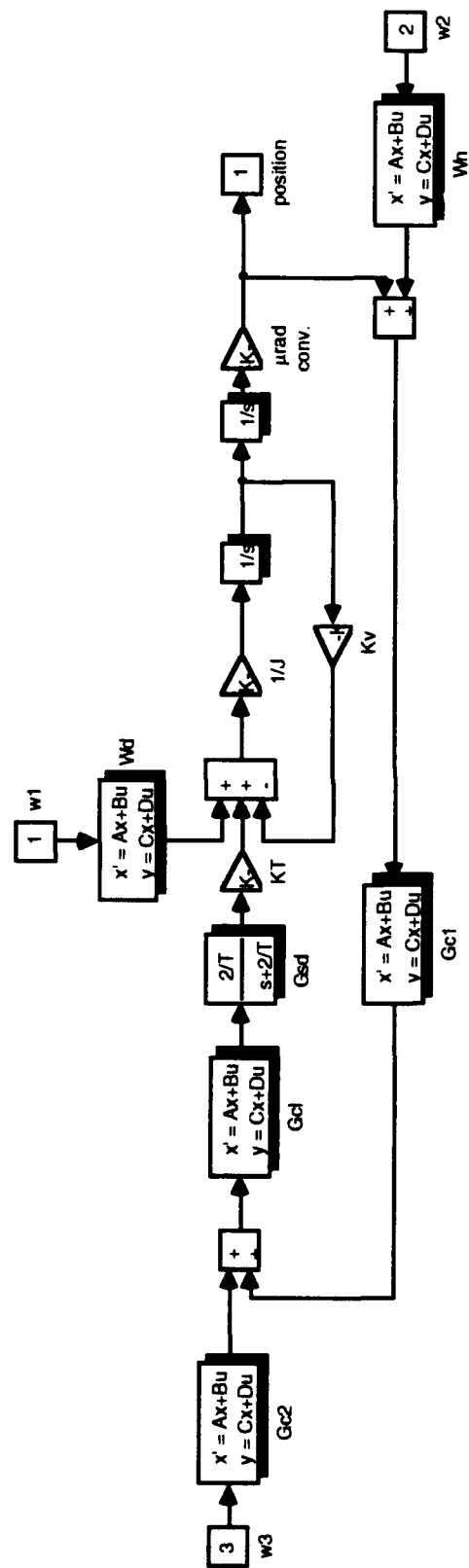


Figure C-6 2-Degree of Freedom Controller Linmod Model "SimTrckTotEvalMod"

Appendix D: SBD Controller Design and Simulation Tutorial

The following is the sequence of steps taken to design the azimuth axis H_2 optimal unity feedback controller and perform Simulink simulations.

1. Build the azimuth axis nominal and truth state-space models by typing *azplant* in the Matlab workspace.
2. Build the torque disturbance and sensor noise coloring filters, and weightings in state-space form by typing *param*.
3. Build the P matrix by typing *pbazsw15*.
4. Calculate the H_2 optimal controller in state-space format by typing *H2*.
5. Calculate the Bode frequency response and gain and phase margins of $-G_p(s)G_c(s)$, the closed-loop transfer function $\theta(s)/\theta_c(s)$, and the torque disturbance rejection transfer function by typing *sentoteval*.
6. Perform simulations with the Simulink model "SimSenEvalMod". The Simulink model was built mostly with state-space blocks such that the parameters for those blocks are automatically read in from the Matlab workspace.
 - a. Simulations were performed with the maximum and minimum step sizes set at 0.005 sec to correspond to the 200 Hz sample rate of the SBD. The integration algorithm used was Linsim.
 - b. Ramp and Ephemeris command tracking simulations were performed by using the "From Workspace" block to load in the command vector. The data for all the command vectors are stored in the MAT-file *poscmd*. The 5 and 10 second ramp command vectors are called *poscmdfivsecramp* and *poscmdtensecramp*, respectively. The 5 second ephemeris command vector is called *poscmdascend*.

Appendix E: Full-Up Simulation Plots

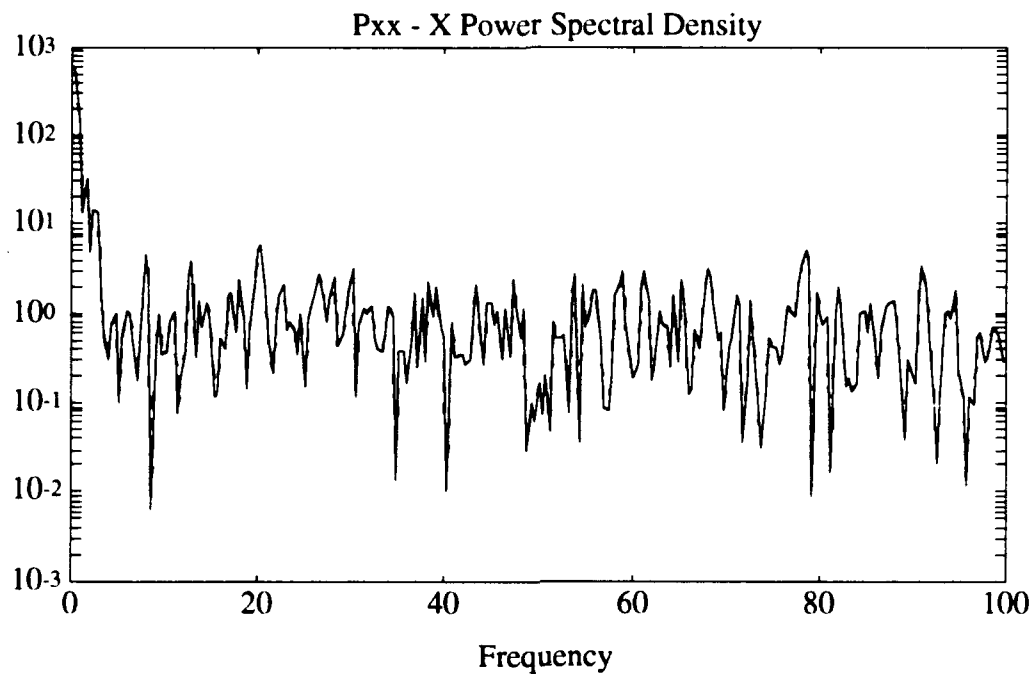


Figure E-1 Current Controller Tracking Error PSD

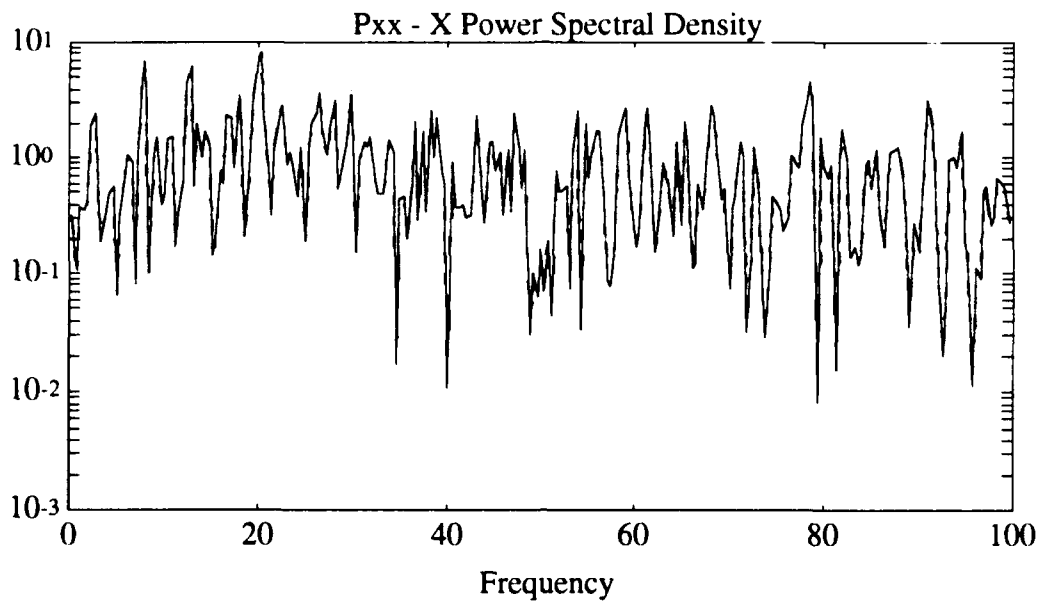


Figure E-2 H₂ Controller Tracking Error PSD

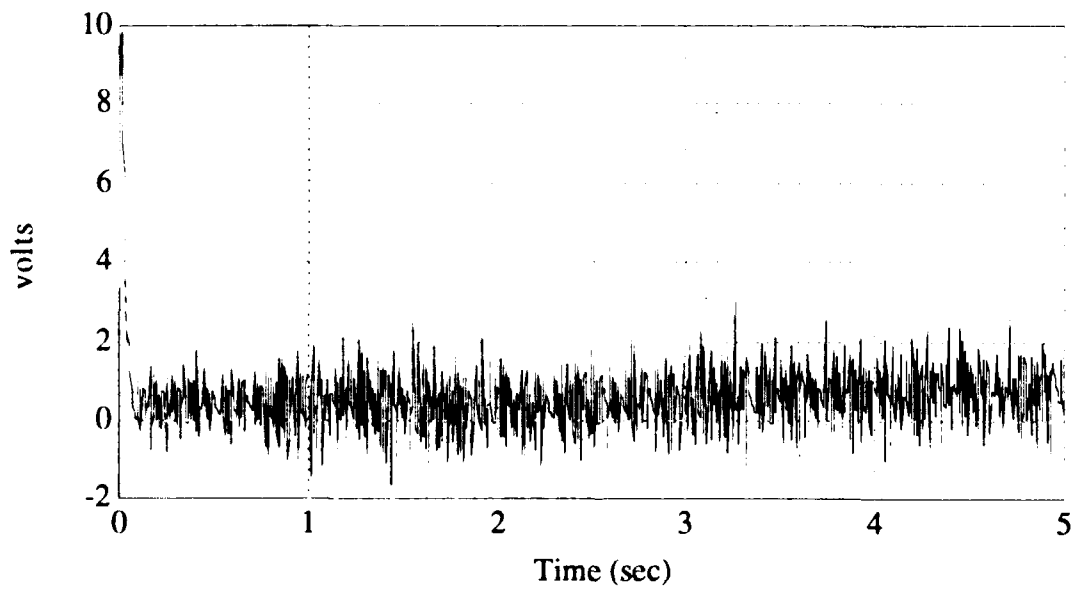


Figure E-3 Current Controller Voltage

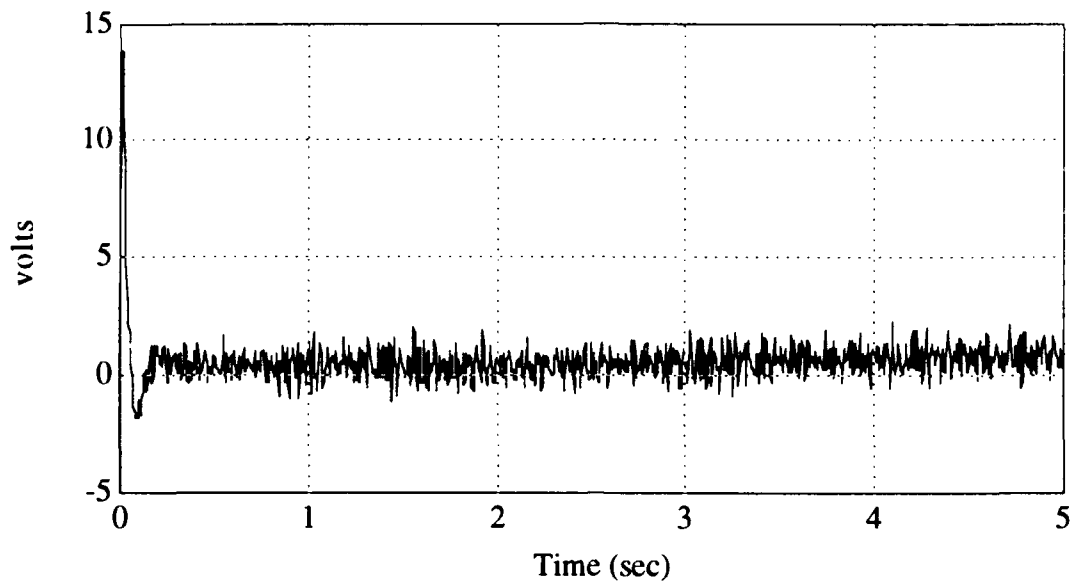


Figure E-4 H₂ Controller Voltage

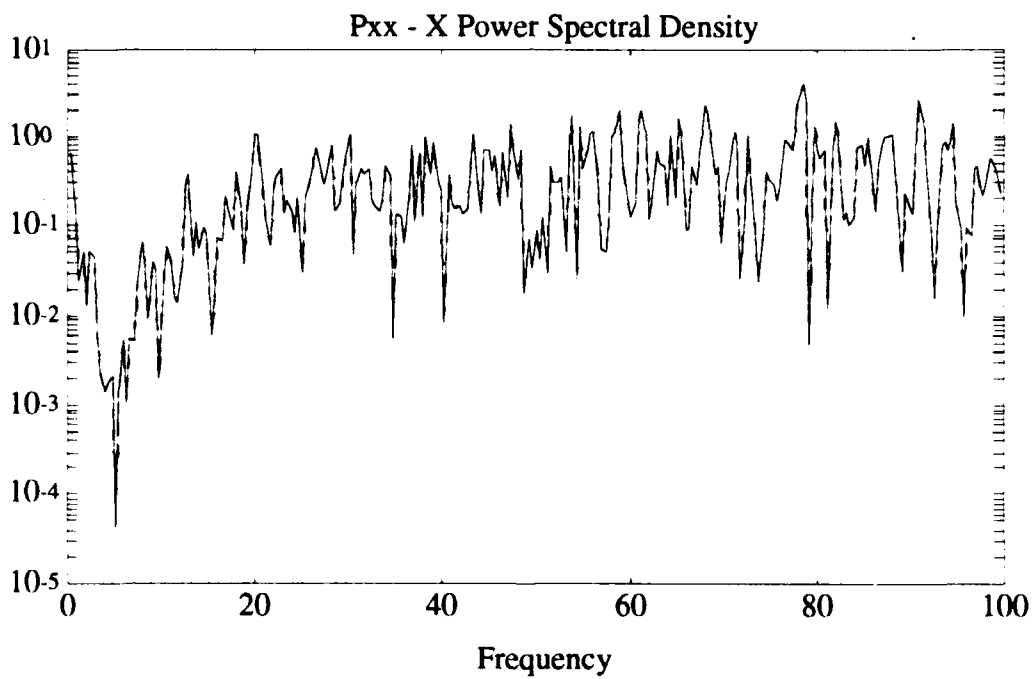


Figure E-5 Current Controller Voltage PSD

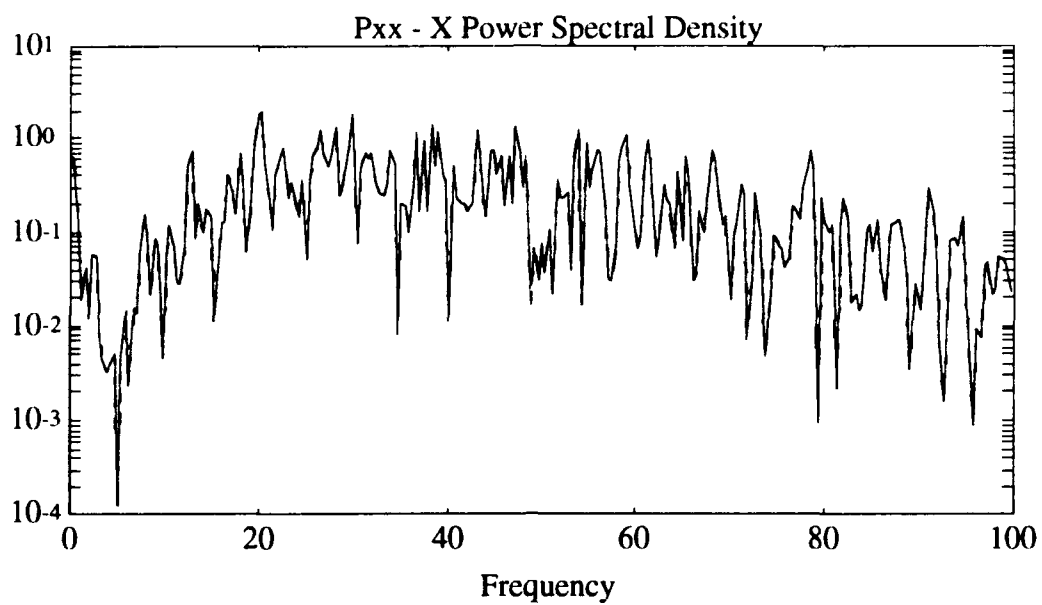


Figure E-6 H₂ Controller Voltage PSD

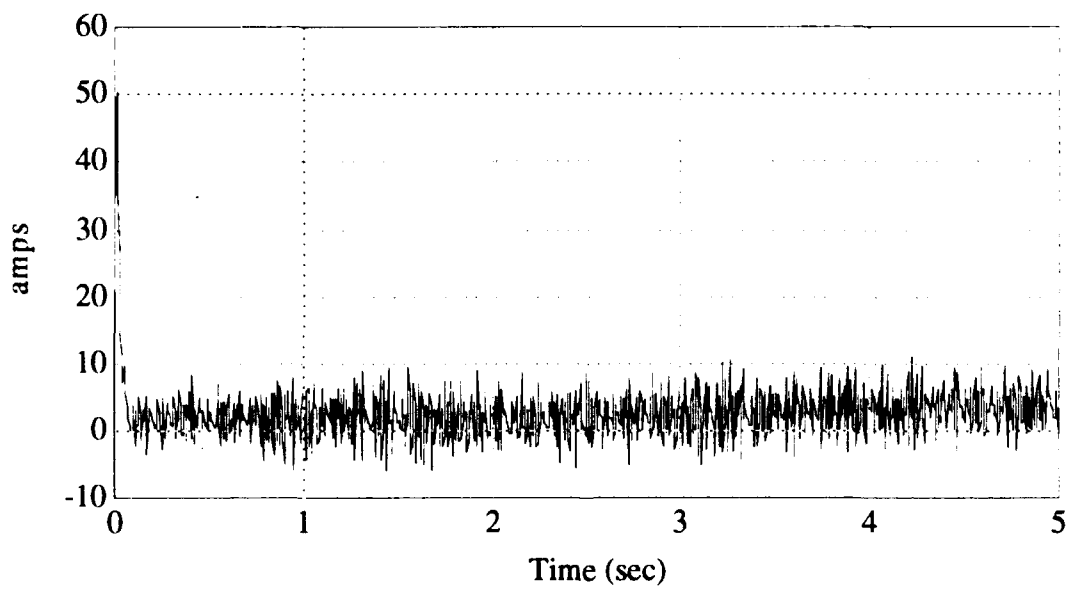


Figure E-7 Current Controller Amps

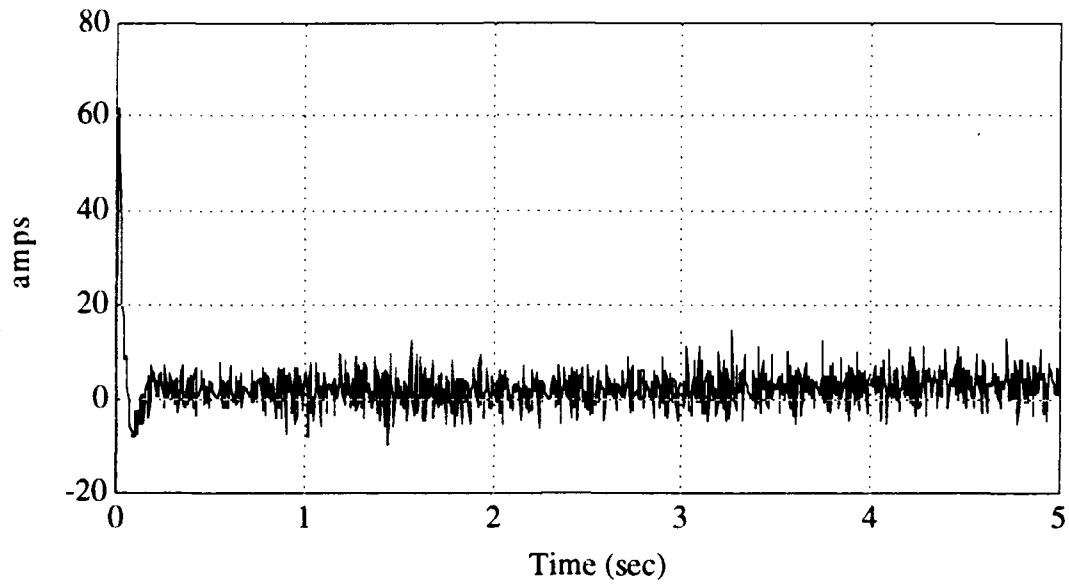


Figure E-8 H₂ Controller Amps

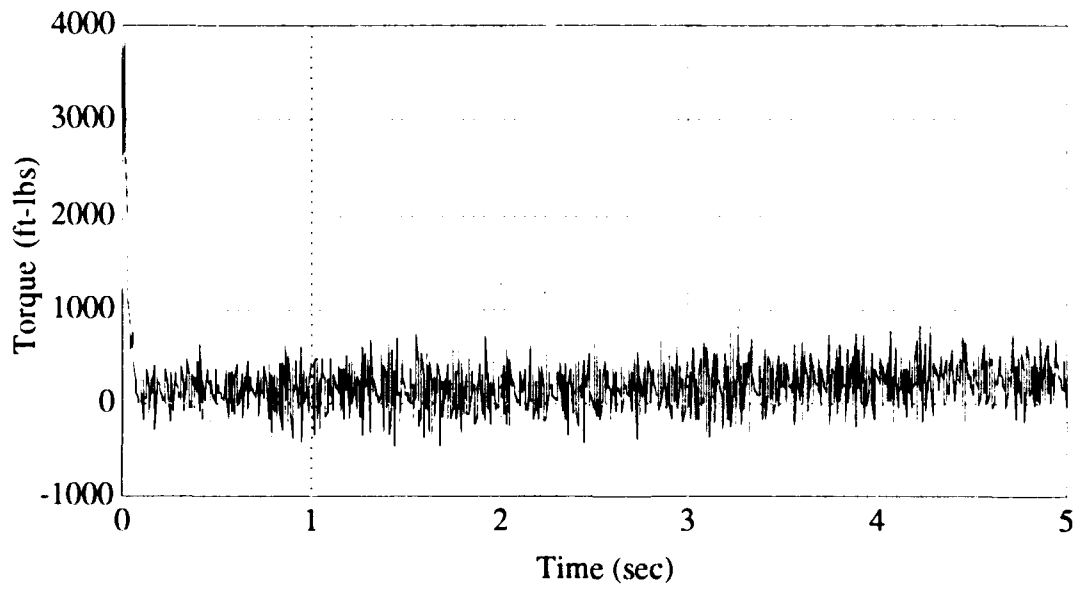


Figure E-9 Current Controller Motor Torque

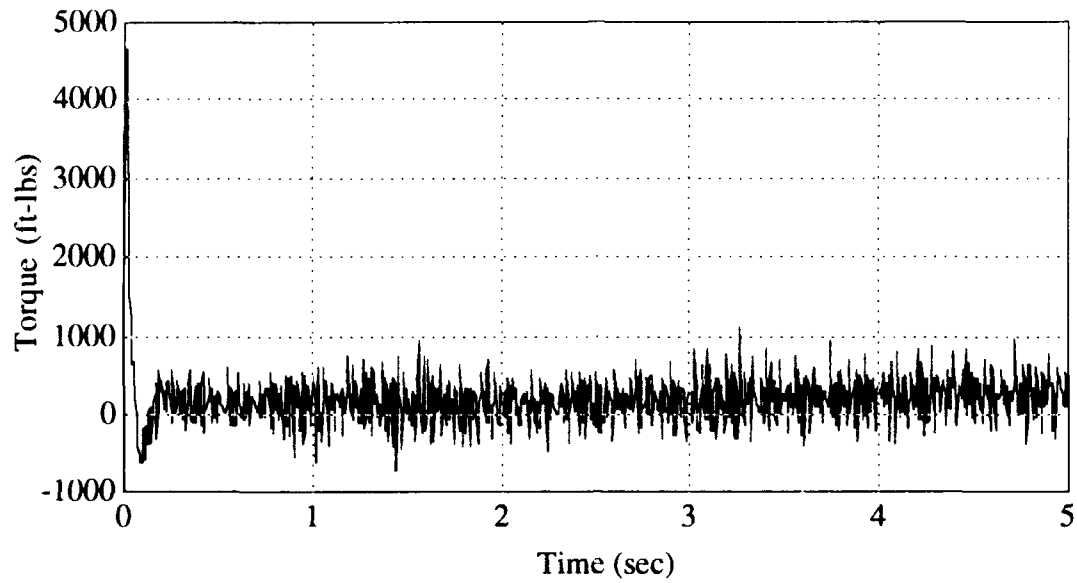


Figure E-10 H₂ Controller Motor Torque

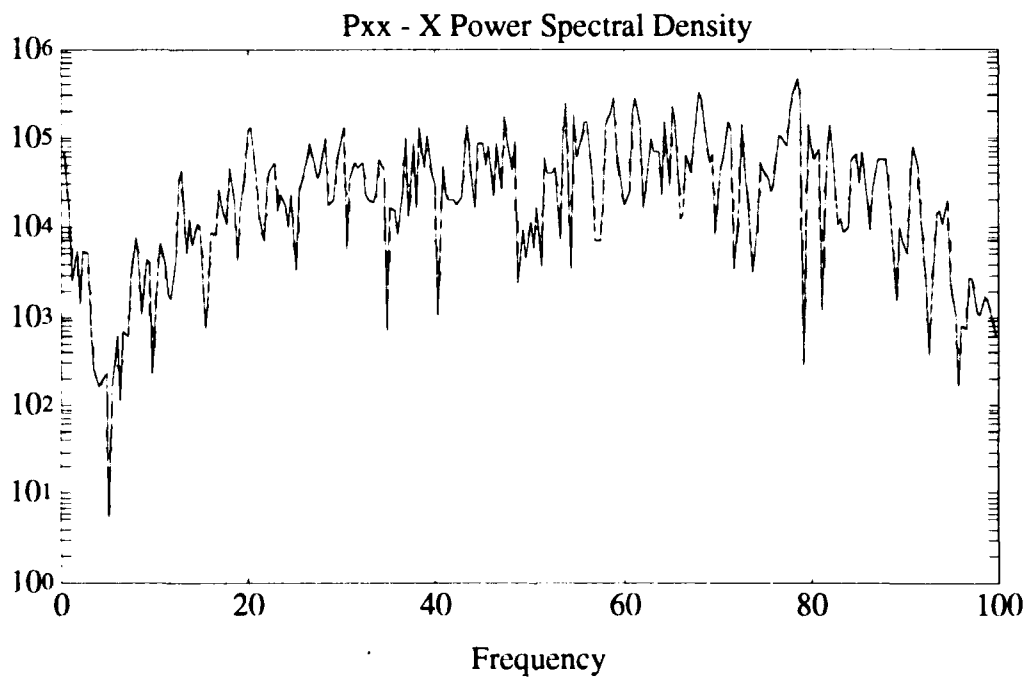


Figure E-11 Current Controller Motor Torque PSD

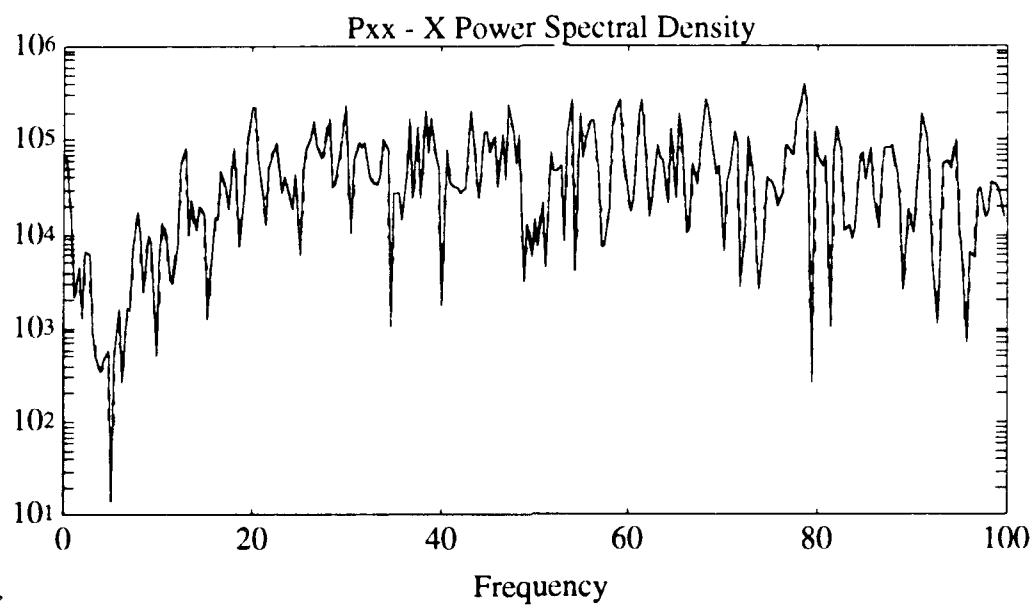


Figure E-12 H₂ Controller Motor Torque PSD

References

1. *Technical Description of a Coelostat System*, August 1979. Technical Report-2965C. Pittsburgh, PA: Contraves Goerz Corporation., August 1979.
2. Franklin, Gene F., J. David Powell, Abbas Emami-Naeini. *Feedback Control of Dynamic Systems*, (Second Edition). Addison-Wesley Publishing Company, Reading, Massachusetts, April 1991.
3. Kwakernaak, Huibert, Raphael Sivan. *Linear Optimal Control Systems*. John Wiley & Sons, Inc., New York, NY, 1972.
4. Houpis, Constantine H., Gary B. Lamont. *Digital Control Systems*. McGraw-Hill, Inc., New York, NY, 1992.
5. Ulich, Bobby L. "Overview of acquisition, tracking, and pointing system technologies," *Proceedings SPIE Acquisition, Tracking, and Pointing II*, 887: 40-63 (January 1988).
6. Hulett, Whitney J. *Comparison of Pointing Control Systems Utilizing Dahl and Coulomb Friction Model Compensation*. MS Thesis GAE/ENY91D-16. School of Engineering, Air Force Institute of Technology (AU), Wright-Patterson AFB OH, December 1991.
7. *3.5-Meter Telescope Control System Document*, December 1990. Technical Report 27902. Pittsburgh, PA: Contraves USA Corporation, December 1990.
8. D.B. Ridgely. *A Non conservative Solution to the General Mixed H_2/H_∞ Optimization Problem*. Ph.D. Dissertation, Massachusetts Institute of Technology, Cambridge, MA, Sept 1991.
9. Doyle, John G., Bruce A. Francis, Allen R. Tannenbaum. *Feedback Control Theory*. Macmillan Publishing Company, New York, NY, 1992.

Vita

Captain Troy V. Lanier was born 25 November 1963 in Germany. He graduated from Iolani School in Honolulu, Hawaii in 1982 and attended the Virginia Military Institute, graduating in 1986 with Distinction with a Bachelor of Science in Mechanical Engineering. Upon graduation he received a regular commission in the USAF and served his first tour of duty at Kirtland AFB, New Mexico. He began as a structural engineer performing modal analysis of a large flexible space structure via computer simulation. He was a qualified project officer, and was program manager for the \$10 million space-based Strategic Defense Initiative's (SDI) Wideband Angular Vibration Experiment that was part of the Relay Mirror Experiment (RME). When the RME was fielded in 1989 he worked as a member of the Science Team analyzing system performance data for the duration of the one year experiment. He was also heavily involved in the very successful RME additional science experiment Adaptive Noise Cancellation for Closed-Loop Systems. He entered the School of Engineering, Air Force Institute of Technology, in May of 1991.

REPORT DOCUMENTATION PAGE

Form Approved
OMB No. 0704-01

1. This report is the property of the Defense Information Systems Agency (DISA) and is loaned to you. It contains information that is exempt from public release under the Freedom of Information Act (5 U.S.C. 552). It is to be controlled, stored, handled, and disposed of in accordance with the instructions in this report. It is to be returned to DISA when it is no longer needed. It is not to be distributed outside the agency to which it is loaned. It is not to be used for official purposes outside the agency to which it is loaned. It is not to be used for official purposes outside the agency to which it is loaned. It is not to be used for official purposes outside the agency to which it is loaned.

1. AGENCY USE ONLY (Leave blank)		2. REPORT DATE December 1992	3. REPORT TYPE AND DATES COVERED Master's Thesis	
4. TITLE AND SUBTITLE Optimal Control of the Starfire Beam Director			5. FUNDING NUMBERS	
6. AUTHOR(S) Troy V. Lanier, Captain, USAF				
7. PERFORMING ORGANIZATION NAME(S) AND ADDRESS(ES) Air Force Institute of Technology, WPAFB OH 45433-6583			8. PERFORMING ORGANIZATION REPORT NUMBER AFIT/GAE/ENY/92D-16	
9. SPONSORING / MONITORING AGENCY NAME(S) AND ADDRESS(ES) Phillips Laboratory Dr. Sal Cusamano PL/LITT Kirtland AFB, New Mexico 87117-6008			10. SPONSORING / MONITORING AGENCY REPORT NUMBER	
11. SUPPLEMENTARY NOTES				
12a. DISTRIBUTION / AVAILABILITY STATEMENT Approved for public release; distribution unlimited			12b. DISTRIBUTION CODE	
13. ABSTRACT (Maximum 200 words) The Starfire Beam Director (SBD) is located at the Starfire Optical Range at Kirtland Air Force Base in Albuquerque, New Mexico. The SBD capabilities include tracking celestial objects and active or passive tracking of artificial satellites to support the Phillips Laboratory Ground Based Laser Acquisition, Tracking, and Pointing (GBL ATP) program. The pointing and tracking accuracy needed to support such experiments is μ rad to sub- μ rad level. To accomplish this goal requires precise pointing of the massive 6 ton 1-meter clear aperture coelostat. The purpose of this thesis is to use optimal control design techniques to develop a controller to meet the stringent pointing requirements. A nominal linear state-space model was built which included gimbal dynamics, plant disturbances, and sensor noise. Then optimal control design techniques were used to develop unity feedback and two degree of freedom controllers. The various controllers were simulated with the coelostat "truth" model, which incorporated the higher frequency control loop and motor dynamics, nonlinearities, plant disturbances, sensor noise, and discrete control effects. The best of the designs, the H_2 unity feedback controller, was compared and contrasted with the performance of the controller currently being used, which was obtained by classical control design. The H_2 controller exceeded tracking requirements and in most areas performed better than the current controller.				
14. SUBJECT TERMS Optimal Control, H_2 Optimization, Gimbal Modeling, Starfire Beam Director Modeling, Acquisition, Tracking, and Pointing (ATP), Unity Feedback and Two Degree of Freedom Control			15. NUMBER OF PAGES 123	
			16. PRICE CODE	
17. SECURITY CLASSIFICATION OF REPORT Unclassified	18. SECURITY CLASSIFICATION OF THIS PAGE Unclassified	19. SECURITY CLASSIFICATION OF ABSTRACT Unclassified	20. LIMITATION OF ABSTRACT UL	